ELECTRICAL, STRUCTURAL AND OPTICAL PROPERTIES OF $AgGaSe_{2-x}S_x$ THIN FILMS GROWN BY SINTERED POWDER

A THESIS SUBMITTED TO
THE GRADUATE SCHOOL OF NATURAL AND APPLIED SCIENCES
OF
MIDDLE EAST TECHNICAL UNIVERSITY

BY

HAKAN KARAAĞAÇ

IN PARTIAL FULFILLMENT OF THE REQUIREMENTS
FOR
THE DEGREE OF DOCTOR OF PHILOSOPHY
IN
PHYSICS

SEPTEMBER 2010

Approval of the thesis:

ELECTRICAL, STRUCTURAL AND OPTICAL PROPERTIES OF $AgGaSe_{2-x}S_x$ THIN FILMS GROWN BY SINTERED POWDER

submitted by **HAKAN KARAAĞAÇ** in partial fulfillment of the requirements for the degree of **Doctor of Philosophy in Physics Department, Middle East Technical University** by,

Prof. Dr. Canan Özgen _____
Dean, Graduate School of **Natural and Applied Sciences**

Prof. Dr. Sinan Bilikmen _____
Head of Department, **Physics**

Prof. Dr. Mehmet Parlak _____
Supervisor, **Physics Dept., METU**

Examining Committee Members:

Prof. Dr. A.Çiğdem Erçelebi _____
Physics Dept., METU

Prof. Dr. Mehmet Parlak _____
Physics Dept., METU

Prof. Dr. Raşit Turan _____
Physics Dept., METU

Prof. Dr. Mehmet Çakmak _____
Physics Dept., Gazi Unv.

Assoc. Prof. Dr. Caner Durucan _____
Metallurgical and Materials Dept., METU

Date: _____

I hereby declare that all information in this document has been obtained and presented in accordance with academic rules and ethical conduct. I also declare that, as required by these rules and conduct, I have fully cited and referenced all material and results that are not original to this work.

Name, Last name : HAKAN KARAAĞAÇ

Signature :

ABSTRACT

ELECTRICAL, STRUCTURAL AND OPTICAL PROPERTIES OF $AgGaSe_{2-x}S_x$ THIN FILMS GROWN BY SINTERED POWDER

Karaağaç, Hakan

Ph.D., Department of Physics

Supervisor : Prof. Dr. Mehmet Parlak

September 2010, 164 pages

In the present study, the effect of S and Se substitution on structural, electrical and optical properties of $AgGa(Se_{2-x}S_x)$ thin films has been investigated.

$AgGa(Se_{0.5}S_{0.5})_2$ thin films were prepared by using the thermal evaporation method. X-ray diffraction (XRD) analysis has revealed that the transformation from amorphous to polycrystalline structure took place at about 450 ^oC. The detailed information about the stoichometry and the segregation mechanisms of the constituent elements in the structure has been obtained by performing both energy dispersive X-ray analysis (EDXA) and X-ray photoelectron spectroscopy (XPS) measurements.

$AgGaSe_2$ thin films were deposited by using both electron-beam (e-beam) and sputtering techniques. In e-beam evaporated thin films, the effect of annealing on the structural and morphological properties of the deposited films has been studied by means of XRD, XPS, scanning electron microscopy (SEM) and EDXA measurements. Structural analysis has shown that samples annealed between 300 and 600 ^oC were in polycrystalline structure with co-existance of Ag, Ga_2Se_3, GaSe, and $AgGaSe_2$. The variation of surface morphology, chemical composition and bonding nature of constituent elements on post-annealing has been determined by EDXA and XPS analyses.

$AgGaSe_2$ thin films were also prepared by using sputtering technique. XRD measurements have shown that the mono-phase $AgGaSe_2$ structure is formed at annealing temperature of 600 ^oC. The crystal-field and spin-orbit splitting levels were resolved. These levels around 2.03 and 2.30 eV were also detected from the photospectral response measurements.

Thin films of Ag-Ga-S (AGS) compound were prepared by using $AgGaS_2$ single crystalline powder and deposition of the excess silver (Ag) intralayer with double source thermal evaporation method. As a consequence of systematic optimization of thickness of Ag layer, Ag(Ga,S) with the stoichiometry of $AgGa_5S_8$ and $AgGaS_2$ were obtained and systematic study to obtain structural, electrical and optical properties was carried out.

Keywords: Chalcopyrites, Thermal evaporation, Electron-beam evaporation, Sputtering technique, Structural characterization, Optical characterization, Electrical characterization

ÖZ

SİNTERLENMIŞ TOZDAN BÜYÜTÜLEN $AgGaSe_{2-x}S_x$ İNCE FİLMLERİN ELEKTRİKSEL, YAPISAL VE OPTİK ÖZELLİKLERİ

Karaağaç, Hakan

Doktora, Fizik Bölümü

Tez Yöneticisi : Prof. Dr. Mehmet Parlak

Eylül 2010, 164 sayfa

Bu çalışmada S ve Se yerdeğiştirme konsantrasyonun $AgGa(Se_{2-x}S_x)$ ince filmlerin yapısal, elektriksel ve optiksel özellikleri üzerine etkisi incelenmiştir.

$AgGa(Se_{0.5}S_{0.5})_2$ ince filmler ısısal buharlaştırma yöntemi kullanılarak hazırlandı. X-ışın kırınımı (XRD) analizi amorf yapının çoklu-kristal yapısına geçişinin 450 ^oC'deki tavlama sıcaklığında gerçekleştiğini ortaya koydu. İçerik elementlerin stokometrisi ve segregasyon mekanizmaları hakkındaki detaylı bilgi enerji dağılımlı X-ışını analizi (EDXA) ve X-ışını fotoelektron spektroskopisi (XPS) ölçümleri gerçekleştirilerek elde edildi.

$AgGaSe_2$ ince filmleri hem elektron-demeti (e-demeti) hem de saçtırmalı kaplama yöntemleri kullanılarak üretildi. E-demeti yöntemiyle kaplanan filmlerde tavlanmanın kaplanan filmlerin yapısal ve morfolojik özellikleri üzerine etkisi XRD, XPS, taramalı elektron mikroskobu (SEM) ve EDXA ölçümleri sayesinde çalışıldı. Yapısal analiz 300 ve 600 ^oC arasında tavlanan numunelerin Ag, Ga_2Se_3, GaSe ve $AgGaSe_2$ fazlarıyla birlikte çoklu-kristal yapıda olduğunu gösterdi. Tavlamayla beraber yüzey morfolojisi, kimyasal içeriği ve içerik elementlerinin bağ değişimi EDXA ve XPS analizleriyle incelenmiştir.

$AgGaSe_2$ ince filmler ayrıca saçtırma tekniği kullanılarak da hazırlandı. XRD ölçümleri 600 ^oC tavlama sıcaklığında tek-fazlı $AgGaSe_2$ yapısının oluştuğunu

gösterdi. Kristal-alan ve spin-yörünge bölünme seviyeleri 2.03 ve 2.30 eV'de spektral fototepki ölçümleriyle de saptandı.

Ag-Ga-S (AGS) ince film bileşiği $AgGaS_2$ tek kristal toz ve ekstra ara gümüş (Ag) katmanların iki kaynaklı ısısal buharlaştırma yöntemi ile kaplanmasıyla hazırlandı. Ag katmanının kalınlığını sistematik optimizasyonu sonucu $AgGa_5S_8$ ve $AgGaS_2$ stokoyimetrilerine sahip Ag(Ga,S) elde edildi, ve yapısal, elektriksel ve optik özelliklerin ortaya çıkartılması için sistematik bir çalışma gerçekleştirildi.

Anahtar Kelimeler: Kalkopritler, Isısal buharlaştırma, Elektron-demeti buharlaştırma, Saçtırma tekniği, Yapısal karekterizasyon, Optik karekterizasyon, Elektriksel karekterizasyon

To My Family

ACKNOWLEDGEMENTS

Firstly, I would like to offer my deepest appreciation and sincere gratitude to my supervisor Prof. Dr. Mehmet Parlak for his endless support, guidance and great effort that enabled me to develop my skills as an experimentalist and understand the subject we have studied. I would also like to present my sincere thanks to thesis committee members, Prof. Dr. Çiğdem Erçelebi, Assoc. Prof. Dr. Caner Durucan, Prof. Dr. Raşit Turan, and Prof. Dr. Mehmet Çakmak, who made this thesis more plausible.

My special thanks to Yücel Eke for his assistance with all types of technical problems at the every stage of this study.

I also want to thank my dear friends in basement floor, who have made this work quite enjoyable, Dr. Murat Kaleli, Mustafa Kulakçı, Dr. Tahir Çolakoğlu, İdris Candan, Dr. Arife Gencer, and Hasan Hüseyin Güllü.

Many thanks to all academic and administrative staff of Department of Physics; in particular I would like to acknowledge the helps of Gülşen Özdemir Parlak and Zeynep Eke.

Many thanks also to my home mate Hacı Mehmet Duranoğlu for sharing life during seven years. I am also grateful to Meliz for her unlimited understanding and endless patience.

Lastly, I offer my special thanks to each member of my family, without their encourange and support this thesis would not have been possible.

TABLE OF CONTENTS

LIST OF TABLES

TABLES

LIST OF FIGURES

FIGURES

CHAPTER 1

INTRODUCTION

In recent years, I-III-VI_2 ternary compounds have been studied extensively due to their interesting optical and electrical properties. These types of compounds are regarded as to be the ternary analogues of the II-VI binary semiconductors. I-III-VI_2 materials crystallize with the structure called chalcopyrite, which is a supper lattice of structure of II-VI compounds (Zinc-blende). Chalcopyrites are potential candidates for a number of applications such as photovoltaics [1], non-linear optics [2], and harmonic generations of frequencies [3]. Tuning the band gap energies (ranging from 3.5 eV ($CuAlS_2$) to 1.04 eV ($CuInSe_2$)) make these compounds as promising candidates for the light-emitting devices (LEDs) and detectors in wide wavelength range varying from ultraviolet to infrared [4]. Their properties can be modified in large extend due to the possibility of accommodation with different dopants, which results in formation of various solid solutions to be used in specific applications [5]. I-III-VI_2 compounds are particularly good candidates for the formation of the p-n heterojunction with II-VI group semiconductors because of the similarity between the structures of two compounds. It is also one of the reasons for them to be seen as convenient material for the fabrication of high-efficient solar cells. In general, chalcopyrite ternary compounds are divided into two different groups, namely, copper (Cu-III-VI_2) and silver (Ag-III-VI_2) based compounds. Among the Cu-based materials the most extensively studied one is the Cu (In, Ga) Se_2 (CIGS), particularly convenient for the construction of high-efficient thin film solar cells due to having a high absorption coefficient (10^5 cm^{-1}), the convenient optic band gap for solar cell spectrum (1.04 eV) and easily producible by a number of deposition techniques. Solar cells using CIGS as an absorber block have already reached a19.5% efficiency [4]. On the other hand, the Ag-based chalcopyrites attract much attention because of their potential applications in non-linear optical and

photonic applications [6]. Among the Ag-based chalcopyrites, the $AgGaS_2$ is one of the most known compounds having a direct band gap of about 2.7 eV and good transparency in the wavelength range of 500-1200 nm [7]. Providing high transparency in this region makes this compound as a potential candidate for the frequency doubler and tripler of CO_2 laser output [8]. It is also known that the high transparency in 550 nm is used in the fabrication of optic parametric oscillator (OPO) pumped by Nd:YAG laser [9]. Moreover, due to having a uniaxial structure the birefringence characteristic is achieved in this material. The degree of birefringence is so high that it permits phase matching over a wide wavelength range in linear and non-linear optical interactions [10]. The $AgGaS_2$ could be phase matched for the generation of second and third harmonics for the fundamental wavelength ranging between 1.8 and 11 μm. In addition, it is possible to extend the three wave mixing process to this range [11]. It is known that $AgGaS_2$ behaves as a semi-insulating ($>10^8$ Ω-cm) material. And, for all efforts to decrease resistivity of either n-or p-type, it seems very difficult to achieve because of existing of shallow states in band gap region resulting in formation of both acceptors and donors leading to self-compensation [12]. Attempts to improve the conductivity of $AgGaS_2$ by several efforts such as annealing and impurity doping have failed. That's also the reason of limited usage of this material in large extend in optoelectronics applications [13].

$AgGaSe_2$ is another well-known ternary semiconductor that have been studied extensively. It is of particular interest due to having optical non-linear properties, like $AgGaS_2$, used in many applications such as the generation of second and third harmonic frequencies [14-16]. It is also known that $AgGaSe_2$ is a promising material for the preparation of Schottky diodes [17], X- and gamma-ray detector [18], and solar cells [19]. Especially, p-type $AgGaSe_2$ thin films have shown that they exhibit favorable optical and electronic properties similar to $CuInSe_2$ and $CuGaSe_2$ and are suitable for fabricating heterojunction solar cells. $AgGaSe_2$ has a direct band gap nature with energy value around 1.80 eV [20] and shows the characteristic optical band gap structure of I-III-VI_2 ternary compounds. $AgGaSe_2$, like $AgGaS_2$, is a semi-insulating material having resistivity values varying from $1x10^8$ to $3x10^{10}$ Ω-cm [21-23]. $AgGaSe_2$ can be obtained as n-type or p-type depending on formation of anion (V_{Se}) and cation (V_{Ga}, V_{Ag}) vacancies in the

structure during the deposition cycle or post-depositional heat treatments [24].

In summary, both $AgGaS_2$ and $AgGaSe_2$ compounds are known for their good transparency in infrared region (from 0.71 to 18 μm), large birefringence and non-linear optical (NLO) properties. To obtain the desired linear and non-linear optical features for specific applications the solid solution of $AgGaS_2$ and $AgGaSe_2$ ($AgGaSe_{2-x}S_x$) can be formed by tuning alloy composition for different x values. Since the properties of materials are closely related to the constituent atoms $AgGaSe_{2-x}S_x$ alloy may exhibit quite interesting electrical and optical properties.

1.1 Structure of I-III-VI_2 materials

I-III-VI_2 (I=Cu, Ag, III=In, Ga, VI=S, Se, Te) materials are regarded as to be the ternary analogue of the II-VI binary compounds having a structure called zinc-blende as shown in Fig.1.1

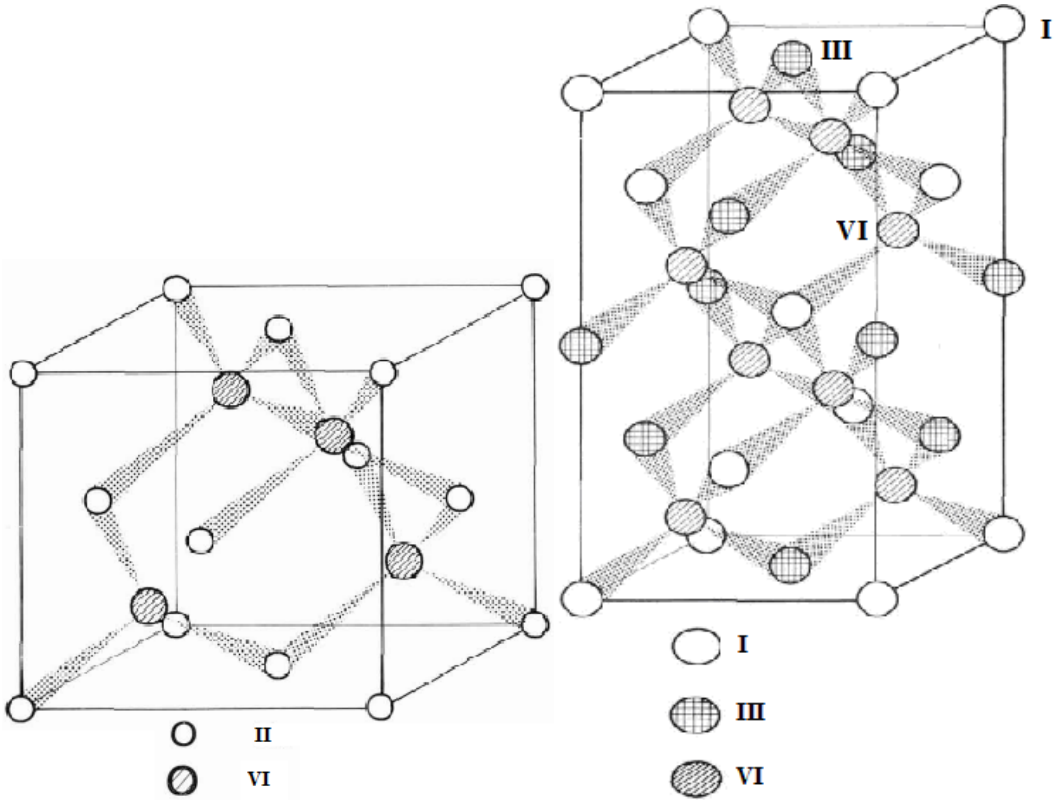

(a) (b)

Figure 1.1: Unit cell structure of (a) Zinc-blende and (b) Chalcopyrite.

As can be seen from figure, I-III-VI_2 semiconductors crystallizing in the chalcopyrite structure with tetragonal ($a=b\neq c$, $\alpha=\beta=\gamma=90^o$) and space group symmetry I(-4)2d with four formula units in each unit cell, which is constructed by doubling the unit cell of the zinc-blende in vertical direction [5]. The vertical direction in zinc-blende is z-axis and becoming the c-axis in the chalcopyrite unit cell. There may be a difference in terms of c/a ratio for the most of real chalcopyrite compounds and that have ideal chalcopyrite structure, which is equal to two for ideal chalcopyrite structure. In spite of a supperlattice of zinc-blende structure, there are some deviations relative to binary analogues called anomalies. The anion displacement (μ) is one of these anomalies stemming from the existing of two different cations (I and III) in the chalcopyrite structure with respect to zinc-blende structure. The ordered distribution of these cations in place of group-II atoms in the zinc-blende unit cell in sequence of I-III-I-III with c/2 interval steps results in construction of chalcopyrite unit cell. As can be seen from the Fig. 1.1, each cation coordinates with four anions in zinc-blende structure, while in chalcopyrite structure each anion coordinates with two different cations and each cation with four anions [5, 25-26]. It is the existing of these two different cations that result in formation of two bonds with different length (I-VI and III-VI), which give rise to displacement of anions from their ideal position in the structure. One another anomaly is the deviation of c/a from two in chalcopyrite structure called tetragonal distortion (η). For the determination of the anion displacement parameter, firstly the position parameter (σ) (defining the position of VI atoms with respect to I and III atoms in the structure of I-III-VI_2) is calculated by using the lattice parameters (a and c for tetragonal system) as follow [27]

$$\sigma = 0.5 - 0.25\left[\frac{c^2}{2a^2} - 1\right]^{\frac{1}{2}} \tag{1.1a}$$

$$R_{I-VI} = 0.125a\left[64\sigma^2 + 4 + \left(\frac{c}{a}\right)^2\right]^{\frac{1}{2}} \tag{1.1b}$$

$$R_{III-VI} = 0.125a\left[64(0.5-\sigma)^2 + 4 + \left(\frac{c}{a}\right)^2\right]^{\frac{1}{2}}$$

(1.1c)

where $R_{I\text{-}III}$ and $R_{III\text{-}VI}$ are bond lengths of I-VI and III-VI pairs, respectively. Having calculated bond lengths, the anion displacement parameter is calculated through the following relation

$$\mu = \frac{1}{4} + \left[\frac{R^2{}_{I-VI} - R^2{}_{III-VI}}{a^2}\right] \tag{1.2}$$

In addition, the second anomaly parameter (tetragonal distortion (η)) is represented by η=2-c/a [28]. These anomalous parameters play an important role on determining structural and optical properties of chalcopyrite materials. The deviation of anion, for instance, from its ideal position has a considerable effect on designating the band gap of such types of compounds as a consequence of alternation in degree of hybridization between anion and cation orbitals.

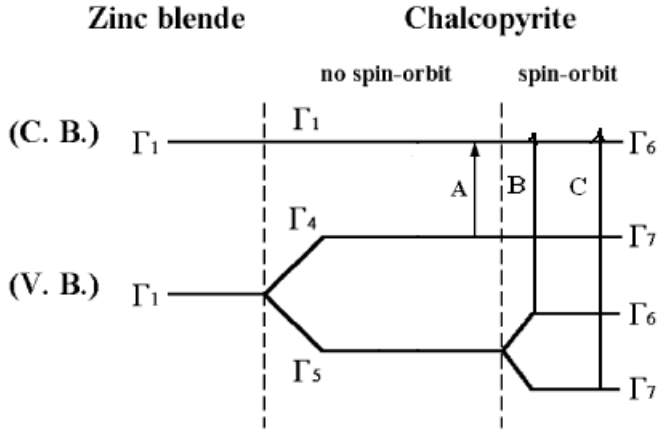

Figure 1.2: Crystal-field and spin-orbit splittings.

Unlike II-VI compounds, in chalcopyrite structure the triple degeneracy in p-like character Γ_{15} level consisting top of the valance band in Zinc-blende structure is lifted and split into three resolved levels as a result of tetragonal symmetry of the tetragonal crystal field and spin orbit interaction in chalcopyrite structure [5, 29-30]. That is, as a consequence of crystal-field the degeneracy of Γ_{15} is lifted and subsequently a non-degenerate level Γ_4 is resolved and stand above a doubly degenerated level Γ_5 as shown in Fig. 2.2 [7]. Furthermore, when the spin-orbit interaction is taken into account, the Γ_5 separated into Γ_6 and Γ_7, whereas Γ_4 and Γ_1 convert into Γ_7 and Γ_6, respectively [30]. Here, A, B and C transitions correspond to band to band transition, the crystal field, and the spin-orbit splitting levels to conduction band minimum, respectively. Thus, the characteristic band gap structure of I-III-VI_2 chalcopyrite compounds is consisted of triple transitions.

The structural, electrical, and optical properties of $AgGa(Se_{2-x}S_x)$ crystals have been studied both experimentally and theoretically by Tang et al. [31]. The structure of $AgGaS_2$ and $AgGaSe_2$ is shown in Fig. 1.3. As a common characteristic of all other chalcopyrites, $AgGaSe_2$ and $AgGaS_2$ unit cell is a supperlattice of two zinc blende unit cell with I(-4)2d space group symmetry. A typical unit cell of $AgGaSe_2$ and $AgGaS_2$ is consisted of four cation (Ag and Ga) and eight anion (Se or S) atoms. The symmetrical position of these atoms are represented by (x, y, z), (-x, -y, -z), (y, -x, -z), (-y, x, -z), (-x+1/2, y, -z+3/4), (x+1/2, -y, -z+3/4), and (-y+1/2, -x, z+3/4), respectively.

The substitution of Se and S in $AgGa(Se_{2-x}S_x)$ for different x values results in either compressing or expanding in the volume of unit cell which have a significant effect on determining structural parameters and optical properties. The calculated and measured some structural parameters (tetragonal distortion (η) and anion displacement (μ)) and bond lengths between the constituent atoms of $AgGa(Se_{2-x}S_x)$ for x values ranging from 0.00 to 1.00 are given in Table 1.1. The presence of two types of cation-S and/or cation-Se bonds results in distortion of tetrahedral coordination of S and/or Se atoms. The calculated average bond lengths for Ga-S, Ga-Se, Ag-S, and Ag-Se are given in Table 1.1. The bond lengths of Ga-S and Ag-S in $AgGaS_2$ were calculated to be 2.24 and 2.60 Å, and Ga-Se and Ag-Se bonds in $AgGaSe_2$ were found to be 2.42 and 2.60 Å, respectively [32]. The bonding between

(Ag, Ga) and (Se, S) results in a shorter bond lengths in $AgGa(Se_{2-x}S_x)$ with increasing x value. That is also the reason of increase in band gap of this compound with increasing S concentration due to the unit cell's volume compression.

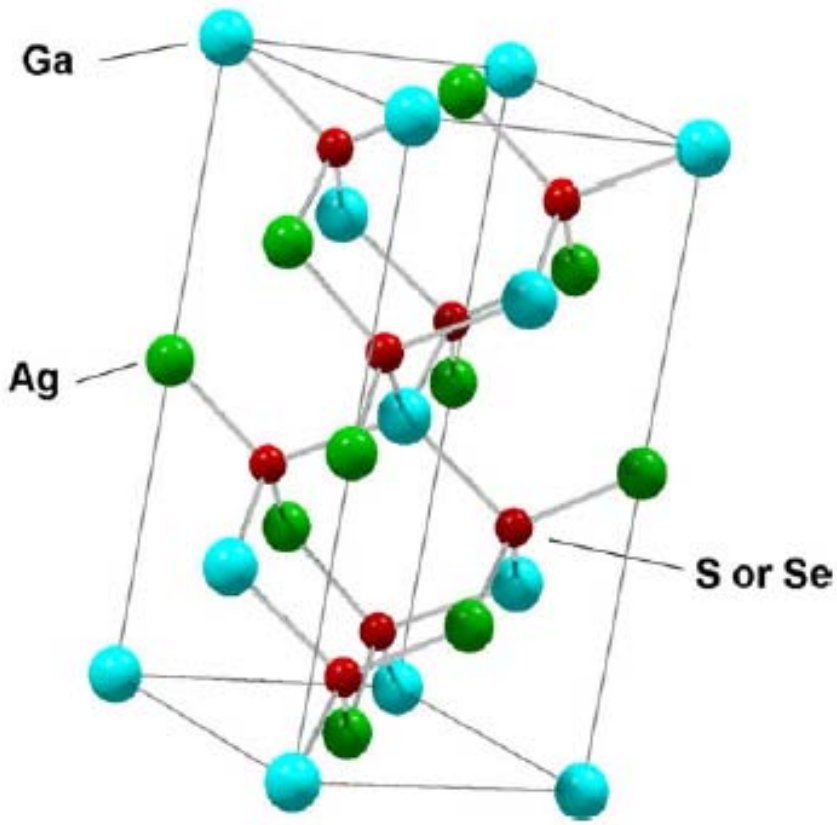

Figure 1.3 [31]: Crystal structure of $AgGaSe_2$ and $AgGaS_2$.

XRD studies on $AgGa(Se_{2-x}S_x)$ crystals have revealed that the preferred orientation (112) peak position (2θ) is shifting gradually with substituting composition. That is, 2θ values of XRD peaks are decreasing with increasing x value. It is also reported that the lattice parameters of $AgGa(Se_{2-x}S_x)$ varies linearly with x as $a = b \approx (5.99\text{-}0.55x)$ Å, $c \approx (10.87\text{-}0.57x)$ Å, and results in a change in linear variation of unit cell volume with x as $V \approx (387.88\text{-}54.50x)$ $Å^3$.

Table 1.1: Structural parameters and bond lengths of $AgGa(Se_{2-x}S_x)$ for different x values [31].

	x				
parameters	0.00	0.25	0.50	0.75	1.00
a (Å) (exp.)	5.97	5.92	5.86	5.80	5.74
a (Å) (calc.)	5.87	5.89	5.77	5.66	5.63
c (Å) (exp.)	10.88	10.73	10.57	10.42	10.26
c (Å) (calc.)	10.64	10.60	10.24	10.09	10.02
Ga-S (Å) (calc.)	-	2.17	2.14	2.14	2.15
Ga-Se (Å) (calc.)	2.30	2.29	2.27	2.26	-
Ag-S (Å) (calc.)	-	2.64	2.60	2.59	2.59
Ag-Se (Å) (calc.)	2.70	2.68	2.67	2.65	-
η (exp.)	1.79	1.80	1.80	1.81	1.82
η (calc.)	1.81	1.87	1.84	1.85	1.84
μ [S] (calc.)	-	0.32	0.32	0.32	0.32
μ [Se] (calc.)	0.31	0.31	0.31	0.31	-

1.2 Previous studies

To investigate the structural, electrical and optical properties of $AgGa(Se_{2-x}S_x)$ single crystal or thin films for different x values many studies have been carried out so far.

H. V. Campe [13] has studied the growth and electrical properties of $AgGaS_2$ thin films in detail. In that study, the polycrystalline and amorphous $AgGaS_2$ thin films were grown by flash evaporation method. As a result of measurements, it was concluded that this material was not sufficient in terms of photosensitivity to be used for device applications, and the low photosensitivity was attributed to the existing of high trap concentration. In addition, the photosensitivity was observed only for the $AgGaS_2$ thin films deposited at substrate temperature of 600 ^{o}C.

The effect of annealing on structural and optical properties of $AgGaS_2$ thin films was studied by H.-C. Hsu et al. [7]. Films in that study were deposited by pulsed laser deposition. From the XRD studies, it was found that below the annealing

temperature of 550 ^{o}C the co-existence of Ag and $AgGaS_2$ was appeared, but after annealing at 550 ^{o}C for 30 minute, the single phase of $AgGaS_2$ with (112) preferred orientation was developed. In addition, from the photoluminescence (PL) measurements, the shallow donors and exciton binding energies were determined and analyzed in detail.

Growth of $AgGaS_2$ single crystals was studied by E. Niwa et al. [33]. $AgGaS_2$ single crystals in that study were grown by self-seeding vertical gradient freezing method, and the effect of growth conditions on crystal quality was investigated in detail. As a result of this study, the basic reason behind difficulty in growing $AgGaS_2$ single crystal was found to be a large supercooling of 51 ^{o}C. To cope with this problem a capillary larger than the length of the supercooling region was used. After this modification, it was possible to grow $AgGaS_2$ single crystals with dimension of around 12 mm x 20 mm.

B. Chen et al. [34] modified a crystal growth furnace to grow high quality $AgGaS_2$ single crystals. By using this furnace with a growth rate of 5-8 mm/day and temperature gradient of 30^{o}C/cm, they were able to grow crack free high quality $AgGaS_2$ single crystals. This study was also revealed that to grow high quality $AgGaS_2$ single crystals the modified furnace is the promising way.

PL of Er-doped $AgGaS_2$ single crystal has been studied by S. Shirakata et al. [35]. From the PL study two PL series were observed, which were 1.83-1.88 eV and 2.22-2.26 eV regions. The band observed at 2.28 eV was attributed to the $4f^6sd$-$4f^7$ transition of Eu^{2+} ion in $AgGaS_2$.

M. Marceddu et al. [36] performed PL measurements for $AgGaS_2$ samples in the form of needles grown by chemical vapour transport method to investigate the donor-acceptor pairs and exciton recombinations. Following to systematic study of temperature and excitation density power dependence of PL, two emission peaks at 461.6 nm and 502.4 nm were observed at 10 K. From the temperature dependent PL, it was found that the observed peaks at 461 nm and 502 nm were belonging to bound excitons with estimated 34 meV binding energy and donor-acceptor recombination, respectively.

The effect of post-annealing on physical properties of $AgGaSe_2$ thin films grown onto quartz glass substrates by using an evaporation method has been studied

by H. Matsumo et al. [20]. From the XRD study, it was found that the single phase of $AgGaSe_2$ could be developed at an annealing temperature of 600 ^oC. By means of wavelength dependence of transmittance and reflectance spectra, the absorption coefficient and band gap energy values were evaluated and found to be around 10^5 cm^{-1} and 1.79 eV, respectively.

H. Matsuo et al. [37] have studied the effect of Ag/Ga composition ratio on optical properties of $AgGaSe_2$ thin films. $AgGaSe_2$ thin films with Ag/Ga ratio ranging from 0.4 to 1.5 were deposited on glass substrates by using vacuum evaporation technique. From the optical transmittance at room temperature, the band gap energies were evaluated except for the Ag/Ga ratios of 0.4 and 1.5. It was observed that the band gap energy was increasing with increasing Ag/Ga ratio, which was attributed to the Bernstein-Moss shifts. PL study was carried out for all samples, but the strong PL spectrum was obtained for only stoichiometric samples. That was explained by existing less defects resulting in non-radiative recombination in stoichiometric sample with respect to Ag-and Ga-rich samples. Two PL bands at 1.77 and 1.70 eV were observed in stoichiometric samples and ascribed to bound exciton emission and donor-acceptor pair (DAP) emission, respectively. The observed DAP emission was attributed to recombination between V_{Se} and V_{Ga} defects.

Photo-electrical properties of $AgGaSe_2$ single crystal has been studied by U. N. Roy et al. [23]. Bridgman technique was used for the growth of high resistive $AgGaSe_2$ single crystals. The photoconductivity measurements revealed that the room temperature photoconductivity at near band edge was $2x10^4$ times higher than the dark conductivity. The optical structure characteristic of I-III-VI_2 materials was revealed by observing the transitions from Γ_7 (A), Γ_6 (B), and Γ_7 (C) to conduction band Γ_6. By taking account the observed peak energy values, the crystal field and spin-orbit splittings were evaluated and found to be around -0.24 and 0.35 eV, respectively.

S. –F. Zhue et al. [38] has studied the effect of heat treatment on optical properties of $AgGaSe_2$ single crystals. It was found that the optical quality of crystal can be improved by both quenching and annealing process. But, the annealing of $AgGaSe_2$ crystals in presence of Ag_2Se at 800 ^oC was found to be more effective in

terms of enhancing the optical quality. Heat treatment resulted in pronounceable improvement in both the IR absorption and the efficiency of frequency doubling process. After the heat treatment on $AgGaSe_2$ crystal, 8.2% energy conversion efficiency in frequency of CO_2 laser output was achieved.

A study on identification of near-infrared absorption bands of $AgGaSe_2$ single crystals grown by a modified Bridgman method was reported by W. Z. Shen [39]. To identify these absorption bands a comparative investigation of transmittance and photoluminescence measurements were carried out. Two absorption bands at 1.3 and 2.2 μm were observed and attributed to the donor-acceptor (D^oA^o) pair recombination related to selenium and silver vacancies and precipitates in $AgGaSe_2$ resulting in non-radiative recombination, respectively.

The change in absorption edge with temperature has been studied by E. Calderon et al. [40]. Absorption measurements were carried out in the temperature range of 9-300 K for $AgGaSe_2$ single crystal grown by standard vertical Bridgman method. The energy band gap values were obtained by using the Elliot-Toyozawa model. The thermal expansion and electron-phonon interaction were taken into account to determine the band gap energy-temperature variation. Based on these analyses, it was found that $AgGaSe_2$ shows a positive energy gap coefficient $dE_g/dT=0.9x10^{-4}$ eV/K for the temperature region of 9-100 K and a negative energy gap coefficient $dE_g/dT=-1.3x10^{-4}$ eV/K for temperatures above 100 K.

M. R. A. Bhuiyan et al. [41] have reported the optical absorption characteristic of $AgGaSe_2$ thin films deposited by sequentially evaporated individual elemental layers onto glass substrates. XRD measurements indicated a polycrystalline structure with a (112) preferred orientation belonging to tetragonal chalcopyrite system. The optical absorption coefficient was found to be varying from 10^5 to 10^3 cm^{-1} depending on composition of deposited films. Optical analyses have revealed that there was more than one type of electronic transitions. These were direct allowed and direct forbidden transitions varying from 1.62 to 1.75 eV and 2.08 to 2.20 eV, respectively, as a function of composition. Results also indicated that the spin-orbit splitting becomes minimum for the $AgGaSe_2$ samples with perfect stoichiometry.

The structural, electronic, and optical properties of $AgGa(Se_{2-x}S_x)$ crystals

have been investigated theoretically and experimentally by Tang et al. [31]. The measurements have shown that the electronic band gap and optical properties were linearly dependent on the substitution concentration of cations. It is also found that the electronic states near the band edge of this compound were consisted of the mixture of the atomic orbitals of Se and S. Linear dependence of material properties of $AgGa(Se_{2-x}S_x)$ was attributed to cell-volume effect. The unit cell volume was found to be compressing by linearly increasing x and resulted in a linear increase in band gap values and second order non-linear optical (NLO) susceptibility. In addition, results have revealed that the unit cell structure and the constituent atoms have a significant effect on determining NLO properties of this material.

1.3 Present study

In the present study, an attempt was made to see the effect of S and Se substitution on determining the structural, electrical and optical properties of $AgGa(Se_{2-x}S_x)$ thin films for x = 0 ($AgGaSe_2$), x = 1 ($AgGa(Se_{0.5}S_{0.5})_2$), and x = 2 ($AgGaS_2$).

$AgGaSe_2$ thin films were deposited by both electron-beam (e-beam) and sputtering techniques. The e-beam evaporated thin films were produced onto the soda lime glass substrates from the powder extracted from the single crystal $AgGaSe_2$ grown by Bridgman method. Following the deposition of films, the effect of annealing (between 300-600 ^oC) on structural, electrical, and optical properties have been investigated. The same compound is deposited from the Ag and GaSe targets by using RF and DC magnetron sputtering to deposit the GaSe and Ag thin films layers. From the sequential deposition of GaSe/Ag/GaSe/Ag/GaSe/Ag/GaSe/Ag/GaSe layers onto the soda lime glass substrates, $AgGaSe_2$ thin films were prepared. Then, the post-annealing in the range of 350-600 ^oC was carried out and the effect of annealing on physical properties of films were studied in detail.

The $AgGa(Se_{0.5}S_{0.5})_2$ thin films have been deposited onto the soda lime glass substrates by thermal evaporation method using the sintered crystal powder as an

evaporation source. In order to determine the effect of heat treatment on properties of deposited thin films, they were annealed in temperature range of 300-600 ^{o}C for 30 min under the inert gas flow.

Thin films of compound with Ag-Ga-S (AGS) system were prepared by using $AgGaS_2$ single crystalline powder obtained from Bridgman method and deposition of the excess silver (Ag) intralayer with double source thermal evaporation method. The systematic optimization to obtain single phase of $AgGaS_2$ thin films was carried out by changing the thickness of excess silver layer. As a consequence of this process, Ag(Ga,S) with the stoichiometry of $AgGa_5S_8$ and $AgGaS_2$ were obtained and systematic study to reveal structural, electrical and optical properties was carried out.

This thesis was divided into four main chapters. In the first chapter, the theoretical background about the thin film growth process and characterization techniques has been introduced. It is followed by chapter 3 in which a detailed explanation of measurement systems and main stages of thin film deposition using thermal evaporation, electron-beam and sputtering techniques to deposit $AgGa(Se_{0.5}S_{0.5})_2$, $AgGaSe_2$ and $AgGaS_2$ thin films have been presented. Chapter 4 deals with the results obtained for the deposited films as a consequence of conducted several type of structural, electrical and optical characterization measurements. And, finally, in chapter 5, the important results obtained for these materials have been stressed.

CHAPTER 2

THEORETICAL CONSIDERATIONS

2.1Introduction

In this chapter, the theoretical basis behind the thin film growth and structural, electrical, and optical characterization techniques are introduced in detail.

2.2 Thin Film Growth

Thin film technology is playing an important role in development of many industries, such as microelectronics, optoelectronics, and telecommunication. The microelectronic is still the major thin film science exploited area. But, the applications in other fields like optical and magnetic devices, electrochemistry, and coating for decoration, solar energy, data-storage are also growing very rapidly.

Usually one defines thin films as a liquid or solid linear dimension of which is very small in comparison with the other two dimensions [42]. Thin films have been attracting much attention mostly due to their quite difference properties with respect to corresponding bulk material. That is, there are large difference between the properties of the same material in the thin film and bulk form. The thickness of the thin film layers can be ranged from nanometer to several micrometers depending on the application. Thin films are deposited onto a substrate or previously deposited layers to obtain the features not achievable by substrate itself. The properties of films are closely associated with the thickness and conditions under which they were grown and deposition technique.

Fabrication of a thin film is consisted of several main stages. The first stage is the determination of the substrate onto which the film will be deposited. The next stage is the deposition of material onto the substrate from liquid, vapour or solution.

And, the final stage is the formation of structure of the deposited film depending on the constructed bonds with the deposited material and substrate surface. Based on these considerations, several type of thin film growth models have been developed. These are Weber (island growth) [43], Frank-Van der Merwe (layer growth) [44], and Stranski-krostanov (layer + islands) [45] models, which are depicted in Fig. 2.1.

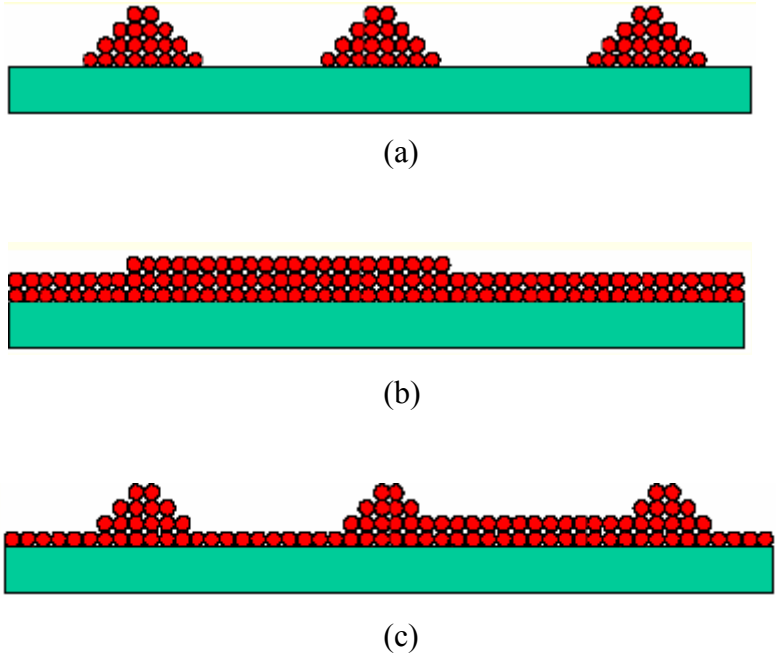

Figure 2.1: Thin film grow models: (a) Volmer-Weber (island growth), (b) Frank-Van der Merwe (layer growth), and (c) Stranski-krostanov (layer + islands).

Various methods can be employed for the production of thin films, which are commonly classified under the following headings:

1. Physical vapor deposition (PVD)
    - Evaporation
        - Thermal evaporation
        - Electron-beam evaporation
    - Sputtering
        - Direct current (DC) sputtering
        - DC magnetron sputtering

- Radio frequency (RF) sputtering

2. Chemical vapor deposition (CVD)
    - Low-pressure CVD (LPCVD)
    - Plasma-Enhanced CVD (PECVD)
    - Atmosphere-pressure CVD (APCVD)
    - Metal-organic CVD (MOCVD)

CVD is a gas transporting reaction based method widely used for the material-processing technology. It has been used to produce a large variety of high-purity bulk materials, powders and thin film coating surfaces. CVD process involves a heated substrate onto which a solid material deposited via chemical reaction in gas phase. Thin film growth process by CVD techniques includes several major stages summarized below and shown in Fig. 2.2 [46]:

- Introduction of precursors gases to the chamber
- Decomposition of introduced gases by either heat or plasma
- The absorption of gases by substrate surface
- Reaction of absorbed components on substrate surface
- Expel of byproducts from the surface

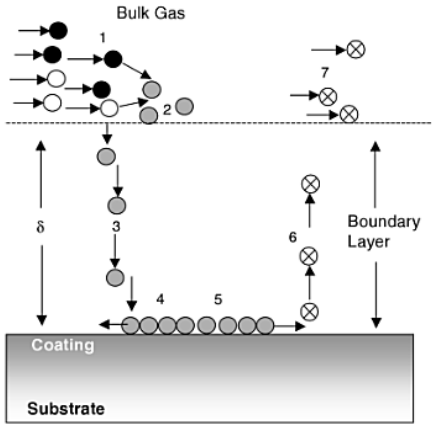

Figure 2.2: Schematic diagram of major steps in CVD process: (1) transport of reactants into the chamber, (2) intermediate reactants, (3) diffusion of reactants to the substrate, (4) absorption of gases onto the substrate surface, (5) reactions at substrate surface, (6) desorption of byproducts from the substrate surface, and (7) expel of byproducts from the system.

This technique provides some special features such as convenience for epitaxial growth, high growth rate, and suitability for deposition of materials that have evaporation problems. On the other hand, this technique is experimentally quite complex and sophisticated [42].

The physical vapor deposition (PVD) methods offer much more flexibility in terms of the material to be deposited and the substrate to be used with respect to CVD techniques. All PVD methods involve a common process, which is the ejection of source particle into vacuum by a number of physical processes that assign the name of method [47]. The deposition process by PVD techniques includes three major steps [42]:

- Ejection of particles from source to be deposited
- Transport of ejected species to the substrate
- Condensation of species on the surface of substrate

The whole process is taking place in a vacuum atmosphere to allow the particle travel to the substrate without scattering and reacting with medium particles between source and target as much as possible.

Of all the known PVD techniques the thermal (resistive) evaporation is the one that has the largest background and history. It is a quite simple and powerful technique for the deposition of a large number of materials [47]. A schematic representation of a thermal evaporation system is shown in Fig. 2.3 [48]. For the evaporation of the particles from the source placed in a boat (crucible), a current is passed through a resistive wire wrapped around the crucible containing the material to be deposited. To deposit a material by resistive heating evaporation method, the heated source must be molten firstly, which limits the use of this method for the deposition of materials with high melting points. The attainable maximum temperature of the source material is limited by the boat's melting point. On comparing with other PVD methods, thermal evaporation is quite simple and cheap. But, there are some disadvantages such as accessibility and control of growth rate, ability in deposition of materials with high melting point, high possibility of reaction between the heated crucible and contained source material (contamination), and very poor density and weak hardness in deposited films.

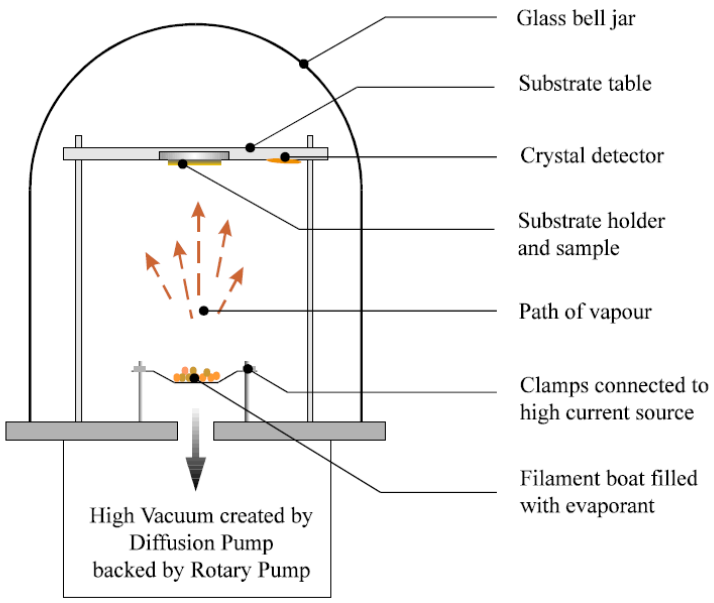

Figure 2.3: Schematic diagram of a thermal (resistive) evaporation system.

One another widely used evaporation method is the electron-beam (e-beam) technique. In the e-beam technique (shown in Fig. 2.4), the boat containing source material is heated by bombarding with high energetic electrons generated by an electron gun. The basic growth steps by e-beam technique can be listed as follow:

- Heating of filament of electron gun till the electron is emitted
- Focusing and directing the generated electron beam to the crucible containing the source material to be deposited by magnetic deflection
- Acceleration of electrons to various energies toward to the crucible for the evaporation of source material.

By way of magnetic deflection mechanism supplied by electromagnets, the localized heating on the material is provided, which eliminates the contamination problem mostly encountered in resistive heating deposition process. Thus, when compared with thermal evaporation method, e-beam technique offers some advantages such as the growing high-pure material, evaporation of materials with high melting point, allowing a good control over the growth rate (particularly it is important for the deposition of compounds), and better uniformity in thickness of the deposited films.

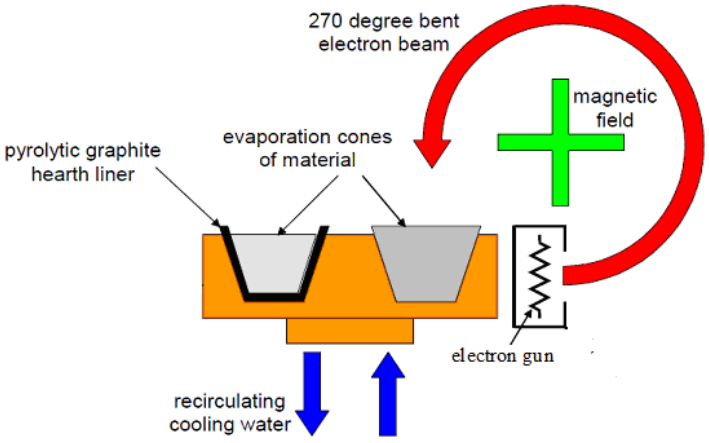

Figure 2.4: Electron-beam heated evaporation system [49]

The sputtering is a process by which the material is ejected from a surface when high energetic atoms or ions strike [50]. The **sputtering** term is aroused from the analogy to the generation of drops out of a liquid surface by impingement the primary drop [42]. The break off the material from the target is accomplished as a result of a momentum transfer from the bombarding particles. A typical sputtering system consists of a vacuum chamber, a target (cathode) and substrate holder (anode). The basic stages in a typical sputtering deposition are listed below:

- Free electrons in chamber are accelerated through the applied voltage to the target and substrate
- Accelerated free electrons interact with inert gas introduced to chamber inelastically and ionize them and generate plasma
- Generated ions are accelerated and directed to the target material to be deposited
- Bombarding the target results in locking out atoms and transporting them to the substrate as a consequence of formed low pressure region near substrate.
- And finally the condensation of sputtered atoms on the substrate grows a thin film.

Sputtering yield, which measures the number of atoms locked out from the target material per incident ion, is the most important parameter in sputtering deposition process owing to its significant role on determining deposition rate.

This quantity depends on several major factors; such as energy and mass of incident ions, target material itself, and type of discharge gas (Ar is the most commonly used gas due to its inertness and low price) used in sputtering process [47]. In sputtering process, it is proved that the yield increases with increasing mass and energy of bombarding ions in energy interval of sputtering for a material. However, at very high energies (>2000 eV) the incident ions penetrate too deeply into the target and results in decrease of yield since the sputtering is a surface phenomenon [47].

Direct current (DC) sputtering (shown in Fig. 2.5) can be applied only for the deposition of conductors. During the deposition cycle of insulators, the incident ion bombardment results in a quick building up of a positive charge on target surface that blocks the impingement of further ions to target. Under these conditions, the deposition of insulating materials would not happen.

For the sputtering of non-conducting materials, radio frequency (RF) sputtering has to be implied. A typical RF sputtering system is depicted in Fig. 2.6 **[**48**]**. In RF sputtering, the target is periodically bombarded (depending on frequency of applied RF power) by ions, and in a full period cycle of pulse the charge built up on the target is neutralized.

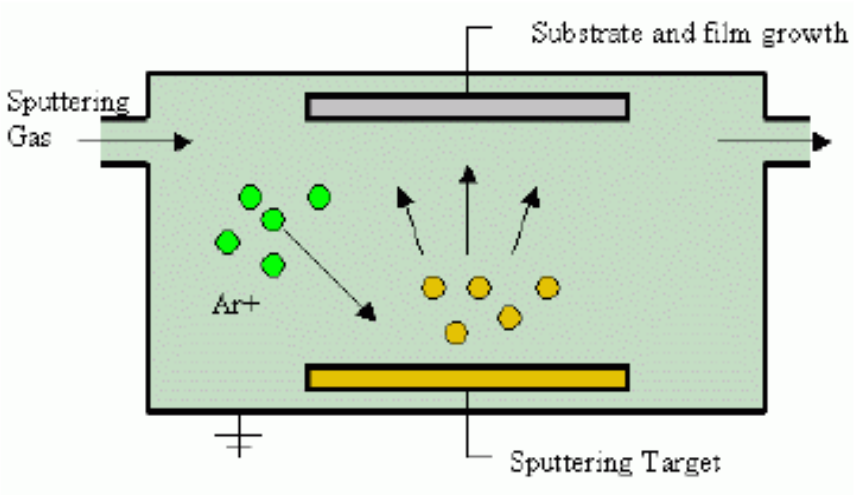

Figure 2.5: Schematic diagram of DC sputtering.

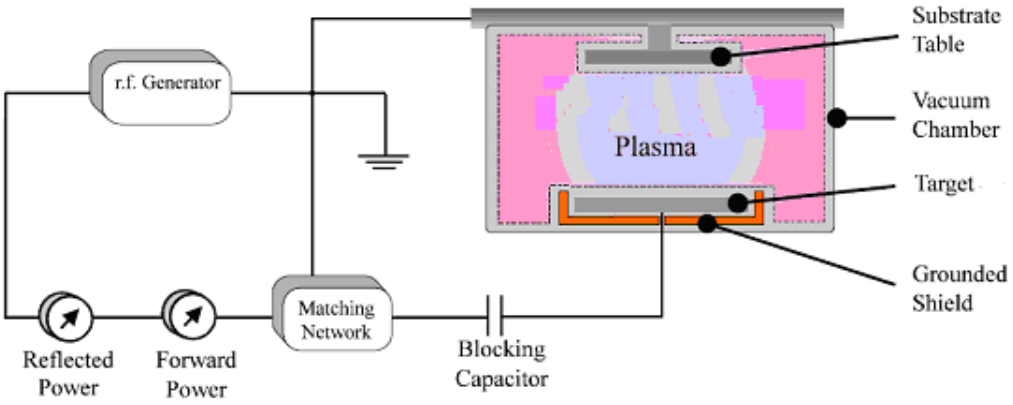

Figure 2.6**:** Schematic diagram of RF sputtering chamber.

By using RF sputtering, it is possible to deposit various dielectric materials, particularly oxides and nitrides. The main drawback in RF sputtering of dielectric targets is that these materials have poor thermal conductivity and usually are brittle. Thus, bombarding target with high energetic ions produces a heat that generates a large thermal gradient, which results in fracturing the target when sputtered at high power levels [51].

Magnetron sputtering (Fig. 2.7) is another technique developed to increase the efficiency of a sputter system by means of the created magnetic field by a permanent magnet which confines the plasma close to the target and hence increases the number of ions for the bombarding the target.

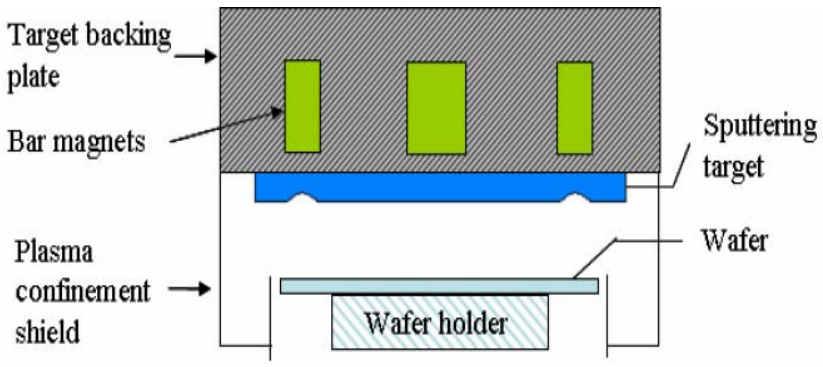

Figure 2.7: DC magnetron sputtering system [52].

In magnetron sputtering, a parallel magnetic field applied to the cathode surface results in electrons near the target surface to sustain plasma. This give rise to increase in current density and subsequently sputtering rate [47]. The main advantage of the magnetron sputtering is that quite intense plasma can be created near the target (cathode) at low pressures that enable ions to accelerate from the plasma to target without loss of energy in connection with inelastic interactions such as charge exchange collisions. This makes it possible to achieve high sputtering rates without applying large potentials on the target, which is the case for the DC sputtering [51]. The disadvantage of magnetron sputtering is that there is no a uniform plasma over the surface of target. Thus, the patterns formed by magnetron sputtering are dependent on the position of samples relative to target.

In summary, on comparing with other PVD methods, sputtering deposition offers some advantages such as the ease at deposition of materials having even the highest melting point, a better adhesion of films to substrate, a good control on thickness of deposited films, and control of the alloy composition.

2.3 Material Characterization Techniques

2.3.1 Surface Analysis Methods

The information obtained from the interaction of materials with their environment by means of their surfaces is indispensible for the development of semiconductor technology [53]. To investigate the surface properties of solid state materials a number of surface-sensitive characterization techniques are employed, such as Auger electron spectroscopy (AES), scanning Auger electron microscopy (SAEM), secondary ion mass spectroscopy (SIMS), Rutherford backscattering spectroscopy (RBS), and X-ray photoelectron spectroscopy (XPS) [54]. By using these tools useful knowledge about the surface states, surface composition, thin film multilayer structure, and surface topography can be obtained. For the investigation the chemical bonding nature and composition of surface or near-surface region of deposited thin films, we have carried out XPS measurements, detailed theoretical background of which is provided in subsequent subsection.

2.3.1.1 X-ray Photoelectron Spectroscopy (XPS)

X-ray photoelectron spectroscopy, known also as electron spectroscopy for chemical analysis (ESCA), is a powerful surface-sensitive technique for the determination of chemical composition of materials. It is accomplished by irradiating a sample with X-rays for the excitation of the material and energy analyzing of emitted photoelectrons [54]. Schematic illustration of this process is shown in Fig. 2.8 [55].

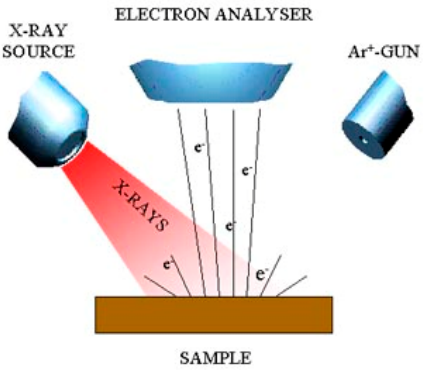

Figure 2.8: Schematic diagram of XPS process.

The source used for the soft X-rays are generally MgK_{α} (1253.6 eV) or AlK_{α} (1486.6 eV). Depending on the matrix of atoms in structure of materials, incident X-rays can travel in solids from 1 to 10 nm. The kinetic energy (E_k) of the emitted photo-electron can be calculated through the Einstein photoelectronic relation; $E_b=h\nu-E_k-W$. Here, E_b is the binding energy (a measure of energy strength of interaction between electron and atom's nuclear charge) of the electron to a particular atom in the material, $h\nu$ is the incoming photon energy, and W is the spectrometer work function [53-54]. It is possible to evaluate the binding energy of an electron on condition that its kinetic energy is known.

Since for each element there is a characteristic binding energy of an electron associated with specific atomic orbital (s, p, d, f, etc.), by using the XPS measurement one can identify the elements present in the material. The concentration

of them can also be measured since the intensity of the photoelectron lines is taken as the measure of this quantity.

The energy of liberated electrons from the sample is much less than 1 keV, and the most of the photoelectrons are collected from a depth of 20 Å below the surface and this is the reason of this technique to be called as surface sensitive [54]. Due to the coulombic interaction between electron and its surrounding there is an important effect of atomic environment on binding energy of an electron. This interaction results in shifting in binding energy of electrons and give rises to the identification of bonds an atom constructing with surrounding atoms and subsequently revealing the compounds present in the structure [54].

For the non-conducting materials, a positive charge is built up in the sample surface following to the ejection of electrons from the specimen under X-ray irradiation and results in lowering the kinetic energy of liberated electrons due to the coulombic interaction taking place between surface charge and electrons. To eliminate the effect of surface charging on shifting binding or kinetic energy, the correction is done based on the calibration of the binding energies with known reference binding energy of photoelectron line (in general, C 1s (284.6 eV)).

Table 2.1: The relations between quantum numbers and labeling notations

Quantum numbers					
n	l	s	j	Spectroscopists' notation	X-ray notation
1	0	+1/2, -1/2	1/2	$1s_{1/2}$	K
2	0	+1/2, -1/2	1/2	$2s_{1/2}$	L_1
2	1	+1/2	1/2	$2p_{1/2}$	L_2
2	1	- 1/2	3/2	$2p_{3/2}$	L_3
3	0	+1/2, -1/2	1/2	$3s_{1/2}$	M_1
3	1	+1/2	1/2	$3p_{1/2}$	M_2
3	1	- 1/2	3/2	$3p_{3/2}$	M_3
3	2	+1/2	3/2	$3d_{3/2}$	M_4
3	2	- 1/2	3/2	$3d_{5/2}$	M_5

In XPS spectra photoelectrons are described by labels defining the electrons involved in the transition between states in an atom during the material and X-ray interaction. Labeling is established either by X-ray or spectroscopists' notation as given in Table 2.1 [53]. Among these labelings, the most commonly used one is the spectroscopists' notation. In this notation photoelectrons are represented by n, l, and j standing for the principal quantum number (taking values of 1, 2, 3, etc.), orbital angular momentum, and total angular momentum, respectively. The orbital angular momentum (l) is commonly represented by a letter associated with its value as listed in Table 2.2 [53].

Table 2.2: Notation of quantum numbers associated with orbital angular momentums

Value of l	Usual notation
0	s
1	p
2	d
3	f

Some photoelectron lines originating from orbital having orbital angular momentum greater than zero are appeared as doublets in XPS spectra. This originates from the interaction between the electron orbital and spin orbital angular moments. In quantum mechanics, it is known that each electron has either +1/2 or -1/2 spin angular momentum (s) value. Total angular momentum (j) is calculated from the addition of orbital and spin angular momentums through the $j = |l + s|$ relation. Electron ejected from the p orbital, for instance, can have ½ or 3/2 total angular momentum resulting in two peak associated with each angular momentum ($p_{1/2}$ and $p_{3/2}$) appeared as a doublet in spectrum . The relative intensity of doublets is determined by their degeneracy defined by 2j+1. Thus, the relative intensity of a doublet of 3/2 and 5/2 originating from a d orbital is 2:3.

Following to the ejection of electrons after excitation, the ionized atom can be relaxed in several ways. One of them is the emission of Auger electron.

In this process, the unoccupied level (let's say K level) is filled by an electron from a higher energy level (L), and the energy given off by this transition is absorbed for the liberation of a secondary electron (let's say in L level) called Auger electron and labeled by KLL in XPS spectrum.

The characterization of the surface of specimen under investigation is established by following to several major analyzing stages. The first step is the recording of the survey scan spectrum for the related sample region and identification of elements present in sample by comparison of the obtained binding energies (after calibration of binding energy values due to the chemical shift and surface charging) with the values reported in database. For the identification of chemical bonds, a more complex stage is required. The first step in this process is the elimination of background stemming from the inelastic interaction of ejected electrons in atomic matrix structure resulted in kinetic energy loses by applying appropriate background model such as Tougard. Then, the determined photoelectron peak is deconvoluted into its component parts by applying most convenient fitting functions like Gaussian and Lorentzian. The other major stage in analyzing is the checking of the spin doublets for the p, d, and f lines. The intensity ratio for them should preserve the correct values, which are 1:2, 2:3, and 3:4, respectively. For the identification of chemical states of each element, the most intense core level peak is deconvoluted into its components. The identification of chemical states of determined element is accomplished by comparing the calculated binding energies of each component with reported state values by taking the chemical shift into account. Furthermore, the relative amount of present phases in specimen is revealed from the relative area under each component state. So, following all these complex analyzing stages, XPS measurement can reveal important surface properties of a material like the identification of elements present at the surface, chemical state of elements, quantity of chemical state of each element, spatial distribution of the material in 3-D, and concentration of element present in the material [53].

2.3.2 Microscopy Techniques

Microscopy techniques play an important role in many respects in characterization of semiconductors. The most widely used microscopy techniques are optical microscopy, electron microscopy, and scanning probe microscopy [54]. When compared with other microscopy techniques, optical microscopy offers significant advantages, such as versatility in examination, ease of sample preparation, no vacuum requirement and sample charging problems [54]. Scanning probe microscopy (SPM) uses mechanically scanable probes for the characterization of materials instead of excitation probes like a photon beam and electron or ion beams used in other techniques and provides high quality surface images of materials on the atomic scale as a consequence of interaction between the mechanically moved a fine probe and a sample. The most commonly used electron microscopy techniques are the scanning electron microscopy (SEM) and transmission electron microscopy (TEM) that provide much valuable information related to the compositional, structural and defects in the structure of materials. The following subsection introduces a detailed theoretical background about the basic principles and applications of scanning electron microscopy.

2.3.2.1 Scanning Electron Microscopy (SEM)

Scanning electron microscopy (SEM) is a strong tool for the determination of structural, physical and compositional properties of solid state materials and devices [54]. A typical SEM system consists of an electron gun (creating electron beam), sample chamber (providing electron beam-sample interaction), several types of detectors for different applications (for detecting signals resulting from the beam-specimen interaction), and monitoring system (performing the image), which is schematically presented in Fig. 2.9 [56]. When the specimen is bombarded by accelerated high energetic electrons, it results in a series of interaction with the nuclei and electrons of the specimen. This interaction give rise to change in direction of incident electrons (scattering) and gradual lose of energy of electrons. Scattering may be both elastic and inelastic, which results in deflection of incoming electrons by nuclei of atoms called backscattered electrons and generation of different signals

such as emitting secondary electrons, electron-hole pairs, Auger electrons and characteristic X-rays, respectively [54]. The penetration depth of incident electrons depends on accelerating voltage and increases with increasing energy of energy incident electrons. In addition, it is known that the volume of interaction varies inversely with the atomic number of the sample determined [57]. Electron-specimen interaction origin generated secondary electrons, back scattered electrons, and characteristic X-rays provide surface morphology, composition contrast, and elemental analysis, respectively [54].

A SEM equipped with energy dispersive X-ray analysis (EDXA) component determines the chemical composition of material on the micro- and nano scale by measuring the X-rays emitted during the electron-specimen interaction. The origin of the emitted characteristic X-rays is the change in the speed of bombarded electrons. By measuring the energies of X-rays emitted from the excited sample, the elements present in this region are qualitatively determined. The relative intensity of these characteristic X-rays is the measure of the atomic percentage of present constituent elements in the materials. So, by scanning the over all sample area it is possible to reveal spatial elemental mapping of the material.

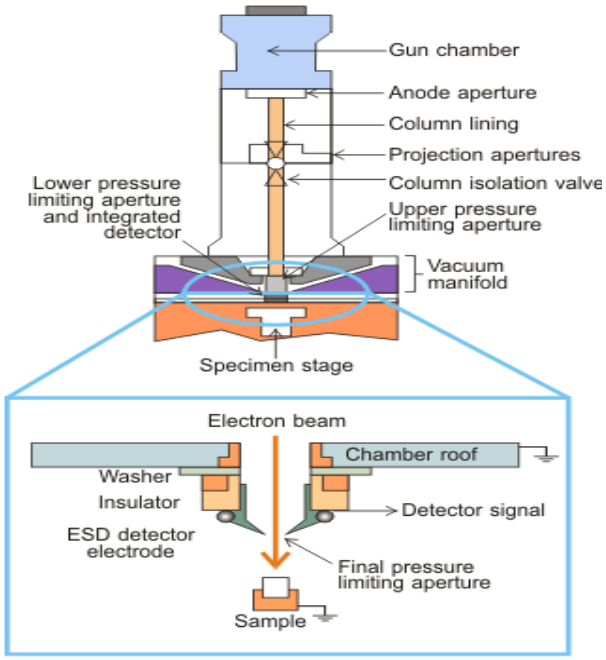

Figure 2.9: Schematic representation of an SEM image.

2.3.3 Structural Characterization

The determination of structural properties of solid state materials can be performed by several analytical techniques such as X-ray diffraction, neutron diffraction analysis, electron microscopy and electron diffraction. By using these techniques, it is possible to calculate lattice parameters, identify the phases exist in the structure, reveal crystalline state (crystalline, polycrystalline or amorphous), detect defects and stress present in the structure. To determine these parameters we have carried out X-ray diffraction technique theoretical background of which have been presented in detail in following subsection.

2.3.3.1 X-ray Diffraction Technique

X-rays are electromagnetic waves having energies ranging from 200 eV to 1MeV. They can be used for the identification of structural parameters when interacted with a solid state material in several ways (absorbed, emitted, reflected or transmitted). It is known that when X-rays interacts with a material having an ordered structure (crystalline phase), a diffraction pattern is formed. This pattern can be taken as the fingerprint of a substance and gives valuable information about the structure of a material. In the case of incident of X-rays on a crystalline substance, a constructive interference is taking place in specific orientations and results in generation of well-defined X-ray diffraction patterns. The constructive interference is the result of reinforcement of reflection of X-rays from the periodically distributed parallel planes consisting of the structure of a material. The orientation and inter-distance of parallel planes are represented by the h, k, and l indices. A (h, k, l) plane stands for the intersection of unit cell's a-axis in h sections, b-axis in k sections and c-axis in l sections, respectively [58]. A unit cell can be regarded as the smallest volume element repetition of which in three dimensions can construct all the structure. The specification of a unit cell is done by three axes (a, b, and c) and angles (α, β, and γ). It is possible to imagine many unit cells with different shapes. However, the requirement of filling the three-dimensional space by stacking of

smallest volume element allows only to seven unit-cells composing the known seven crystal systems given in Table 2.3 [59].

Table 2.3: Crystal systems

System	Crystal system	Angles
Triclinic	$a \neq b \neq c$	$\alpha \neq \beta \neq \gamma \neq 90^o$
Monoclinic	$a \neq b \neq c$	$\alpha = \beta = 90^o\ \gamma \neq 90^o$
Orthorhombic	$a \neq b \neq c$	$\alpha = \beta = \gamma = 90^o$
Tetragonal	$a = b \neq c$	$\alpha = \beta = \gamma = 90^o$
Hexagonal	$a = b \neq c$	$\alpha = \beta = 90^o, \gamma = 120^o$
Trigonal	$a = b = c$	$\alpha = \beta = \gamma \neq 90^o$
Cubic	$a = b = c$	$\alpha = \beta = \gamma = 90^o$

To observe diffraction after incident of X-rays on crystalline material (shown in Fig. 2.10) several conditions should be satisfied.

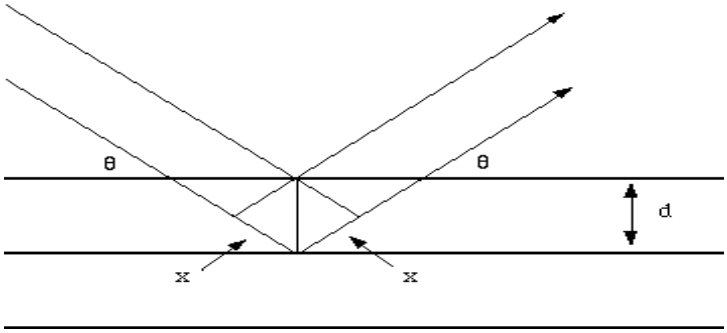

Figure 2.10: Diffraction of X-rays from parallel planes.

One of these conditions is that the angle between the incident beams and reflecting planes should be equal to that of diffracted beam and reflecting planes.

Another condition is that the incident and reflected waves from planes should be in phase and the difference in path lengths have to be an integral number of wavelengths. These conditions are expressed in Bragg's Law:

$$n\lambda = 2d\sin\theta \tag{2.1}$$

where n, λ, d, and θ are the order of diffracted beam, wavelength of the incident X-ray, inter-planar spacing of parallel planes, and Bragg's angle, respectively. Depending on varied parameters in Bragg equation X-ray diffraction techniques called with different names, such as Laue, rotating crystal, and powder diffraction. Powder diffraction is the most widely used technique and the varied parameter is the angle [58].

From the obtained peak positions, intensity, peak-width and shape much valuable knowledge about the crystal structure of a material can be obtained. Phase identification is done by comparing the peak position 2θ values and inter-planar spacing with the known standards JCPDS (joint committee on powder diffraction standards) files supplied by XRD measuring systems' suppliers. To determine the strain in the structure the shift in the position of the diffracted peaks is taken into account. In addition, having measured the full widths at half maximum (FWHM) of diffracted peaks, it is possible to calculate the grain size of crystals through the Scherrer's formula [60]

$$d = \frac{0.9\lambda}{\beta\cos\theta} \tag{2.2}$$

where β, θ, and λ are FWHM, Bragg's angle, and wavelength of the X-rays, respectively. Moreover, XRD is also used for the determination of the thickness of thin films by measuring the space between the primary and secondary or subsidiary maxima diffraction peaks [61].

2.3.4 Electrical Characterization

2.3.4.1 Electrical Conductivity

The electrical conductivity of a material can be defined as the measure of how well a material conduct electric current. It can be measured by using several techniques such as the four-point probe and van der Pauw. Using one of these, it is possible to derive the resistivity.

Since the contribution to current in a semiconductor coming from both electrons and holes the conductivity (σ) can be expressed as

$$\sigma = n\, e\, \mu_e + p\, e\, \mu_p \tag{2.3}$$

Here, μ is the mobility and defined as $\mu = \upsilon_d/E$ where υ_d is the drift velocity and E is the applied electric field. In addition, n and p in eqn. (2.3) are the free electron and hole concentrations, respectively. For the intrinsic semiconductors, the concentration of electrons in conduction band (n) and holes in valance band (p) is equal and expressed by the following relation:

$$n = p = constant\ x\ T^{3/2}\ exp[(-E_g)/2k_BT] \tag{2.4}$$

where T, k_B, and E_g are absolute temperature, Boltzmann constant, and energy band gap, respectively. From the eqns. (2.3) and (2.4), conductivity can be written as

$$\begin{aligned}\sigma &= constant\ xe\ (\mu_e+\mu_h)\ T^{3/2}\ exp[(-E_g)/2k_BT] \\ &= \sigma_o\ exp[(-E_g)/2k_BT]\end{aligned} \tag{2.5}$$

where σ_o is the pre-exponential factor. The band gap energy value (E_g) can be derived from the slope of the curves of Ln σ versus T^{-1} [54].

2.3.4.2 Hall Effect

Hall effect measurement is a strong electrical characterization technique employed for the determination of free carrier density, carrier type, and the mobility of a

semiconductor. The Hall effect system is consisted of a conducting material through which a current (I) flows perpendicular to the applied magnetic field (B) as shown in [62].

As a result of deflection of moving charges by the Lorentz force, an electric field is generated perpendicular to both the current and applied magnetic field. The current flow through the p-type material is expressed by

$$I=qwdpv_x \tag{2.6}$$

And, the voltage along the x-axis (V_ρ) is given as

$$V_\rho = \frac{\rho sI}{wd} \tag{2.7}$$

and from this expression the resistivity (ρ) can be derived as

$$\rho = \frac{wdV_\rho}{sI} \tag{2.8}$$

where w, d, and s are the width, the thickness of the sample, and distance between two contacts.

In the presence of external magnetic field applied perpendicular to current direction, the moving charges (holes in our case) experiences Lorentz force in y-direction given by the vector expression

$$\vec{F} = q\left[\vec{E} + \vec{v}x\vec{B}\right] \tag{2.9}$$

and collected at the bottom of specimen and develops a Hall voltage (V_H) perpendicular to current and magnetic field. Since there is no net force on moving charges in y-direction due to the absence of a current in that direction, the electric

field in y-direction (E_y) is zero. From the eqn. (2.6) and (2.9), the vertical electrical field can be derived as

$$E_y = \frac{BI}{qwdp} \tag{2.10}$$

from which the Hall voltage (V_H) is derived as

$$V_H = -\int_0^w E_y dy = \int_0^w \frac{BI}{qwdp} dy = \frac{BI}{qdp} \tag{2.11}$$

The Hall coefficient (R_H), which is negative and positive for the *n*-type and *p*-type material, respectively, is defined as

$$R_H = \frac{(dV_H)}{BI} \tag{2.12}$$

From the combination of eqn. (2.11) and (2.12), the hole (p) and electron (n) concentrations for *p*- and *n*-type materials are found through the following relations

$$p = \frac{1}{qR_H} \tag{2.13}$$

and

$$n = -\frac{1}{qR_H} \tag{2.14}$$

respectively. In addition, provided that the conductivity is known, Hall mobility can be determined as [62]

$$\mu_H = \sigma R_H \tag{2.15}$$

Therefore, when the conductivity and Hall effect measurements are combined, the free carrier concentration, type of the conduction, and mobility can be determined.

2.3.5 Optical Characterization

Semiconductors can interact with light in many ways and result in formation of different process such as absorption, transmission, reflection, and scattering as shown in Fig. 2.11 [63]. By measuring signals originated from the incident light-specimen interactions much valuable information about the optical properties of materials can be gathered. There are many optical instruments designed for the identification of optical properties of semiconductors. Optical characterization techniques are contactless and non-destructive techniques allowing the in-situ characterization during production process such as thin film deposition process [54]. The main optical characterization techniques are optical microscopy, optical absorption, photoluminescence, Raman spectroscopy, and optical modulation techniques.

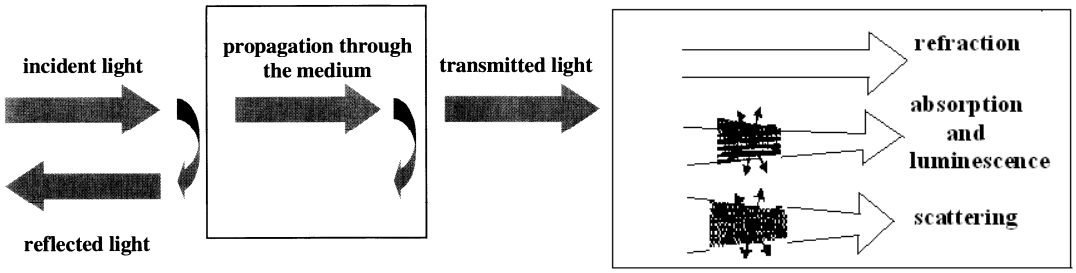

Figure 2.11: Several type of interaction of light with matter

2.3.5.1 Optical Absorption

To determine the band structure of materials optical transmission and reflection or absorption are the most preferred measurement techniques. The absorption mechanism includes the excitation of electrons by means of incident photons from the lower to higher energy levels. The absorption process can be performed through multiple mechanisms like band to band, interconduction band, intervalence band, donor to conduction band, acceptor to conduction band, valence

band to donor, acceptor to conduction band, and donor to acceptor transitions that contribute to the total absorption coefficient (α) as shown in Fig. 2.12 [64]. It is the magnitude of the incident photon energy that determines which absorption mechanism will occur. That is, if the incident photon energy is greater than the band gap, the electrons from valance band is excited to conduction band's empty states and called as the *fundamental absorption*. This type of transition results in a significant rise in the absorption coefficient at photon energies close to the band gap.

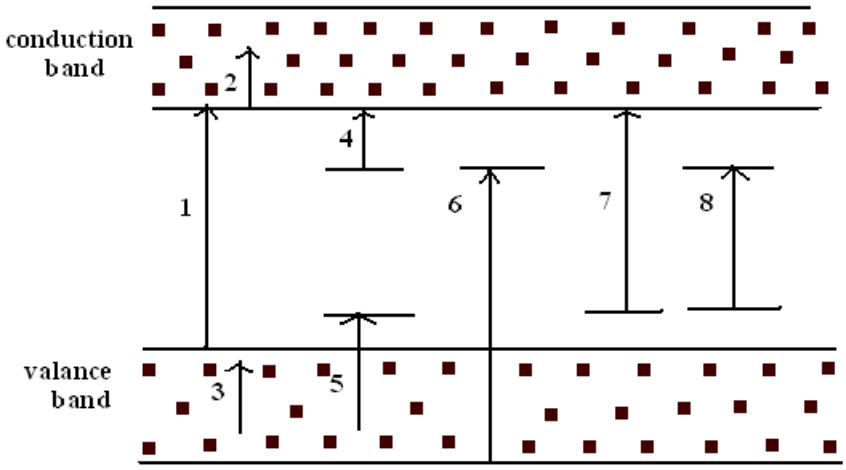

Figure 2.12: Different absorption processes in semiconductors: (1) band to band, (2) interconduction band, (3) intervalence band, (4) donor to conduction band, (5) acceptor to valance band, (6) valance band to donor, (7) acceptor to conduction band, and (8) donor to acceptor transitions.

However, when the photon energy is lower than the band gap, it results in absorption by either *excitons* (electron-hole bound pairs) or transitions between impurity or defect states (acceptor or donor) and band states (conduction or valance bands). In the case of *interconduction* and *intervalence band* transitions the continuous absorption is taking place at low energies.

In the band to band transition, the absorption can be classified as *direct* and *indirect* absorption depending on the position of the minimum of the conduction band and maxima of the valance band in the Brillouin zone. During the direct or indirect transitions the law of conservation of momentum and energy must be conserved. The distinction between direct and indirect band gap is illustrated in Fig.

2.13 [63]. The transition is called *direct* (direct band gap semiconductor) when the band extremes are at the same momentum vector ($\vec{k}$) value, and it is called *indirect* (indirect band gap semiconductors) if they are not at the same momentum wave vector. The momentum conservation in indirect transition is preserved by accompanying of a phonon as illustrated in Fig. 2.13. The requirement of involving phonons (q) in indirect band gap structure lowers the transition probability and subsequently results in a weak absorption with respect to direct band gap materials [54].

The absorption coefficient (α) can be calculated through the transmission (T) and reflection (R) spectra by using the following formula:

$$T = \frac{(1-R)^2 \exp(-\alpha d)}{1-R^2 \exp(-2\alpha d)} \tag{2.16}$$

where I, I_o, and d are the transmitted light intensity, incident light intensity, and the thickness of the specimen, respectively.

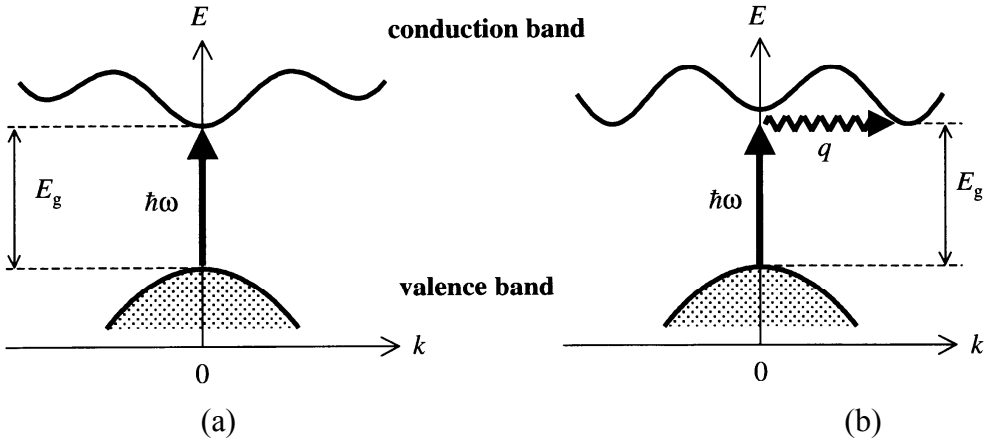

Figure 2.13: (a) Direct band gap, and (b) indirect band gap

This expression is simplified for the large (αd) values as

$$T = (1-R)^2 \exp(-\alpha d) \tag{2.17}$$

If we neglect reflection, the expression can be further simplified to

$$T = \exp(-\alpha d) \tag{2.18}$$

The absorption coefficient can also be found from the following relation [65]

$$\alpha(h\nu) = A\sum p_{if} n_i n_f \tag{2.19}$$

where A, P_{if}, n_i, and n_f are a constant, transition probability from the initial state to the final state, density of electrons in the initial state, and density of empty states in the final states respectively.

The energy of electron and hole relative to conduction and valance band are

$$E_e = \frac{\hbar^2 k^2}{2m_e^*},\ E_h = \frac{\hbar^2 k^2}{2m_h^*} \tag{2.20}$$

The direct transition energy can be expressed as

$$h\nu - E_g = \frac{\hbar^2 k^2}{2m_e^*} + \frac{\hbar^2 k^2}{2m_h^*} = \frac{\hbar^2 k}{2m_r^*} \tag{2.21}$$

where $m_r^* = \frac{m_e^* m_h^*}{m_e^* m_h^*}$ is the reduced effective mass.

The density of state (DOS) is given by the standard formula:

$$N(E)dE = \left(2\pi^2\hbar^3\right)^{-1}\left(2m^*\right)^{\frac{3}{2}} E^{\frac{1}{2}} dE \tag{2.22}$$

So, by replacing this expression into eqn. (2.21) we get the absorption coefficient for the direct transition between the parabolic bands as

$$\alpha(h\nu) = A\left(h\nu - E_g\right)^{1/2} \tag{2.23}$$

where A and E_g are constant ($A \sim 10^4$), and band gap energy, respectively [54, 66].

For the indirect material, the momentum conservation is preserved via either phonon emission or absorption. In the case of phonon absorption indirect transition, the absorption coefficient is expressed by [65]

$$\alpha_a(h\nu) = \frac{A\left(h\nu - E_g + E_p\right)^2}{\exp\left(\frac{E_f}{k_B T}\right) - 1} \tag{2.24}$$

And, for the phonon emission indirect transition, it is given by

$$\alpha_e(h\nu) = \frac{A\left(h\nu - E_g - E_p\right)^2}{1 - \exp\left(\frac{-E_p}{k_B T}\right)} \tag{2.25}$$

where E_p, T, and k_B are involved phonon energy, absolute temperature, and Boltzmann constant, respectively. So, the total absorption coefficient for $h\nu > E_g + E_p$, the absorption coefficient can be calculated through the following relation;

$$\alpha(h\nu) = \alpha_a(h\nu) + \alpha_e(h\nu) \tag{2.26}$$

2.3.5.2 Photoconductivity

The photoconductivity is defined as the change in conductivity of a material when exposed to light. When the materials are illuminated with light having energy greater than the band gap, electrons and holes are generated in conduction and valance bands, respectively. The photogenerated electron and holes contribute to the increase

in the conductivity of materials. Then, the free carriers created by incident photons of energy lower the band gap result in the transition of impurity level to band edge, ionization of donors and acceptors, and deep level to conduction band. It also results in starting of photoresponse spectrum from the low energy side of band gap [67]. As it is stated before, the dark conductivity is given by

$$\sigma_o = e(n_o\mu_o + p_o\,\mu_h) \tag{2.27}$$

where n_o and p_o are the densities of free electron and holes, respectively, and μ_e and μ_h are the electron and hole mobilities. When a homogenous material is exposed to light, the photogenerated electron and holes results in an increase in conductivity given by

$$\Delta\sigma = e\,(\Delta n\mu_o + \Delta p\,\mu_h) \tag{2.28}$$

where Δn and Δp are the increase in the free electron and hole concentration, respectively [68]. For an intrinsic semiconductor, the number of created electrons in conduction band is equal to that of holes in valance band, which results in Δn = Δp equality. This equality reduces the eqn. (2.28) to

$$\Delta\sigma = e\Delta n\,(\mu_o + \mu_h) \tag{2.29}$$

For the simplifying assumption of only one carrier type, let's say n-type, the conductivity in the dark and under light can be given by

$$\sigma_o = en_o\,\mu_o \tag{2.30}$$

and

$$\sigma_o + \Delta\sigma = (n_o + \Delta n)e(\mu_o + \Delta\mu) \tag{2.31}$$

respectively. Here, Δn and Δμ are the change in electron concentration and mobility, respectively. Using eqns. (2.30) and (2.31), the change in conductivity can be written as

$$\Delta\sigma = e\,\Delta n\,\mu_o + (n_o + \Delta n)e\Delta\mu \tag{2.32}$$

The photogenerated charge carrier density can be written as

$$\Delta n = G\,\tau_n \tag{2.33}$$

Where G and τ_n are the photogeneration rate (photo-excitation rate) and electron lifetime, respectively. So, the eqn. (2.32) for the change in conductivity under light can then be rewritten as

$$\Delta\sigma = e\,\Delta\mu\,n + eG\,\tau_n\,\mu_o \tag{2.34}$$

The lifetime (τ) is an important parameter for the understanding of photoconductivity. There are a numbers of types of term lifetime used in literature such as free, excited, pair and minority-carrier lifetimes [69], which must be well distinquished. Here, we are concerned with the free lifetime defined as the time the charge carrier spends in either valance or conduction band (i.e, time of excited electrons in conduction band and holes in valance band). The lifetime is limited due to the existing of recombination and trap centers in the structure. Thus, the density of trap and recombination centers have an important effect on determining the lifetime. The photoconductivity defined in eqn. (2.34) can be analysed based on some simplfiying assumptions. One of them is the thinking of lifetime to be a function of excitation intensity (G). In this approxiamtion, equation (2.34) can be written as

$$\Delta\sigma = G\,\tau_n\,e\,\mu_o \tag{2.35}$$

provided that mobility and lifetime is not changing on illumination. Thus, if τ_n changes as $G^{\gamma-1}$, the $\Delta\sigma$ varies as G^{γ}. We can also say that photocurrent (I_{pc})

(substraction of dark current from the current under illumination) is proportional to G^{γ}. In this specific case, from the slope of Ln (I_{pc}) –Ln (G), the exponent γ can be determined. The value of exponent determines the behavior of photoconductivity. For instance, γ<1 case means that lifetime decreases with increasing light intensity and material behaves as *sublinear*. On the other hand, for γ>1 case the material shows a *supralinear* character meaning that the lifetime increases and material is becoming more photosensitive with increasing illumination intensity. In addition, the calculated γ value determines the recombination mechanisms. The values in the range of 0.5< γ<1 indicates that recombination is dominated by a single type of imperfection level explained by one-center recombination model. The γ = 0.5 and 1 attributed to the existing of *bimolecular* (recombination at surface) and *monomolecular* (recombination in the bulk) recombinations, respectively. Another assumption employed to the eqn. (2.34) is the thinking of that contribution to conductivity on illumination is coming only from the change in mobility. In that case, the eqn. (2.34) reduces to

$$\Delta\sigma = e\,\Delta\mu\,n \tag{2.36}$$

and the change in conductivity is proportional to the change in mobility.

The value of γ is also used to determine the type of model (one-center and two-center models) describing the photoconductivity process. Based on these models one enables to describe many photoconductivity phenomenon, such as sublinear and supralinear photoconductivity, thermal and optical quenching of photoconductivity, negative photoconductivity, and saturation of photoconductivity.

2.3.5.2.1 One Center Model

The one-center model can be represented as in Fig. 2.14.

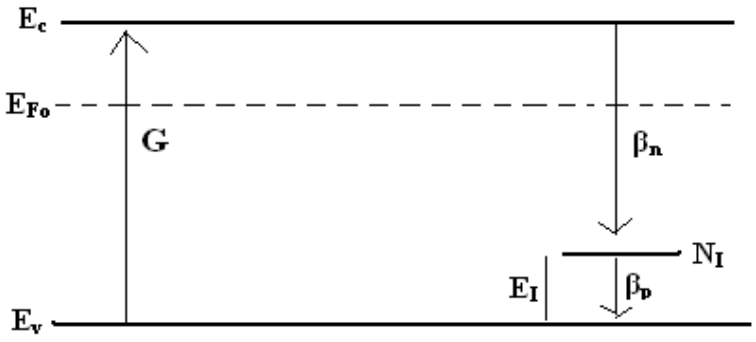

Figure 2.14: One center model.

The transition from the valance band to conduction band is considered to be the only optical excitation in this model. And, only one center with density of N_I and capture coefficient of electron (β_n) and hole (β_p) is dominated. Under the following assumptions:

- No thermal exchange with bands (condition and valance bands)
- No other levels such as traps are considered
- Material is taken as insulator ($\Delta n >> n_o$)
- A fix Fermi level (E_{Fo}) above recombination center (E_I)

the continuity equations can be written as

$$\frac{dn}{dt} = G - n\beta_n\left(N_I - n_I\right) \tag{2.37}$$

$$\frac{dn_I}{dt} = n\beta_n\left(N_I - n_I\right) - n_I p\beta_p \tag{2.38}$$

$$\frac{dp}{dt} = G - n_I p\beta_p \tag{2.39}$$

where, n_I and N_I are the density of electron occupied imperfection levels and density of imperfection level, respectively and β_n and β_p are electron and hole capture

coefficients. Since there are three equations two of which are independent, one more equation is required for the solution of equations. Third equation comes from the requirement of charge neutrality condition expressed as

$$n = p + \left(N_I - n_I\right) \tag{2.40}$$

In steady state, the eqns. (2.39) and (2.40) can be rewritten like that

$$G = n\beta_n\left(N_I - n_I\right) \tag{2.41}$$

$$G = n_I p\beta_p \tag{2.42}$$

Then, by using eqns. (2.40-2.42), the basic relation between the generation rate and n and p can be derived as

$$G = \left(N_I - \frac{G}{n\beta_n}\right)\left(n - \frac{G}{n\beta_n}\right)\beta_p \tag{2.43}$$

$$G = \left(N_I + p - \frac{G}{p\beta_p}\right)\left(N_I - \frac{G}{p\beta_p}\right)\beta_n \tag{2.44}$$

respectively [68]. Since there is a hole in a recombination center for each electron in the conduction band, under the assumption of small values of n or low-intensity photoexcitation n can be written as

$$n \approx \left(N_I - n_I\right) \tag{2.45}$$

and eqn. (2.43) is reduced to

$$G = n^2\beta_n \quad \text{or} \quad n = \left(\frac{G}{\beta_n}\right)^{\frac{1}{2}} \tag{2.46}$$

For large n and high photoexcitation intensity and $\beta_p >> \beta_n$ case, it is thought that all recombination centers are empty and

$$n = p \propto G \tag{2.47}$$

2.3.5.2.2 Two Center Model

Two center model, unlike one center model, includes two recombination centers with quite different capture coefficients for at least one type of carrier as shown in Fig.2.15. For the n-type material with two recombination centers below the dark Fermi level, $\beta_n^s << \beta_n^R$ and $\beta_p^s \approx \beta_p^R$ are the common situations. Here, R and S stand for the sensitizing center and recombination center respectively. So, based on this model, the major characteristics of photoconductivity (imperfection, sensitizing, supralinear photoconductivity, negative photoconductivity, thermal and optical quenching of photoconductivity) can be explained [68]. Here, the optical quenching and negative photoconductivity are two interesting behavior of materials under irradiation explained below by two center model.

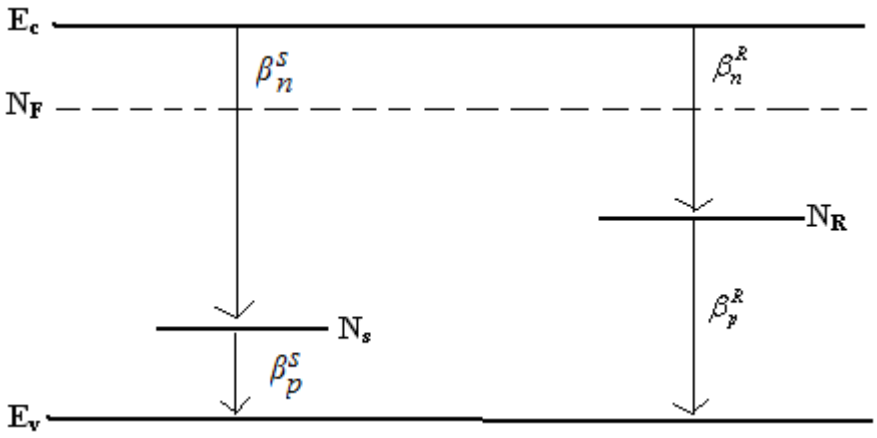

Figure 2.15: Two center model.

The process of decrease in photocurrent on illumination of a sample by light is called *photoquenching*. This process is closely related to the filling of the existing

defect states in the forbidden band gap region. The model to explain photoquenching is depicted in Fig. 2.16 [67].

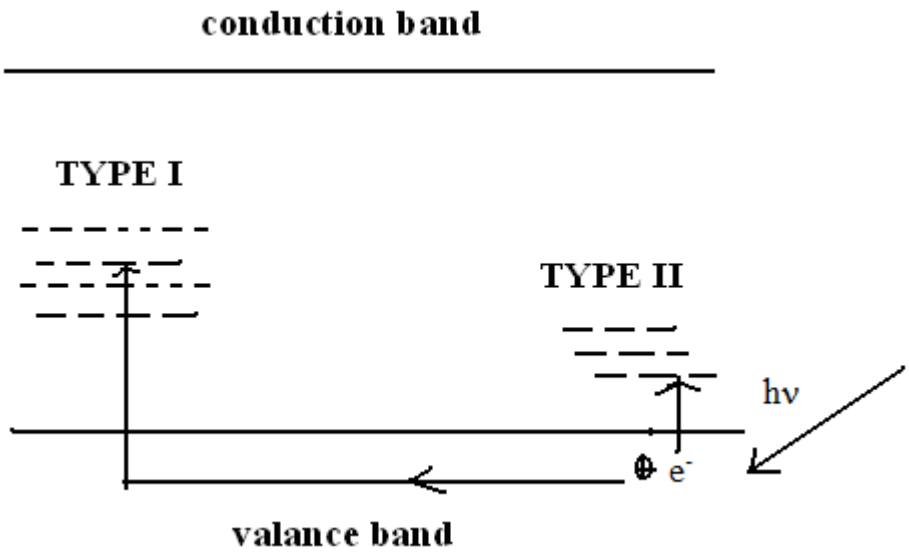

Figure 2.16: Energy scheme to explain photoquenching process

In this model, there are two active centers called as type I and type II represent the state close to the conduction band with high capture cross section for holes and state near the center of band gap with higher capture cross section for electrons, respectively. On illumination, electrons are excited from the valance band to type II levels by leaving free holes behind. Then, the created holes in valance band on radiation are captured by type I levels due to their high capture cross section for holes. Consequently, there is no contribution of created both electrons and holes to conduction process [67].

Negative photoconductivity is another interesting behavior exhibited by some materials explained by two center model. In this process, a decrease in current is observed instead of the expected increase when the sample is irradiated. This model is also based on two levels with energies of E_1 and E_2 located between the Fermi level and conduction band, and between the Fermi level and valance band, respectively. The assumption in this model is that the first type of centers has a quite high capture cross section for electrons and the probability of excitation of electrons to conduction band is very low. For the second type of centers, there is a high capture

cross section for both electrons and holes and thus results in attracting electrons from the conduction band and holes from the valance band and subsequently recombine them. As a result of this process, the net number of the free carriers contributing to conduction process is reduced owing to the incident radiation [67].

CHAPTER 3

EXPERIMENTAL TECHNIQUES

3.1 Introduction

In this chapter, the details of deposition of $AgGa(Se_{2-x}S_x)$ thin films, electrical, optical and structural characterization measurements and analysis of experimental results are presented. The main objective of this chapter is to provide the basic information about the deposition process of thin films and description of experiment setups used for the investigation of structural, electrical, and optical properties of the deposited thin films.

The sections in this chapter are organized as follows. Firstly, the deposition process of thin films by using thermal evaporation, electron beam, and sputtering techniques are introduced. This is followed by a brief introduction of basic structural, electrical, and optical characterization systems and measurement steps.

3.2 Deposition of Thin Films

3.2.1 Substrate Preparation

The deposition of $AgGa(Se_{0.5}S_{0.5})_2$, $AgGaSe_2$, and $AgGaS_2$ thin films was carried out by using thermal evaporation, electron beam, and sputtering techniques. Soda-lime glass and quartz materials were used as substrates in deposition of thin films. It is known that soda-lime glass material is available in large quantities at low cost and satisfy many physical properties (sufficient mechanical support, convenient thermal expansion coefficient for good match to I-III-VI_2 compounds, sufficient surface smoothness, thermal endurance up to 550 ^oC without softening so much, and

satisfying a good insulating) [70]. However, in this study, to achieve the preparation of mono-phase $AgGaS_2$ thin films a higher annealing temperature (>550 ^oC) was required and thus quartz material had to be used instead of soda-lime glass as a substrate. The size of the substrates was 25 mm x 25 mm in square form for the sake of the ensuring conformity with the dimension of sample stage mounted in measuring system. Having obtained the substrates with desired forms, the cleaning process was employed since the clearness of the substrate has an important effect on deposition of high quality thin films. As each material requires different cleaning process, the cleaning of soda lime glass substrates was carried out by following several cleaning stages special to this material to remove the contaminations on the surface onto which the film will be deposited. The main cleaning stages can be summarized as follow: firstly, to eliminate protein and oil molecules substrates were kept in a chemical detergent solution diluted with distilled water; then, substrates in same solution were kept at temperature of about 100 ^oC in an ultrasonic bath for 10 minute to ease the realising of solved contaminations. Secondly, the substrates were rinsed with hot distilled water to remove the possible left detergent contaminations remained from the previous cleaning stage. Then, in order to remove organic contaminants substrates were immersed in a boiling diluted H_2O_2 solution nearly for 15 minute and subsequently the same solution were put into ultrasonic cleaner for the same period of time. Finally, substrates extracted from this solution were rinsed with hot distilled water and kept in pure methanol to keep ready for use. And, before placing them into the holder for the deposition process, the substrates taken from the methanol were dried by blowing pressurized N_2 gas.

3.2.2 Growth of $AgGa(Se_{0.5}S_{0.5})_2$ Thin Films by Thermal Evaporation Method

The deposition of $AgGa(Se_{0.5}S_{0.5})_2$ thin films was carried out by using a Leybold Univex 300 thermal evaporation system. The system basically consists of a turbo-molecular pump, a bell jar vacuum chamber, substrate holder equipped with heating elements, source crucible with embedded thermocouple and heating

elements, a quartz crystal thickness monitor, mechanically controllable shutter placed between source and target, and other accessory parts shown in Fig. 3.1 [71].

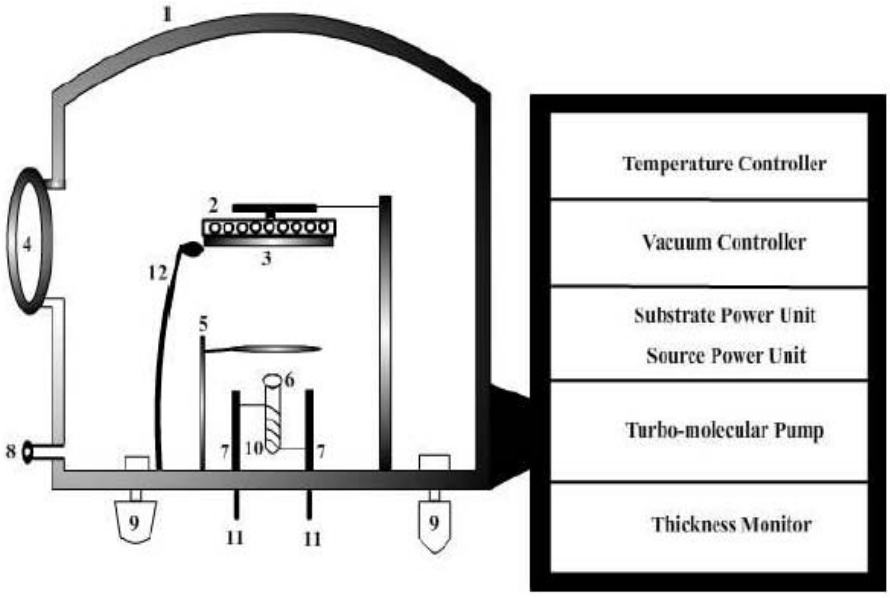

Figure 3.1: Schematic illustration of thermal evaporation system employed for the deposition of $AgGa(Se_{0.5}S_{0.5})_2$ thin films: 1. bell-jar, 2. substrate heater, 3. substrate holder, 4. window, 5. shutter, 6. source boat, 7. feed through, 8. air valve, 9. vacuum gauges, 10. source heater, 11. filament current wires, and 12. thickness monitor probe.

In the bottom flange of the vacuum evaporation system many holes are available to mount gauges, current and mechanical feedthroughs, shields and pumping pipes.

The lowest reachable pressure in this system is around 10^{-6} Torr. The vacuum level of system is monitored through the pirani and penning vacuum gauges as depicted in Fig. 3.1. The evaporation of source to be deposited is carried out by using a tungsten wire wound quartz crucible heated by passing an electrical current through it. The temperature of source is controlled by the power unit supplying and manipulating current going through the wire. The temperature of both substrate holder and source boat were monitored by a Pt/Pt-13 % Rh thermo couple placed inside the quartz ampoule and a thermocouple embedded to the surface of substrate holder, which is controlled by an Elimko-400 temperature controller.

The substrate holder is mounted above the source with design of allowing manipulating the distance between the source and substrate to arrange the position of holder with respect to source boats. The temperature of the substrate was measured with a copper-constantan thermocouple having a contact with surface of substrate holder. System is equipped with a manual controllable shutter to designate the starting and ending time of the deposition cycle. In addition, the thickness and deposition rate of films are monitored in-situ by an Inficon XTM/2 quartz crystal monitor.

$AgGa(Se_{0.5}S_{0.5})_2$ thin films were deposited on soda-lime glass substrates by evaporation of crystal powder crunched in fine grains . To obtain the sintered polycrystalline $AgGa(Se_{0.5}S_{0.5})_2$ powder, the stoichiometric quantities of high purity Ag, Ga, Se, and S have been placed into a chemically cleaned quartz crucibles and subsequently it was evacuated by connecting to vacuum system with base pressure of around 10^{-5} Torr and sealed off. In order to perform the sintering process, the crucible was placed into a Lindberg one zone horizontal furnace, heated slowly up to 1000 ^{o}C, and kept at this temperature approximately 12 h to complete the reaction between the loaded constituent elements. After obtaining the sintered crystal powder, $AgGa(Se_{0.5}S_{0.5})_2$ thin films have been deposited using it as a evaporation source by thermal evaporation system with base pressure of 10^{-6} Torr. The substrate temperature during deposition was kept at around 120 ^{o}C and thickness of the samples controlled and monitored in-situ by thickness monitor. The deposition rate during evaporation cycle was kept constant at value around 8 Å/sec. The thickness of the samples were also measured by using Dektak 6M profilometer following to the deposition and found to be around 1 μm. Post annealing process is an important technique widely used to change the physical and chemical properties of deposited films. To investigate the effect of post-annealing on structural, electrical, and optical properties of $AgGa(Se_{0.5}S_{0.5})_2$ thin films, they were annealed in the temperature range of 300-600 ^{o}C for 30 min under the Ar gas flow in the furnace.

3.2.3 Growth of $AgGaSe_2$ Thin Films by Electron Beam Technique

Electron beam (e-beam) technique offers significant advantages over the other PVD techniques in terms of stoichiometry, directionality of the evaporant flux and purity of the grown thin films. This technique is particularly convenient for the evaporation of alloys and compounds containing constituent elements having quite different vapour pressures since the high thermal density employed by this technique prevailing over small region of the source to be deposited and ensure complete evaporation of material without preference of the vapour pressures of the including elements [72]. In addition, in terms of material utilization efficiency this technique possesses a considerable advantage over the other PVD methods. Moreover, e-beam technique offers good structural and morphological control of the films, high deposition rates, low contamination and easy control of composition and uniformity of the deposited films.

$AgGaSe_2$ thin films were prepared using the e-beam system in Thin Film Laboratory of Middle East Technical University as depicted in Fig. 3.2 [73]. As shown in Fig. 3.2, e-beam system basically consists of the following main components: electron beam source (with a 3-kW electron gun, water cooled holder stage for the graphite crucible containing source material, and electromagnet for the control the direction of generated e-beam), stainless steel vacuum chamber (50 cm in diameter and 75 cm in length), substrate holder equipped with heating unit, turbomolecular pump, thickness monitor unit, vacuum gauges, a shutter between source and substrate holder, and a thermocouple embedded to substrate holder to measure the temperature during the deposition cycle. In this system, the deposition chamber can be evacuated to a pressure of around 10^{-7} Torr. The generated e-beam by electron-beam source is accelerated to high energies and directed to graphite crucible containing evaporation source in powder form composed of fine grain of $AgGaSe_2$ compound and subsequently electron energy is transformed into heat energy and results in evaporation of material. The source powder of $AgGaSe_2$ single crystal have been synthesized by preparing stoichiometric mixture of constituent elements of pure In, Ga, and Se (99.9999 %) sealed into the an evacuated quartz ampoule (10^{-6} Torr).

The sealed ampoule was placed in a horizontal furnace kept at a temperature of 1050 ^{o}C for 48 hours and subsequently was slowly cooled down to the room temperature. Following to the sintering process, a crystalox MSD-4000 model three zone vertical Bridgman-Stochbarger system (shown in Fig. 3.3) was used for obtaining single crystalline form of $AgGaSe_2$ compound.

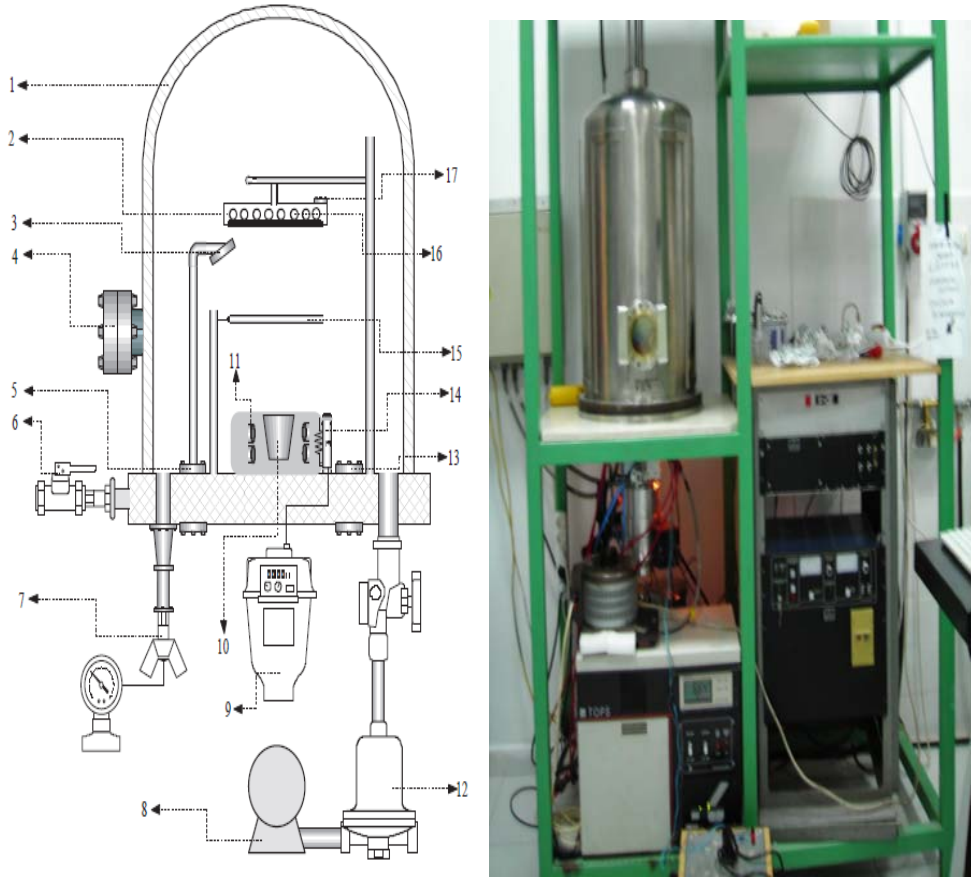

Figure 3.2: Schematic representation of electron beam evaporation system used for the deposition of $AgGaSe_2$ thin films: 1. bell-jar, 2. substrate holder, 3. thickness monitor probe, 4. window, 5. feedthrough, 6. air valve, 7. vacuum gauges, 8. rotary pump, 9. e-beam deflection unit, 10. graphite crucible, 11. water cooling system, 12. turbomolecular pump, 13. feedthrough, 14. e-gun, 15. shutter, 16. substrate heater, and 17. thermocouple.

Figure 3.3: A crystalox three zone vertical Bridgman-Stockbarger system used for the growth of $AgGaSe_2$ single crystal.

For that, a special temperature profile was applied. The temperature of top, middle and bottom zones of the furnace were set to 1050, 850, and 600 ^{o}C, respectively. Following to a 105 hours translation of crucible from the top to cold zone with translation rate of 1.00 mm/h, the single crystalline $AgGaSe_2$ has been grown successfully. After the extraction of powder from the grown crystal ingot, it was used as an evaporation source. Then, the deposition of $AgGaSe_2$ thin films has been carried out on to the soda-lime glass substrates by e-beam evaporation system introduced previously with a base vacuum maintained at about 10^{-6} Torr. The substrate holder was placed at approximately 15 cm above the graphite crucible including the bulk $AgGaSe_2$. The substrate holder was heated up to 200 ^{o}C and maintained at this temperature during the full cycle of evaporation process. The deposition rate (varied between 8 to 15 Å/sec) and thickness of grown films were monitored simultaneously by means of integrated Inficon XTM/2 thickness monitor. The thickness of the films was also confirmed by measuring with a Dektak 6M

profilometer and found to be in the range of 1.8-2 μm depending on the position of samples in holder during deposition process. Having deposited $AgGaSe_2$ films, they were subsequently annealed for 30 min in the temperature range of 300-600 ^oC under the constant nitrogen gas flow in furnace shown in Fig. 3.3.

3.2.4 Growth of $AgGaSe_2$ Thin Films by Sputtering Technique

In this thesis, $AgGaSe_2$ thin films were also prepared by using sputtering PVD technique. Sputtering technique is mostly used for both thin film deposition and etching process. It is preferred particularly in semiconductor industry for the integrated circuit processing and deposition of contacts to thin film transistors.

In this study, $AgGaSe_2$ thin films were prepared by using a Vaksis three magnetron DC/RF sputtering system shown in Fig. 3.4 [71].

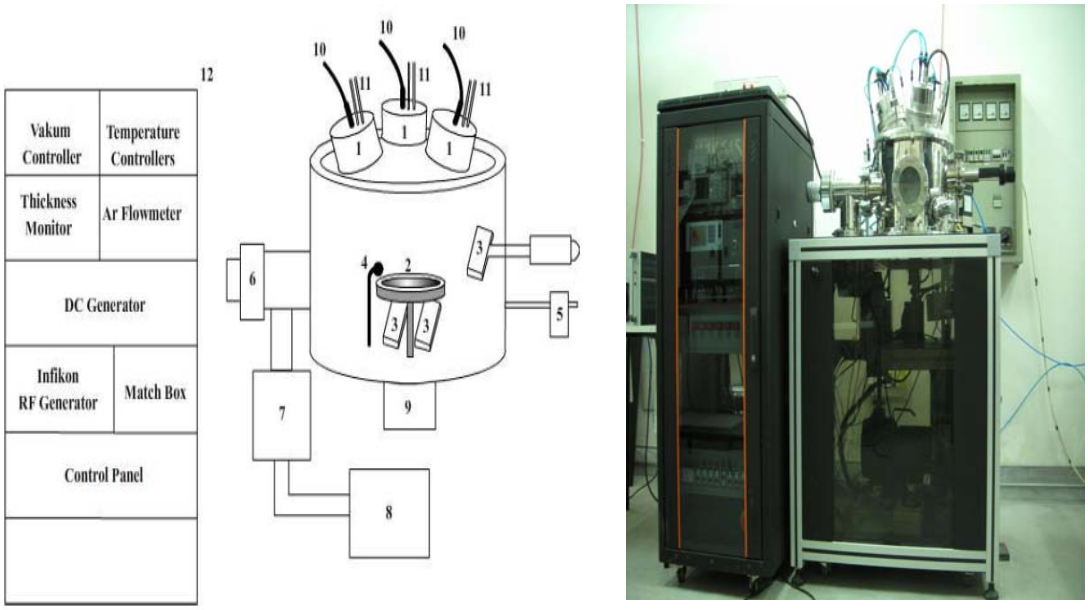

Figure 3.4: Sputtering system used for the deposition of $AgGaSe_2$ thin films: 1. magnetron heads, 2. substrate stage, 3. heating elements (halogen lamps), 4. thickness measuring crystal, 5. Ar gas flow control unit, 6. vacuum valves, 7. turbomolecular pump, 8. roughing pump, 9. substrate holder rotating arrangement, 10. RF/DC magnetron conections, 11. water cooling system, 12. system control unit.

As can be seen from the Fig. 3.4, system consists of one RF and two DC magnetron heads cooled by water circulation, vacuum chamber, substrate holder,

heating elements of substrate holder (attainable temperature up to 600 ^{o}C), RF generator (Fokus 600 W) with a Dressler VM100A match box for the generation of RF plasma, an Advanced Energy MDX500 power supply for the DC plasma generation, vacuum gauges, a shutter, rough and turbomolecular pump, and other required accessory components.

$AgGaSe_2$ thin films were deposited using Ag and GaSe targets through the DC/RF magnetron sputtering. RF power applied for the deposition of GaSe layers was 75 W with deposition rate of 2.5 Å/s, while Ag thin film layers were deposited by 20 W DC magnetron sputtering with rate of 0.5 Å/s in $5x10^{-3}$ Torr Ar atmosphere. The chamber pressure was lowered to around 10^{-7} Torr and subsequently kept at around $5x10^{-3}$ Torr after the introducing Ar gas for generation of plasma during deposition cycle for both Ag and GaSe thin film layer. Before the deposition process, the target surfaces were treated with pre-sputtering for 3 min to eliminate the potential contaminations introduced during the exposure to atmosphere or target installation stage. The layer thickness optimization of Ag and GaSe was carried out by conducting several deposition cycles with the same deposition parameters prior to the sequential deposition of GaSe/Ag/GaSe/Ag/GaSe/Ag/GaSe/Ag/GaSe thin film layers on to the soda-lime glass substrates to form $AgGaSe_2$ thin film. During the sputtering, substrate temperature was kept at a temperature around 250 ^{o}C. Thickness of individual layers of Ag and GaSe was monitored in-situ by thickness monitor and was around 15 and 130 nm, respectively. Measurement conducted by Dektak profilometer has revealed that the thickness of deposited thin films was varying from 705 to 720 nm depending on position of samples on substrate holder. The post-annealing following to the deposition of samples was carried out in the temperature range of 350-600 ^{o}C for 5 min under the N_2 gas flow.

3.2.5 Growth of Ag-Ga-S Thin Films by Thermal Evaporation Method

Ag-Ga-S (AGS) thin films were prepared by using the thermal evaporation system introduced previously. Samples were produced on to the soda-lime glass substrates in vacuum of around 10^{-6} Torr by using double sources. Following to the standard procedure of cleaning, substrates were placed in holder with convenient

masks kept directly at approximately 15 cm above the quartz crucibles including Ag and $AgGaS_2$ powder. The substrate temperature was kept constant at around 200 ^oC during the deposition cycle. Quartz crucibles containing evaporation sources heated by tungsten wire coil were used for the evaporation of Ag and $AgGaS_2$ precursors. The powder of $AgGaS_2$ was obtained by crushing the sintered ingot into the fine grains. The polycrystalline bulk $AgGaS_2$ was synthesized by direct reaction of pure (99.9999 %) constituent elements Ag, Ga, and S weighted in correct stoichiometric ratio in evacuated quartz crucible (10^{-6} Torr) in a horizontal one zone furnace. The temperature of furnace was elevated from the room temperature to 600 ^oC at a rate of 100 ^oC/h, while it was 50 ^oC/h from the 600 to 1050 ^oC. To ensure the homogeneity of the melt and complete the reaction between the constituent elements crucible was held at 1050 ^oC for 4 days. Following to this process, the melt was cooled down to room temperature at a very low cooling rate. Prior to the sequential evaporation of Ag and $AgGaS_2$ layers, the optimization of individual layers was carried out independently by repeating several deposition cycles with the same deposition parameters. The energy dispersive X-ray analysis (EDXA) carried out for the deposited $AgGaS_2$ layers has revealed that there was almost no silver (around 1%) in composition, and a Ga and S rich composition with atomic percent ratio of 5:8. The most probable cause of the shortage of the Ag in composition is the decomposition of the starting material during evaporation process and quite difference between the vapour pressures of constituent elements. To compensate the deficiency of Ag in composition of deposited films, it was incorporated independently from a second source including only Ag shots. The optimization of Ag layers was also carried out till the re-producibility of samples was achieved. The crucible containing powder $AgGaS_2$ was heated up to 1000 ^oC, while the crucible including Ag was heated till a temperature that melts the silver (960 ^oC). To form the AGS thin films, the individual layers of $AgGaS_2$ and Ag were sequentially deposited on soda-lime glass substrates in sequence of $AgGaS_2$/Ag/$AgGaS_2$ with thickness of approximately 900/55/900 nm, respectively. As it was done in deposition of other compounds, the thickness and deposition rate of individual layers were controlled and manipulated in-situ by thickness monitor. Thin films of AGS were annealed in the temperature range of

350-550 ^{o}C for a period of 5 min in N_2 flow atmosphere to study the effect of post-annealing on properties of thin films.

In addition, $AgGaS_2$ mono-phase thin films were prepared by the same procedure employed for the deposition of AGS thin films. In this case, the individual precursors of $AgGaS_2$ and Ag were deposited sequentially on both soda-lime and quartz substrates in the order of $AgGaS_2$/Ag/$AgGaS_2$ thin film layers with thickness of 300/100/300 nm, respectively. Having obtained $AgGaS_2$ thin films, they were annealed in the temperature range of 450-700 ^{o}C for 5 min in N_2 gas flow to examine the changes with post-annealing process.

3.3 Structural, Compositional and Surface Characterization

3.3.1 X-ray Diffraction (XRD)

As it is introduced in theoretical consideration part, X-ray diffraction technique has been developed for the calculation of the structural parameters, determination of phases and the orientation of a single crystal or grain, measuring the residual stress and estimation of grain sizes.

In this study, to investigate the structural properties of deposited $AgGa(Se_{2-x}S_x)$ thin films a Rigaku Miniflex XRD system equipped with CuK_α X-ray source (λ=1.504 Å) was used. XRD patterns were recorded in the range of 10-90^{o} with a scan speed of 2^{o}/min for all deposited thin films. Once the XRD diffractograms obtained, they were compared with database including XRD patterns of well-known material (nearly 62.000 different diffraction patterns) structures supplied by JCPDS (Joint Committee on Powder Diffraction Standards) cards and detailed knowledge about the structure, phase composition and degree of crystallinity is obtained. JCPDS is an organization that supply a database consists of XRD spectra of organic and inorganic materials. It is supplied generally by manufacturer of diffraction systems and offered in two different versions, which are PDF I and PDF II. The PDF I serves the information about the d-spacing, chemical formula and relative peak intensities, while PDF II supply full information about the particular phases covering structural parameters as well. Based on the analysis of XRD patterns, valuable knowledge about the structure of $AgGa(Se_{2-x}S_x)$ thin films was obtained. And, with the help of

measured full width at half maximum (FWHM) of preferred orientation, the grain sizes were calculated through the Shrerrer's formula.

3.3.2 Scanning Electron Microscope (SEM) and Energy Dispersive X-ray Analysis (EDXA) Measurements

As it is introduced in theoretical consideration part, energy dispersive X-ray analysis (EDXA) is a powerful technique to determine the chemical composition of materials on the micro and nano-scale. In this technique, with aid of identification of emitted X-rays from the interaction of bombarded electrons and the investigated material, the amount and spatial distribution of elements ranging from the Boron to Uranium can be measured. EDXA is mostly used as an accessory component of scanning electron microscopy (SEM) system. EDXA equipped SEM can provide valuable information about the quantitative elemental analysis, sample surface morphology, and many other properties.

Following to the deposition, the surface morphology and composition of $AgGa(Se_{2-x}S_x)$ thin films were investigated by using a FEI Quanta 400 FEG model SEM equipped with EDXA system in Central Laboratory of Middle East Technical University. The measurements were conducted at different acceleration energies ranging from the 6 kV to 30 kV depending on the aim of study.

3.3.3 X-ray photoelectron Spectroscopy (XPS) Measurements

A detailed knowledge about the surface composition, the identification of surface or near surface chemical state of elements (chemical bonding states) and detection of contaminants are provided by conduction of X-ray photoelectron spectroscopy (XPS) measurement. An XPS system basically consists of a high vacuum chamber, a lens system collecting the photogenerated electrons, an X-ray source (usually MgK_α (1253.6 eV)), a spectrometer including electron energy

analyser and detector, and a displaying system to show the signal versus kinetic or binding energy spectra.

XPS measurements for the deposited $AgGa(Se_{2-x}S_x)$ thin films were carried out by using a UNISPECS ESCA system in Central Laboratory of Middle East Technical University as shown in Fig. 3.5. The XPS data was obtained by using monochromatic MgK_α line at a power of 195 Watt in conjunction with concentric hemispherical electron analyser operated in 48 eV pass energy. The measurements were performed in vacuum with base pressure of around 10^{-7} Pa. Survey scan was carried out from 1100 eV to 0 eV with step size of 1 eV and an approximately 100 ms dwell time. Once XPS survey spectra obtained, after following to complex and long time taking fitting analysis stages (background elimination, designing convenient fitted functions, preservation of right intensity ratio of spin-orbit doublets for p, d, and f photoelectron lines, and calibration of binding energies) detailed information about the composition and bonding nature of constituent elements present at surface/near surface of $AgGa(Se_{2-x}S_x)$ thin films have been obtained.

Figure 3.5: XPS system in Central Laboratory of Middle East Technical University.

3.4 Electrical Characterization

3.4.1 Introduction

In this study, under the electrical characterization part the temperature dependence of resistivity (ρ), mobility (μ) and carrier concentration of deposited $AgGa(Se_{2-x}S_x)$ thin films were investigated.

For the electrical measurements, several types of sample geometries can be used.

However, Hall bar and van der Pauw geometries (Fig. 3.6) are the most commonly preferred ones [74]. Each geometry has its own advantages and disadvantages. The Hall bar geometry is a good choice particularly for resistivity measurement and widely used for measuring magnetoresistance or Hall mobility of sample with low resistance [74]. Disadvantages of the Hall bar geometry can be summarized as follow: for the mobility measurement at least four contacts are needed, geometry of the sample has a significant influence on accuracy of measured resistivity, and there is a difficulty in measuring Hall bar width and distance between the side contacts. The van der Pauw geometry can solve large part of problems encountered in Hall geometry. Provided that the following conditions are satisfied

- The contacts are placed on the circumference of the sample
- Contacts are sufficiently small
- A uniform sample in terms of thickness
- Samples without isolated regions (continuity of sample)

it is possible to calculate the resistivity, mobility, and carrier concentration of any arbitrary shaped sample by van der Pauw geometry. The main advantages over the Hall bar are the requiring of only four contacts, no need for measuring width or distance between contacts, and possibility of using simple geometries. On the other hand, there are also some disadvantages such as long time taking measurements and quite large errors stemming from contact size and position for simple geometries [74].

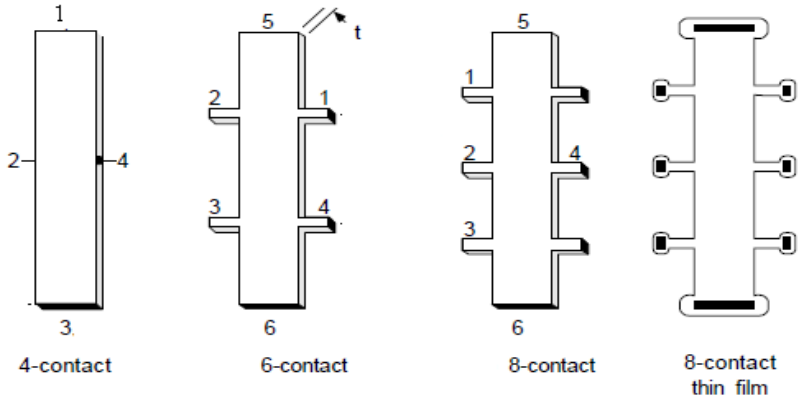

(a)

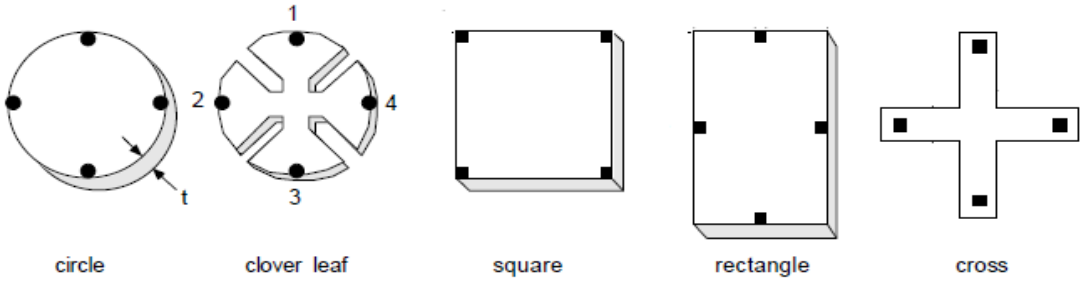

(b)

Figure 3.6: Common (a) Hall bar and (b) van der Pauw geometries used for the electrical measurements.

In this thesis, to study the temperature dependence electrical measurements of deposited thin films, samples were prepared in van der Pauw geometry as shown in Fig. 3.7. Ohmic contacts to carry out electrical measurements were made by evaporation of In through the shadow contact mask by using the metallic evaporation system [66]. Following to the In evaporation, samples were heated at 100 ^{o}C for 30 min to ensure a good adherence of In to sample through the diffusion to bulk and subsequently the copper electrodes were attached to the contacts by silver paste. In electrical measurement, it is very crucial to ensure the ohmic contact behaviour. Thus, samples were checked in terms of ohmicity by applying I-V measurements and it was found that I-V characteristic is independent of applied bias polarity that confirms the ohmic nature of a contact.

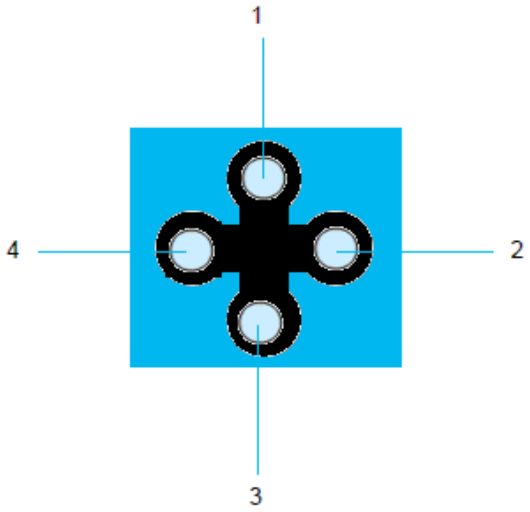

Figure 3.7: van der Pauw mask geometry used during thin film production for electrical characterization measurements.

3.4.2 Resistivity Measurement

The sample geometry used for the resistivity and Hall measurement is shown in Fig. 3.11. These measurements were carried out in the temperature range of 100-430 K under vacuum in a closed cycle cryostat equipped with magnet system shown in Fig. 3.8 [75]. The current was supplied by using a Keithley 220 programmable current source enable to supply current in the range of 0.1 nA to 100 mA with a compliance voltage up to 100 V. For the measuring voltage drop across the contacts, a Keithley 619 Electrometer was used.

The resistivity measurement was carried out by applying a constant current through a couple of contacts and subsequently reading voltage drop across the other two contacts. That is, firstly, the constant current I_{12} (I) applied through the contacts 1 and 2 and voltage drop across contacts 3 and 4 is measured ($V_{12,34}$). Similarly, voltage drops of ($V_{23,41}$), ($V_{34,12}$), ($V_{41,23}$) are measured and recorded. Then, the resistance of $R_a=(V_{12,34})/I$, $R_b=(V_{23,41})/I$, $R_c=(V_{34,12})/I$, and $R_d=(V_{41,23})/I$ were evaluated. Once the R_a, R_b, R_c, R_d and thickness of the sample known, the resistivity is calculated through the following relation:

$$\rho = \frac{\pi t}{Ln(2)} \frac{(R_1 + R_2)}{2} f\left(\frac{R_1}{R_2}\right) \tag{3.1}$$

where $R_1 = R_a + R_b$, $R_2 = R_c + R_d$, t is the thickness of the sample, and f is a correction factor or van der pauw function, which is a function of the potential difference measured. If the two resistances of (R_1 and R_2) agree within around ±10 the $f(R_1/R_2)$ is taken to be 1 [62]. That is, f is a parameter based on sample symmetry and is related to the resistance ratio of R_1 and R_2.

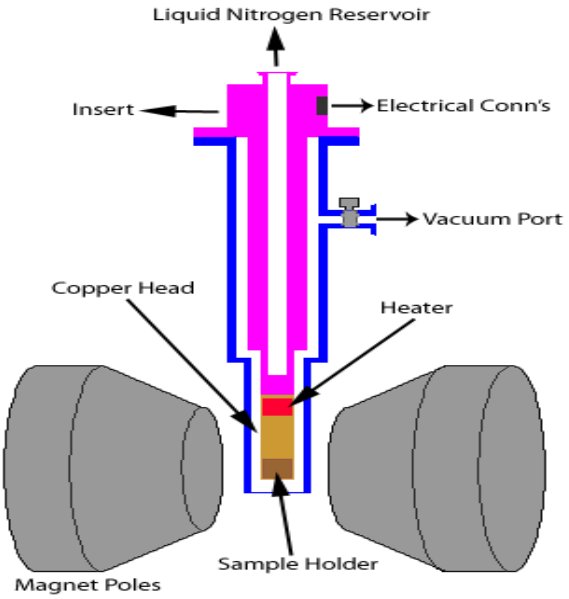

Figure 3.8: Schematic representation of the cryostat and magnet system.

3.4.3 Hall Measurement

System used for the Hall measurement is depicted in Fig. 3.8. The Hall measurement was performed on samples with geometry shown in Fig. 3.7. The measurement was carried out by a series of reading with the consideration of different combination of the magnetic field, current and voltages. Firstly, a constant current was applied between the contacts 2 and 4 in the absence of magnetic field and subsequently measuring the potential drop across 1 and 3, and $R_x=(V_3-V_1)/I$ is calculated. Secondly, the current was applied between same contacts in the presence

of magnetic field and potential drop is recorded and $R_x^{'}$= (V_3-V_1)/I is evaluated. In the third step, the current was supplied through the contacts 1 and 3 in the absence of magnetic field, and voltage drop across the 2 and 4 contacts is measured and R_y=(V_2-V_4)/I is found. And, finally, with the same contact variations in the magnetic field $R_y^{'}$= (V_2-V_4)/I is calculated. Once recording these readings, ΔR_x = (R_x – $R_x^{'}$) and ΔR_y = (R_y – $R_y^{'}$) values were calculated. By making use of these values, the Hall coefficient is found through the following relation:

$$R_H = \frac{t}{B}\frac{\left(\Delta R_x + \Delta R_y\right)}{2} f \tag{3.2}$$

where t and B are the thickness of the sample and applied magnetic field. During the Hall measurement, the strength of magnetic field was around 1 T. After obtaining Hall coefficient, the carrier concentration can be calculated as follow:

$$\text{n or p} = r/qR_H \tag{3.3}$$

The sign of Hall coefficient determines the type of conduction of sample (n or p type). Finally, by combination of calculated conductivity (σ) and Hall coefficient, the mobility (μ) can be evaluated as follow:

$$\mu=\sigma R_H \tag{3.4}$$

3.5 Photo-Electrical Measurement

3.5.1 Photoconductivity

Photoconductivity (PC) measurement provides valuable information about the nature of recombination process and distribution of the trap levels within the band gap zone. In this study, to perform PC measurement a Janis cryostat equipped with liquid nitrogen cooling system was used. In the photoconductivity measurement

setup, the illumination of samples was provided by a 12 Wat halogen lamp with relatively long wavelength range, which is placed approximately 0.5 cm above the sample to ensure a homogenous illumination of sample under estimation. PC measurement was carried out under different illumination intensities (between 17-115 mW/cm^2) adjusted by changing the value of current passing through the lamp (between 50-90 mA with 10 mA steps). The current through the lamp was supplied by a Keithley 220 programmable current source. The generated illumination was measured by an IL Ford 1700 radiometer. The bias voltage and current across the contacts were measured by a Keithley 2400 sourcemeter. All component of PC setup was controlled by LabView computer program. PC measurement was performed in the temperature range of 100-430 K with 10K increment arranged by a Lake Shore 331 temperature controller.

The analysis of light dependence of photocurrent have revealed important knowledge about the statistical distribution of trap levels, type of recombination centres, and photoconduction character of deposited AgGa($Se_{2-x}S_x$) thin films.

3.5.2 Photoresponse Measurement

Photoresponse measurement was carried out to determine the sensitivity of deposited thin films to the exposed light spectrum consisted of different wavelength, estimation of optic band gap, energy levels located in the forbidden band gap, and detect crystal-field and spin orbit split levels special to chalcopyrite materials.

The experimental setup for the Photoresponse measurement is illustrated in Fig. 3.9 [71]. The system consists of a Newport Oriel 74125 monochromator (with 3 diffracting gratings of 600 lines/mm, offering 25-1300 nm, 600-2500 nm, and 900-2500 wavelength ranges), a Newport Oriel Apex monochromator illuminator with a halogen lamp (power spectrum is shown in Fig. 3.10) and 4 optical filter, a Keithley 2440 sourcemeter to apply bias voltage and measure the generated current, a shutter placed between the lamp and monochromator, and computer with installed LabView program to control system.

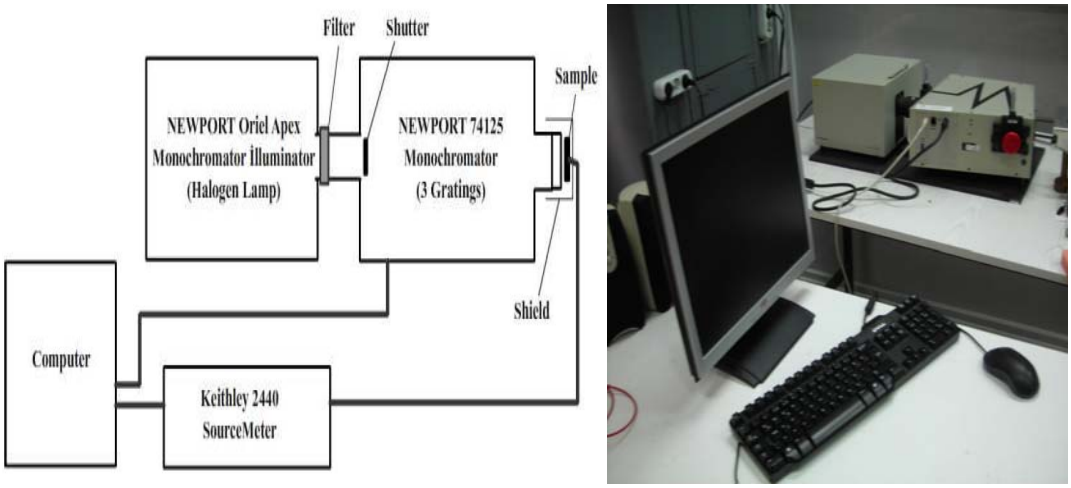

Figure 3.9: Photoresponse measurement setup.

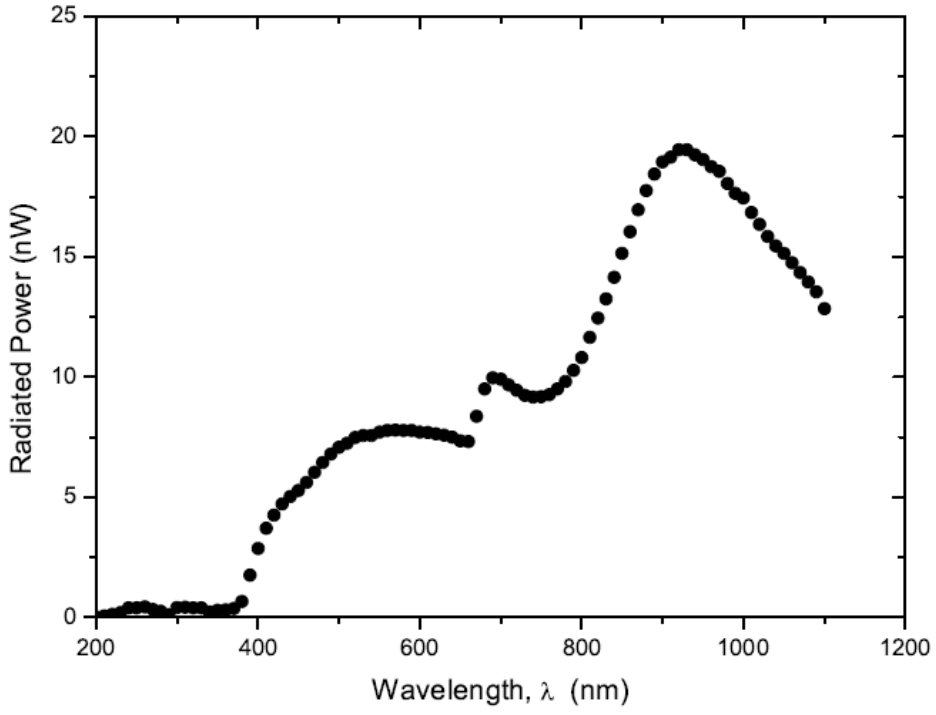

Figure 3.10: The halogen lamp power spectrum

Photoresponse measurements were carried out in the spectral wavelength range of 300-1100 nm with steps of 5 nm at room temperature for all samples.

3.6 Transmission and Reflection Measurement

Transmission and reflection measurements are the basic characterization tools to study the optical properties of semiconductors. Analysing spectra obtained from these spectra, it is possible to calculate optical absorption coefficient, optical band gap, and optical constants such as extinction coefficient and refractive index.

A spectrophotometer is an optic system enables to measure the transmission and reflection. It basically consists of a light source, a monochromator to select wavelengths, a holder to keep sample upright to irradiated light beam, and detector to measure the transmitted or reflected light. In this study, transmission and reflection measurements were conducted using a Pharmacia LKB Ultraspec III UV-VIS and Shimadzu UV-1201 spectrophotometers for the 325-900 nm and 300-1100 nm wavelength ranges, respectively. Measurements for $AgGa(Se_{2-x}S_x)$ thin films have been conducted either in the 325-900 nm or 300-1100 nm range depending on the optical properties of sample. Following to analysing obtained data, the optical band gap, absorption coefficient, and the nature of the band gap (direct or indirect) of deposited $AgGa(Se_{2-x}S_x)$ thin films were determined.

CHAPTER 4

RESULTS AND DISCUSSIONS

4.1 Introduction

This chapter covers the results of electrical, structural and optical measurements obtained for the $AgGa(Se_{2-x}S_x)$ thin films ($0 \leq x \leq 2$) deposited by thermal evaporation, electron-beam and sputtering techniques. Chapter is divided into three parts. First part deals with the characterization of $AgGa(S_{0.5}S_{0.5})_2$ thin films deposited by thermal evaporation method; second part presents the investigation of structural, electrical, and optical properties of $AgGaSe_2$ thin films deposited by both electron-beam method and sputtering technique; and finally third part addresses the optimization process for the deposition of Ag-Ga-S thin films by thermal evaporation method to obtain the mono-phase $AgGaS_2$ thin films and determine the physical properties by performing several type of electrical, optical and structural measurements.

4.2 Charecterization of $AgGa(Se_{0.5}S_{0.5})_2$ Thin Films Deposited by Thermal Evaporation Method

4.2.1 Introduction

The stoichiometric quantities of high purity Ag, Ga, Se, and S have been fused in a quartz crucible to carry out sintering $AgGa(Se_{0.5}S_{0.5})_2$ polycrystalline compound to be used as an evaporation source for the deposition of $AgGa(Se_{0.5}S_{0.5})_2$ thin films onto the soda-lime glass substrates by thermal evaporation method. The substrate temperature during deposition was kept at 120 ^oC and the thickness of the deposited films was around 1 μm. In order to determine the effect of heat treatment

on deposited films, they were annealed in the range of 300-600 ^{o}C for 30 minutes. It was followed by investigation of physical properties of deposited films by performing the X-ray diffraction, transmittance, scanning electron microscopy (SEM) equipped with energy dispersive X-ray analysis (EDXA), X-ray photoelectron spectroscopy, and temperature dependent conductivity measurements.

4.2.2 Structural, Compositional and Surface Analysis

In order to investigate the effect of heat treatment on the chemical compositions and stoichiometry, EDXA measurements were carried out for the source powder, as-grown and $AgGa(Se_{0.5}S_{0.5})_2$ thin film annealed in the temperature range of 450-600 ^{o}C . As can be seen from Table 4.7, there is a nearly stoichiometric composition for powder used as an evaporation source during preparation of samples, while it is not the case for as-grown and annealed-thin films.

Table 4.1: EDXA measurement results for $AgGa(Se_{0.5}S_{0.5})_2$ thin films.

Sample	Ag %	Ga %	Se %	S%
Powder	25.06	23.19	25.32	26.43
As-grown	5.58	27.76	13.84	52.82
450 ^{o}C	3.86	41.09	21.04	34.01
600 ^{o}C	3.63	36.73	21.24	38.40

The main drawback in thermal evaporation is the difficulty in ensuring a stoichiometric vapour phase to produce films with needed stoichiometry [13]. For compounds involving elements with different vapour pressures, it is quite hard to achieve a stoichiometric vapour phase. The EDXA results indicate that deposited as-grown films are silver- and selenium- deficient, gallium- and sulphur- rich. A systematic decrease in Ag is observed following to the annealing procedure.

Furthermore, fluctuations in Ga %, Se %, and S % compounds were observed following to the post annealing that was also understood from variation in colour of the films changed from yellow to dark gray. The yellow amorphous films are the clear evidence of that material contains a considerable excess of sulphur according to the Campe [13]. The plausible reason behind the decrease in S after post-annealing, resulting in transformation from amorphous to crystalline phase, is the triggering out-diffusion of sulphur since the excess sulphur in the amorphous phase is weakly bounded. So, the fluctuations with annealing in S, Se and Ga could be attributed to the segregation of these elements during the transformation of structure from amorphous to polycrystalline.

As it is clearly seen from XRD pattern of the evaporation source powder $AgGa(Se_{0.5}S_{0.5})_2$ in Fig.4.1, there are several mixed binary, ternary, and elemental crystalline structures. Upon searching in database cards, phases in structure were identified to be S (a_1,a_2, and a_3) , $AgGaS_2$ (b_1, b_2, and b_3), $AgGaSe_2$ (d_1 and d_2), Ga_2Se_3 (e), Ga_2S_3 (c_1 and c_2), and GaSe (f) with card no of JCPDS (joint committee on powder diffraction standards) 13-0141, 75-0114, 31-1240, 76-2310, 48-1433, and 81-1971, respectively. The observed sharp peaks in XRD patterns can be taken as indication of that the prepared powder is in crystalline form including mixture of several phases. Through these phases the sulphur is the dominant and directly related to incomplete reacting of constituent elements during the sintering process. Fig.4.2 shows the XRD patterns of powder, as-grown, annealed at 450, 500, 550, 600 ^oC $AgGa(Se_{0.5}S_{0.5})_2$ thin films in the same plot. As can be seen from the diffractograms there is a difference in the peak position of powder and deposited films that means different phases have developed in two structures. Namely, the phases included in powder are not transformed to the structure of deposited films. As-grown thin films have an amorphous structure and the transformation from the amorphous to the polycrystalline phase takes place at the annealing temperature of 450 ^oC. The transformation to polycrystalline in this temperature may be due to deposition of films at low substrate temperature (120 ^oC) since the impinging atoms will prefer placing at fixed positions and not allowing for the migration and nucleation during deposition cycle due to the insufficient thermal energy supplied by thermal energy. This behaviour was explained by Campe [13] like that films deposited at low

temperatures show that all thermally activated processes are taking place slowly, and resulting in low diffusion velocity, the re-evaporation rate, and the nucleation rate.

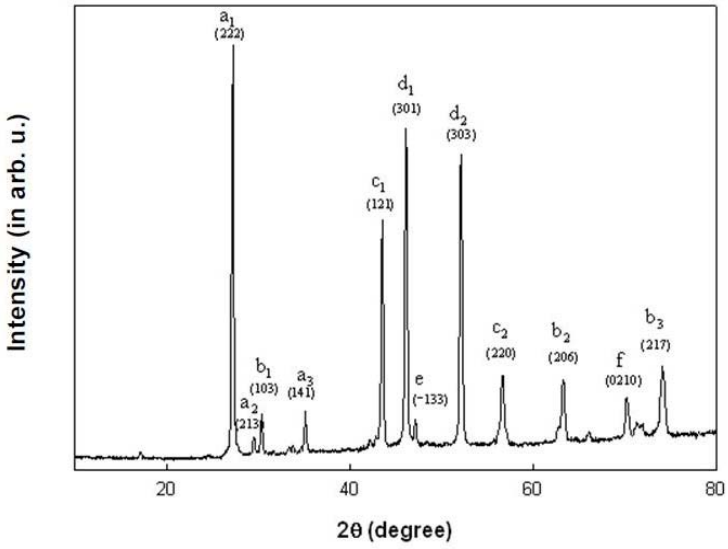

Figure 4.1: X-ray diffraction pattern for powder $AgGa(Se_{0.5}S_{0.5})_2$.

As seen from Fig.4.2, there is no variation in peak positions but an increase in intensity with increasing annealing temperature from 450 to 550 ^oC and a decrease over annealing at 600 ^oC.

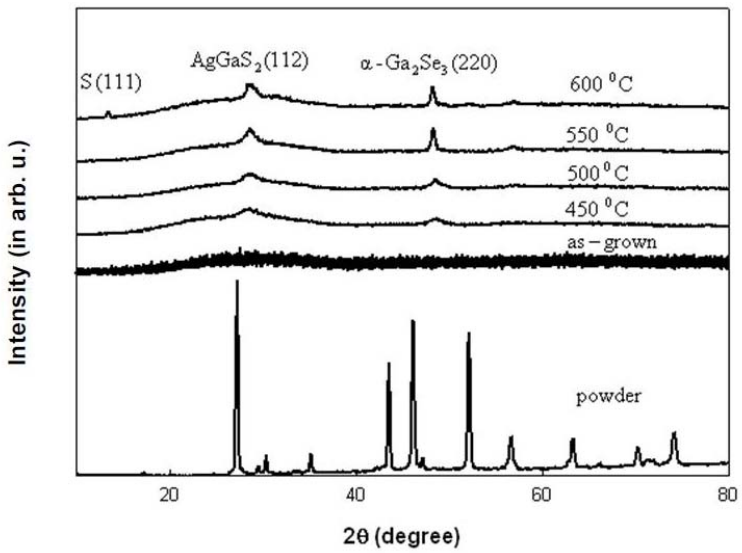

Figure 4.2: X-ray diffraction patterns of powder, as-grown, and $AgGa(Se_{0.5}S_{0.5})_2$ thin films annealed at 450, 500, 550, 600 ^oC.

On comparing with JCPDS cards and reported values [76], the main diffraction observed at 2θ ~28^{o} was identified to be belonging to the $AgGaS_2$ chalcopyrite structure with the (112) preferred orientation, while the second peak observed at 2θ~48^{o} is designated to the main peak of α-Ga_2Se_3 phase with (220) orientation [77]. The increase in crystallinity was observed with increasing annealing temperature, which is understood from the development of more intense reflections of $AgGaS_2$ and α-Ga_2Se_3 phases. The increase in the crystallinity is possibly due to the decrease in structural disorder with increasing annealing temperature up to 550 ^{o}C. The α-Ga_2Se_3 is becoming the dominant phase at annealing temperature of 550 ^{o}C and further increases in annealing above this value result in a faster development of α-Ga_2Se_3 phase as compared with $AgGaS_2$. In addition, a drastic change is observed in $AgGaS_2$ at 600 ^{o}C annealing temperature, which is the clear sign of decomposition at high annealing temperature that results in the out-diffusion of excess sulphur to the surface of film with the same manner as stated in the reported article [13]. The weakly bounded excess sulphur atoms in the structure are probably released at high temperatures and segregate to the surface of films. With further increasing in annealing temperature, a third reflection peak starts to seen at 2θ ~56.7 ^{o} at 550 ^{o}C and fourth peak at 2θ ~13 ^{o} at annealing temperature of 600 ^{o}C as shown in Fig.4.3. Third peak is found to be belonging to Ga_2S_3 phase with JCPDS card no 48-1433. In addition, fourth peak is assigned to (111) reflections of S phase with JCPDS card no 13-0141. A similar behaviour was reported previously [78] and attributed to the segregation of volatile elements within the film structure toward the surface of films and finding considerable chance for aggregate and then forming segregated element-rich phases. In our case, by the help of the EDXA and XRD results, it is possible to suggest that with increasing annealing at/above 550 ^{o}C Ga and S probably start to segregate to the surface of films and find remarkable chance for the development of S and Ga_2S_3 phases. Thus, the observed formations of Ga_2S_3 at 550 ^{o}C and S phases at 600 ^{o}C annealing temperature are the indication of segregation of Ga and S to the surface of films. Moreover, the decrease in reflection peak intensity of $AgGaS_2$ phase at annealing temperature of 600 ^{o}C could be closely related with the decomposition of $AgGaS_2$ and turning into new phases of Ga_2S_3 and S at high temperature.

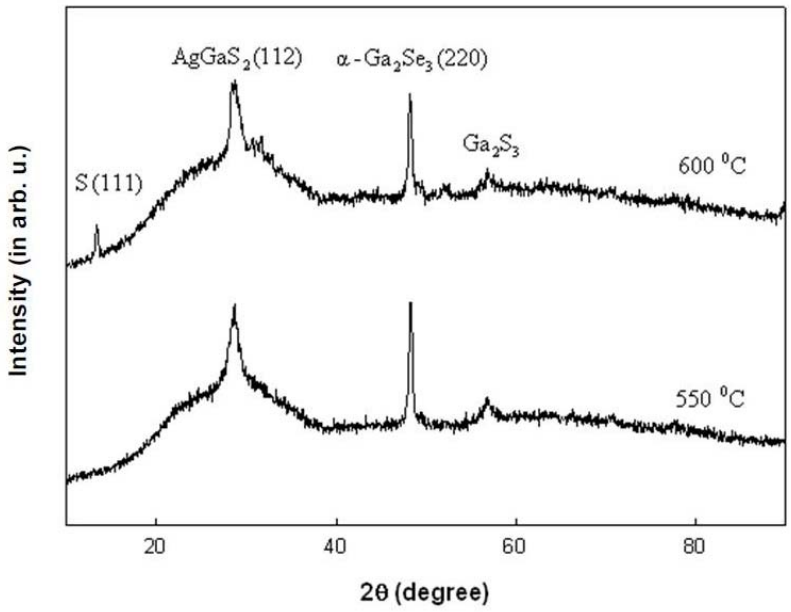

Figure 4.3: X-ray diffraction patterns of $AgGa(Se_{0.5}S_{0.5})_2$ thin films annealed at 550 and 600 ^oC.

In addition, the formation of new phase may be due to its synthesis from the amorphous to non-equilibrium phase where diffusion phenomena takes place through grain boundaries and excess defects in the structure providing low energy diffusion channels [72]. In our case, in summary, by considering EDXA results (existence of excess sulphur and gallium in the structure) we can suggest that the diffusion of the excess Ga and S through grain boundaries results in formation of Ga_2S_3 and S phases at high annealing temperature.

The surface morphology of prepared as-grown and annealed thin films was determined by means of micrographs obtained from the scanning electron microscope (SEM) measurement as shown in Fig.4.4. As can be seen from picture, there is an increase in uniformity of sample surface following to the post-annealing process. Before annealing, there are large randomly distributed agglomerations over the surface as observed from the micrographs, which is attributed to incomplete solid reaction because of insufficient or absence of driving force of thermal energy. As the sample is annealed, the agglomerations almost disappear and result in a smoother, denser and more uniform topography with the aid of thermal energy supplied by post-annealing process.

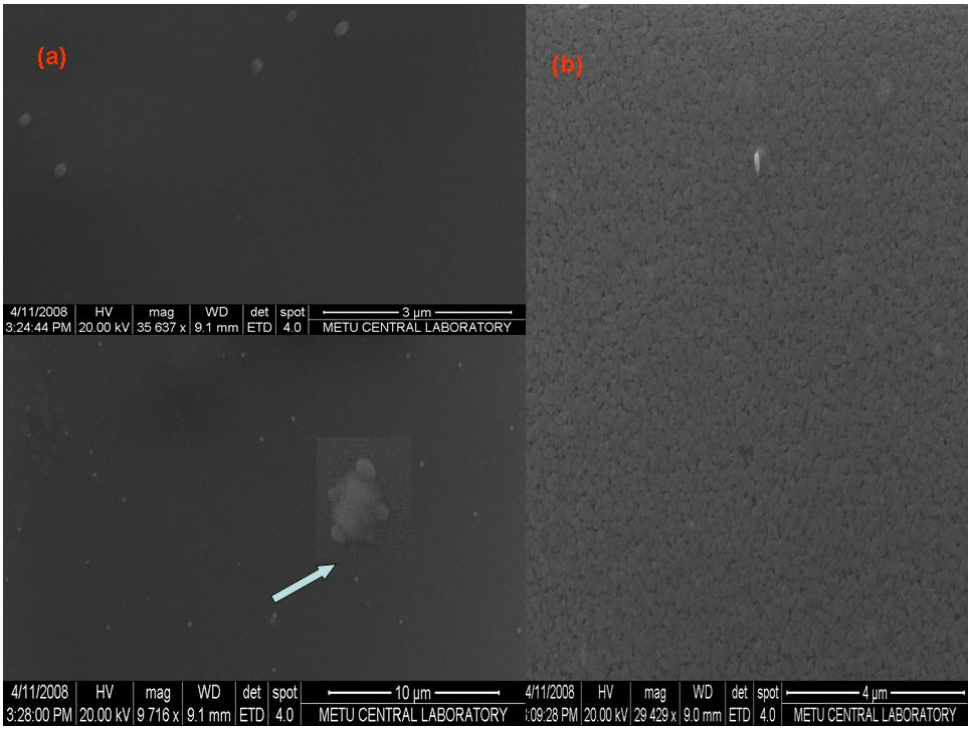

Figure 4.4: SEM micrographs recorded for (a) as-grown and (b) $AgGa(Se_{0.5}S_{0.5})_2$ thin film annealed at 600 ^oC.

The valuable knowledge about the surface composition of the surface of the prepared films has been obtained by X-ray photoelectron spectroscopy (XPS) measurement. The XPS survey spectra corresponding to as-grown and film annealed at 600 ^oC are illustrated in Fig.4.5 and Fig.4.6, respectively. As can be seen from the spectra, the Ag, Ga, Se, and S elements with corresponding photoelectron lines are clearly visible in both as-grown and annealed sample. The C 1s and O 1s photoelectron lines are also appeared in spectra, which states the presence of carbon and oxygen contamination that probably incorporated during the preparation or characterization of samples. Sample's surface was sputtered by using 2 keV Ar^+ ions for 5 min duration to reduce the amount of these contaminants (Fig.4.5 and Fig.4.6). Following to this process, the amount of these contaminants, particularly carbon is reduced substantially as compared with pre-sputtered surface. All the peaks appeared in survey spectra were identified by comparing binding energies, their chemical

shifts, and doublet separation of spin-orbit splittings with NIST XPS Database supplied values [79].

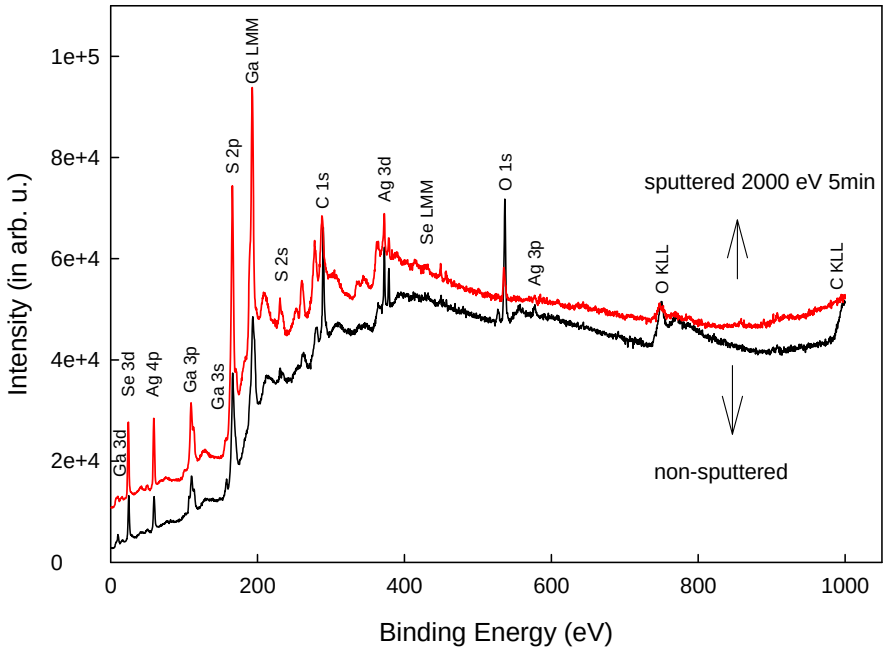

Figure 4.5: XPS survey spectrum for as-grown $AgGa(Se_{0.5}S_{0.5})_2$ thin film before and after sputtering with 2 keV Ar^+ ions.

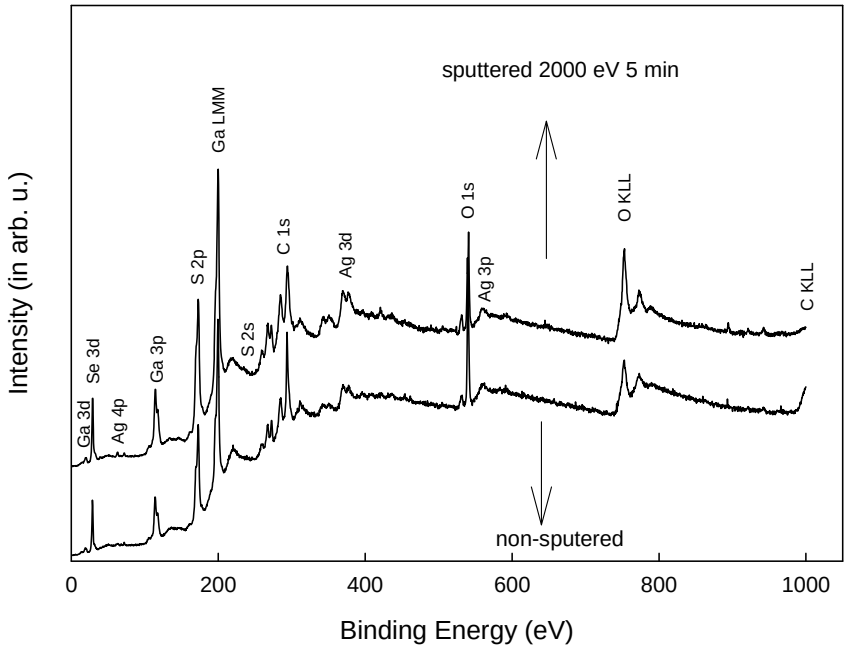

Figure 4.6: XPS survey spectrum for $AgGa(Se_{0.5}S_{0.5})_2$ thin film annealed at 600 ^oC before and after sputtering with 2 keV Ar^+ ions.

The elements identified via this way were Ag, Ga, Se, S and adventious C and O. To interpret the spectra consisted of photoelectron lines; the exact binding energy value of ejected photoelectrons is required. The well-known C 1s line with 284.6 eV is used as a reference peak to achieve this. Namely, it is used to correct the shift in binding energy stemming from the surface charge built up as ejected photoelectrons leaves the material surface.

To deduce the effect of post-annealing on the surface composition of films, the XPS survey spectra of as-grown and film annealed at 600 ^{o}C were compared as indicated in Fig.4.7.

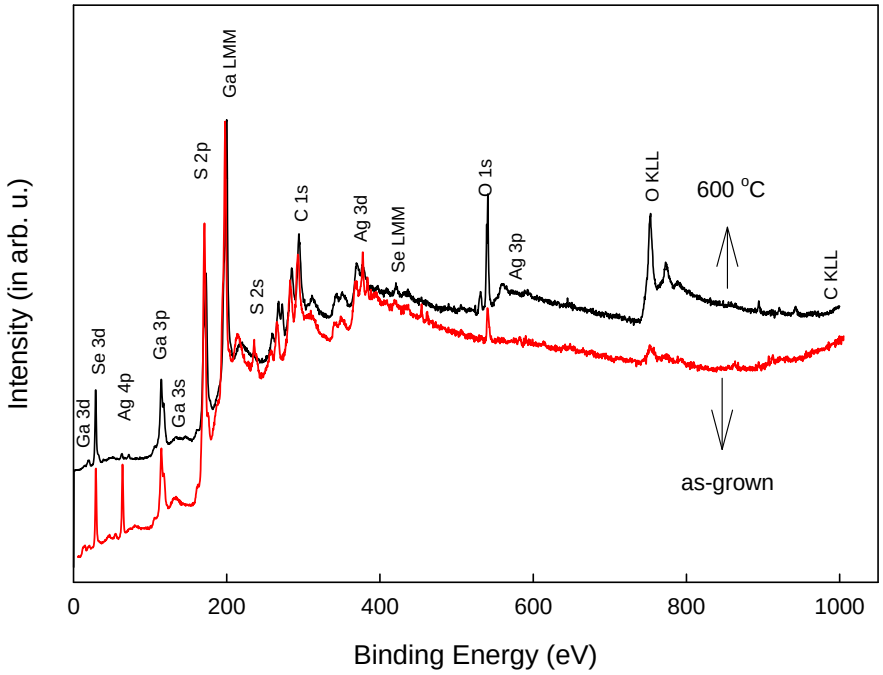

Figure 4.7: XPS survey spectra of as-grown and $AgGa(Se_{0.5}S_{0.5})_2$ thin film annealed at 600 ^{o}C after sputtering with 2 keV Ar^{+} ions.

As can be seen from the Fig.4.7, there is a decrease in amount of almost all constituent elements and an increase in oxygen contamination following to post-annealing process. However, the drastically change was observed for S and Ag. The substantial change in S obtained from XPS study after annealing is consisted with behaviour understood from XRD study. The agreement and cooperation between these measurements allow us to suggest that the out-diffusion of weakly bounded

sulphur in the structure to surface and subsequently volatilization is triggered with annealing. On the other hand, the opposite behaviour is valid for the silver, namely, post-annealing triggers the diffusion of Ag from the upper to lower layers in the material that can be easily understood from the EDXA and XPS studies.

4.2.3 Optical Analysis

In order to investigate the optical properties of the $AgGa(Se_{0.5}S_{0.5})_2$ thin films, transmittance measurements were carried out in between 300-1100 nm at room temperature. By using the transmission spectra, absorption coefficient is calculated by using the relation;

$$\alpha = \frac{1}{d} Ln\left(\frac{I_0}{I}\right) \tag{4.1}$$

where d is the thickness, I is the intensity of transmitted light, and I_0 is the incident light perpendicular to the surface of sample. The absorption coefficient varies with photon energy $h\nu$ as;

$$(\alpha h\nu) = A\left(h\nu - E_g\right)^n \tag{4.2}$$

where A is a constant, E_g is the band gap energy. Here, n is the index taking values according to the type of transition, which is ½ value for direct allowed transition and *2* for indirect transition [80]. From the plot of $(\alpha h\nu)^{1/n}$ versus $h\nu$, it is possible to determine the type of transition (direct or indirect). Fig.4.8 shows the typical plot of transmission versus wavelength. As can be seen from the figure, there is no a considerable change in transmission with the annealing. The general behaviour of absorption coefficient as function of photon energy (Fig. 4.9) in all plots is almost same except the shifting of absorption edge slightly to different energies with annealing. By extrapolating the linear regions of plots to $(\alpha h\nu)^2 = 0$, the band gap values were found to be 2.68, 2.85, 2.82, 2.83, and 2.81 eV for as-grown, annealed at 450, 500, 550, and 600 ^oC samples, respectively. There is a shifting in band gap toward high energy when the transformation from amorphous to polycrystalline phase takes place at 450 ^oC annealing temperature. However, there is no any

considerable change in optical band gap of the samples with further increasing in annealing temperature above 450 ^{o}C. That is, the optical band gap value initially decreases from 2.85 to 2.82 eV with increasing annealing from 450 to 500 ^{o}C, and then shows a slight increase to 2.83 eV from 500 to 550 ^{o}C, and finally a slight decrease to 2.81 eV with further increase of annealing to 600 ^{o}C. In the amorphous form, the degree of disorder and the density of defects are more pronounced than in polycrystalline phase. In general, the decrease in disorder and defect density in the structure gives rise to increase in the optical band gap. In addition, the saturation of dangling bonds in the amorphous structure results in increase in band gap [81]. So, the shifting of band gap to the higher energy side during the phase transformation from amorphous to crystalline could be attributed to the better crystallization of $AgGa(Se_{0.5}S_{0.5})_2$ thin films with post-annealing .

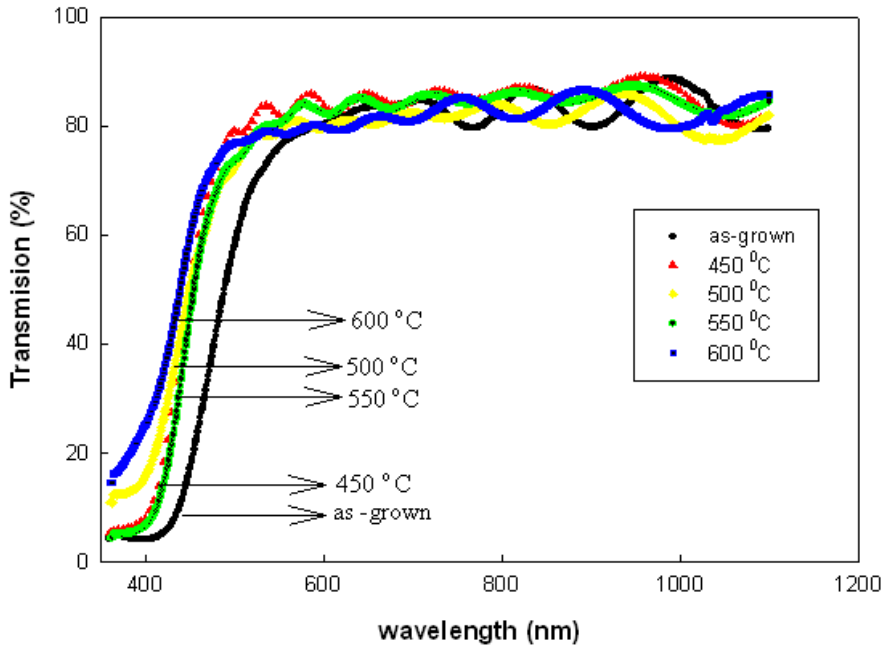

Figure 4.8: Transmission of as-grown, and annealed $AgGa(Se_{0.5}S_{0.5})_2$ thin films at 450, 500, 550, and 600 ^{o}C.

The variation in the band gap energies may also be a consequence of decomposition and creation of new phases with annealing treatment as observed in XRD study. Furthermore, the increase in band gap might be due to the improvement in the crystallinity of existence $AgGaS_2$ and Ga_2S_3 phases observed up to specific annealing

temperature. A similar behaviour is reported for InSe thin films such that the optical band gap increasing with annealing was attributed to the selenium loss at high temperatures as well as the formation of different phases [82-83].

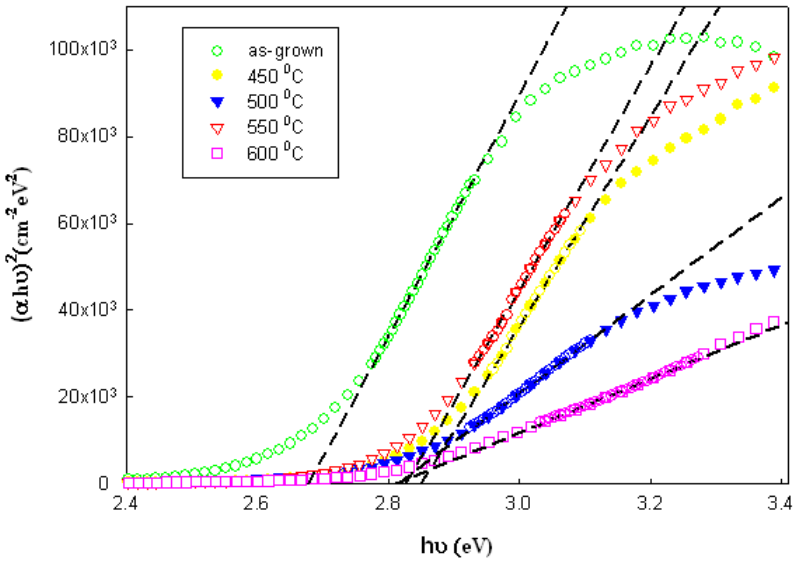

Figure 4.9: Variation of absorption coefficient with photon energy for as-grown and $AgGa(Se_{0.5}S_{0.5})_2$ thin films annealed at 450, 500, 550, and 600 ^oC.

4.2.4 Electrical Analysis

Temperature dependent conductivity measurements were carried out in the temperature range 250-430 K for the as grown, and $AgGa(Se_{0.5}S_{0.5})_2$ thin films annealed in the temperature range of 300, 450, 500, and 550 ^oC. The room temperature resistivities are calculated to be 0.7 x 10^8, 0.5 x 10^8, 0.2 x 10^8, 0.3 x 10^8, and 0.9 x 10^7 Ω-cm, respectively. The temperature dependent conductivity for as grown and annealed $AgGa(Se_{0.5}S_{0.5})_2$ thin films is shown in Fig.4.10.

The conductivity can be expressed by the Arrhenius relation

$$\sigma = \sigma_0 \exp\left(\frac{-\Delta E}{kT}\right) \tag{4.3}$$

where σ_0 is the pre-exponential factor, ΔE is the conductivity activation energy in

specific temperature range, k is the Boltzmann's constant and T is the absolute temperature. The activation energy values are estimated from the relation between the $Ln\ \sigma$ and T^{-1}. As it is clearly seen in plot, the conductivity is increasing substantially with increasing temperature for both as grown and annealed $AgGa(Se_{0.5}S_{0.5})_2$ thin films. Moreover, it is seen that the variation of $Ln\ \sigma$ versus T^{-1} shows three linear regions for as grown thin films with different activation energies (ΔE), which describes different conduction mechanisms taking part in the conduction process at specific temperature intervals.

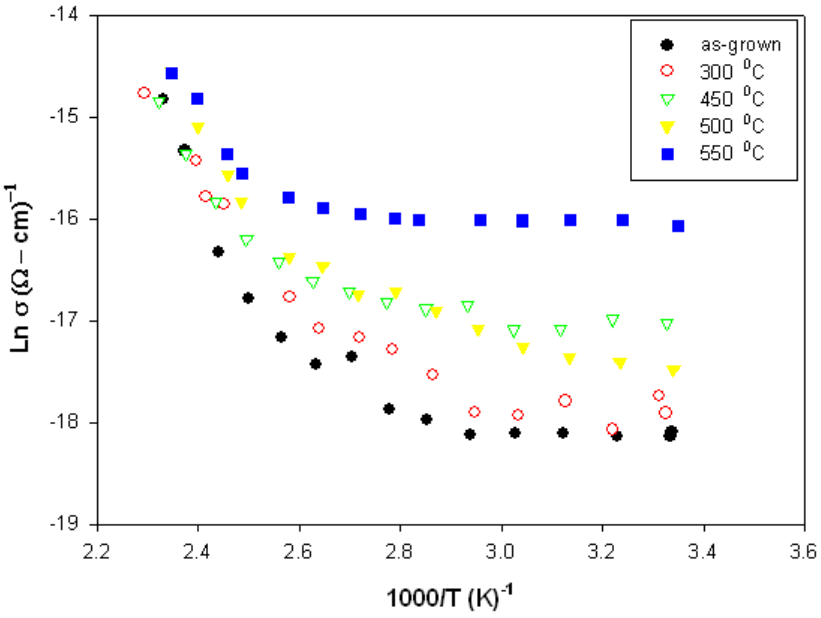

Figure 4.10: The temperature dependent electrical conductivity of as-grown, and $AgGa(Se_{0.5}S_{0.5})_2$ thin films annealed at 300, 450, 500, and 550 °C.

These regions are 250-300, 340-370, and 380-430 K with activation energies 49.2, 134.6, and 496.4 meV, respectively. However, for annealed thin films it is observed that each $Ln\ (\sigma)$ versus (T^{-1}) plot consists of two linear regions that present the presence of two different thermally activated conduction mechanisms. These regions and activation energies for annealed $AgGa(Se_{0.5}S_{0.5})_2$ thin films are summarized in Table 4.2. The absence of systematic variation in activation energies with annealing is possibly due to the complex nature of structure that is consisted of mixture of

single, binary, and ternary phases. The conduction process is governed by grain boundaries in polycrystalline structure, which act as potential barriers for the free carriers and limit the conductivity. The increase in grain size with heat treatment reduces the amount of these barriers and their potential that traps free carriers. Thus, the improvement observed in crystallinity may be responsible for changes observed in conductivity.

Table 4.2: Activation energies for as-grown, and annealed $AgGa(Se_{0.5}S_{0.5})_2$ thin films

Temperature (^oC)	ΔE_1 (meV)	ΔE_2 (meV)
300	148.4 (310-370 K)	577.6 (380-430 K)
450	24.6 (250-370 K)	493.2 (380-430 K)
500	40.4 (260-310 K)	274.7 (320-430 K)
550	17.1 (250-310 K)	393.1 (380-430 K)

Namely, higher annealing temperature results in low resistive samples as result of the structural modifications.

4.3 Characterization of $AgGaSe_2$ Thin Films Deposited by Electron Beam Technique

4.3.1 Introduction

In this study, the structural and morphological properties of $AgGaSe_2$ thin films deposited by electron-beam technique have been studied using X-ray diffraction (XRD), scanning electron microscopy (SEM), and X-ray photoelectron spectroscopy (XPS) measurements.

The $AgGaSe_2$ single crystals have been grown from the prepared stoichiometric mixture of constituent elements of pure indium, gallium and selenium fused in a quartz ampoule. A Crystalox MSD-4000 model three zone vertical

Bridgman-Stockbarger system was used for the growth of single crystals of $AgGaSe_2$ to be used as evaporation source. The deposition of $AgGaSe_2$ thin films have been carried out on to the soda-lime glass substrate under the vacuum with base pressure of 10^{-6} Torr. The deposition parameters such as substrate temperature and thickness of the deposited films were 200 ^{o} C and 2.0 μm, respectively. The samples were annealed in the range of 300-600 ^{o} C for 30 minutes under the nitrogen atmosphere to determine how post-annealing effects the properties of films.

4.3.2 Composition Analysis

To investigate the chemical composition of source powder and deposited $AgGaSe_2$ thin films energy dispersive X-ray analysis (EDXA) measurements were carried out, results of which are listed in Table 4.3. The results show that powder has a nearly a stoichiometric composition, with the atomic ratio of Ag:Ga:Se is 23,13:23,99:52,88 %. A typical EDXA spectrum obtained for as-grown $AgGaSe_2$ thin film is shown in Fig.4.11. The EDXA measurement was operated at two different acceleration energies to measure the composition at different depths since the range of electron penetration depends on the incident electron-beam energy. An electron beam with relatively low energy (6 kV) was chosen for the determination of surface or near surface region, while for the deeper layers a more energetic electron beam (30 kV) was preferred. From the measurement conducted at 6kV it was found that the as-grown films have an Ag-rich but Ga- and Se- deficient composition. Upon elevating annealing temperature from 450 to 600 ^{o}C, it was observed that there is a systematic decrease in atomic percentage of Ag and increase in that of Ga and Se constituent elements on the surface of deposited films, which is perfectly consisted with the results obtained from the XPS measurement shown in Fig.4.12. The measurement performed at 30 kV exhibits a similar behaviour in terms of variation in amount of constituent elements following to post-annealing treatment. As can be easily understood from the results of EDXA measurements, prepared films are non-stoichiometric, and the amount of Ag obtained in 6 kV is more than that obtained in 30 kV for the as-grown films.

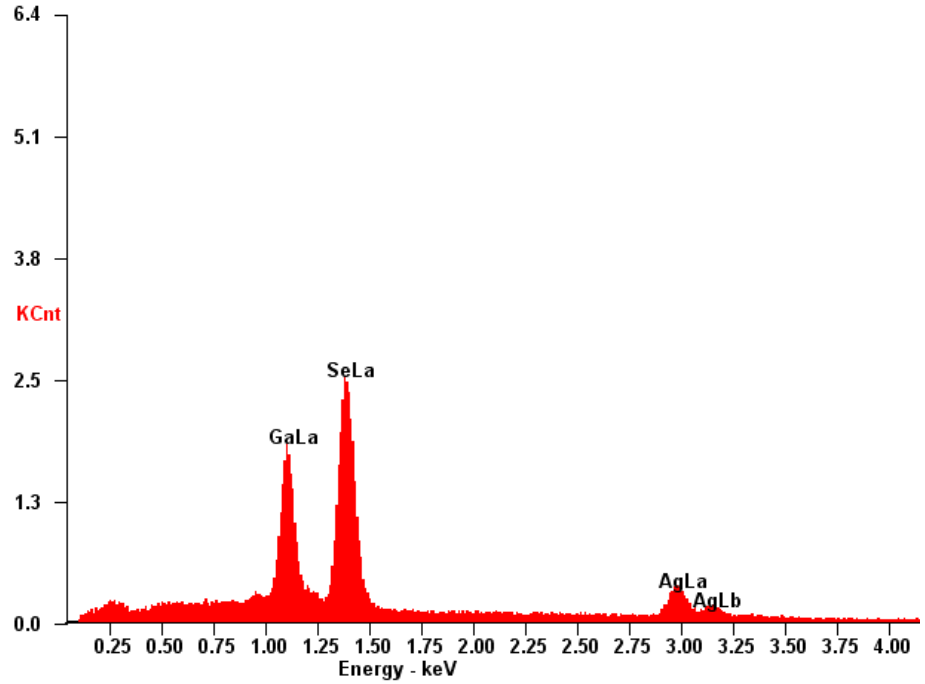

Figure 4.11: A typical EDXA spectrum for as-grown $AgGaSe_2$ thin film

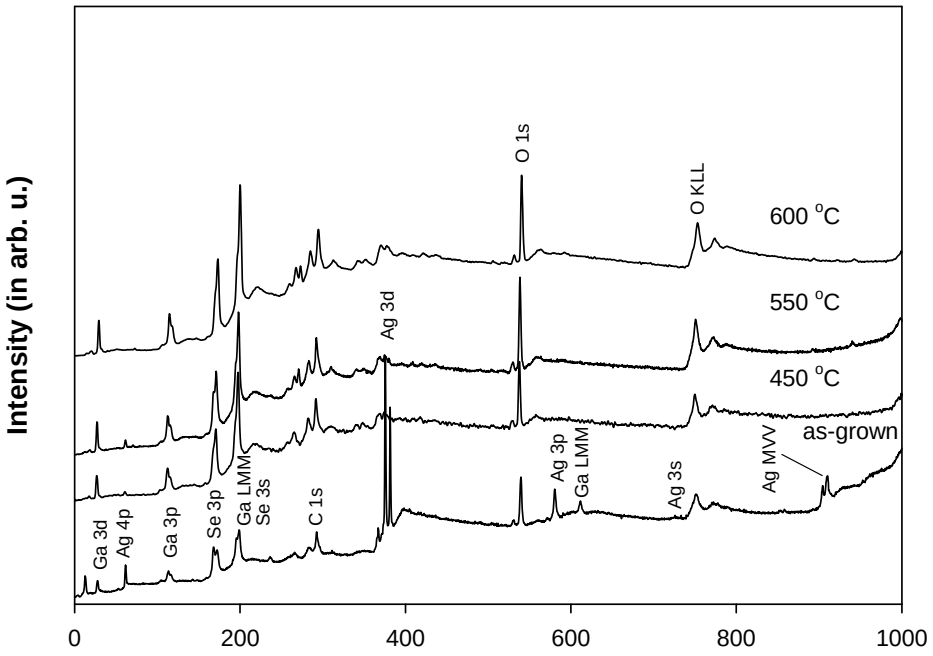

Figure 4.12: XPS survey spectrum recorded for as-grown, and $AgGaSe_2$ thin films in the temperature range of 450-600 ^{o}C.

Table 4.3: EDAX results of as-grown and annealed $AgGaSe_2$ thin films in the temperature range of 450-600 ^{o}C

Sample	6 kV			30 kV		
	Ag at %	Ga at %	Se at %	Ag at %	Ga at %	Se at %
As-grown	36.17	22.51	41.32	13.76	33.71	52.53
450 ^{o}C	16.09	40.92	42.99	12.18	34.51	53.31
550 ^{o}C	7.52	49.11	43.38	10.51	35.07	54.42
600 ^{o}C	5.49	54.66	39.85	9.34	35.09	55.56

The higher concentration of Ag (at 6 kV) is a clear indication of an Ag-rich surface, which is also confirmed by the recorded SEM micrographs shown in Fig.4.13 and XPS measurement indicated in Fig.4.12. As can be seen in Fig.4.13, large agglomerations (spots) are present on the surface of as-grown samples and almost disappear with increasing annealing temperature. Based on EDXA measurements carried out at the different regions of film surface, it was found that these spots are belonging to silver, which was confirmed by measuring a high Ag atomic percentage (47 %) in regions includes relatively high density of such agglomerations. The disappearance of these spots with annealing may be consequence of either the diffusing of Ag atoms from surface to bulk or staying at the layer just beneath the surface mainly occupied by segregated Ga and Se atoms. The segregation of Ga and Se triggered at high annealing temperature may be the plausible reason behind the increase in the number of the spots on the surface. The decline in Ag and increase in Ga and Se are clearly observed from the XPS survey spectrum shown in Fig.4.8.

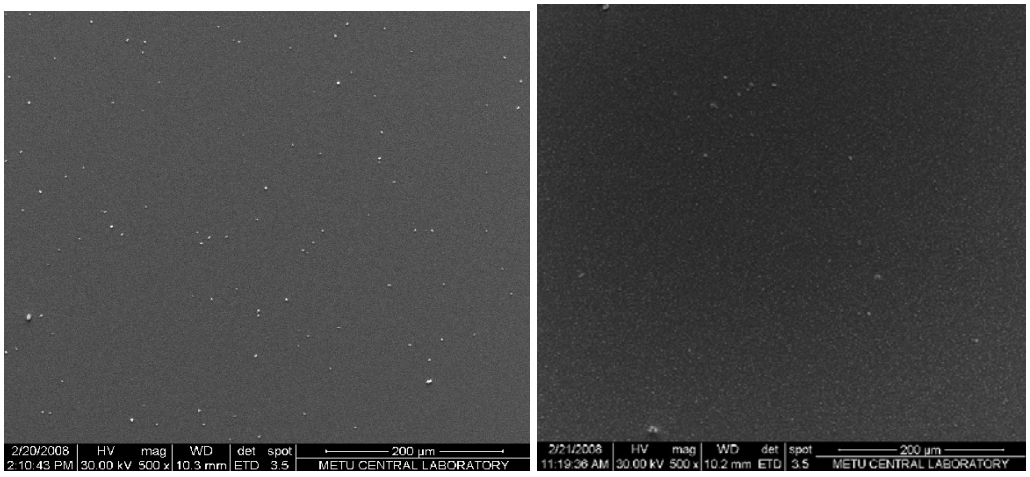

(a) (b)

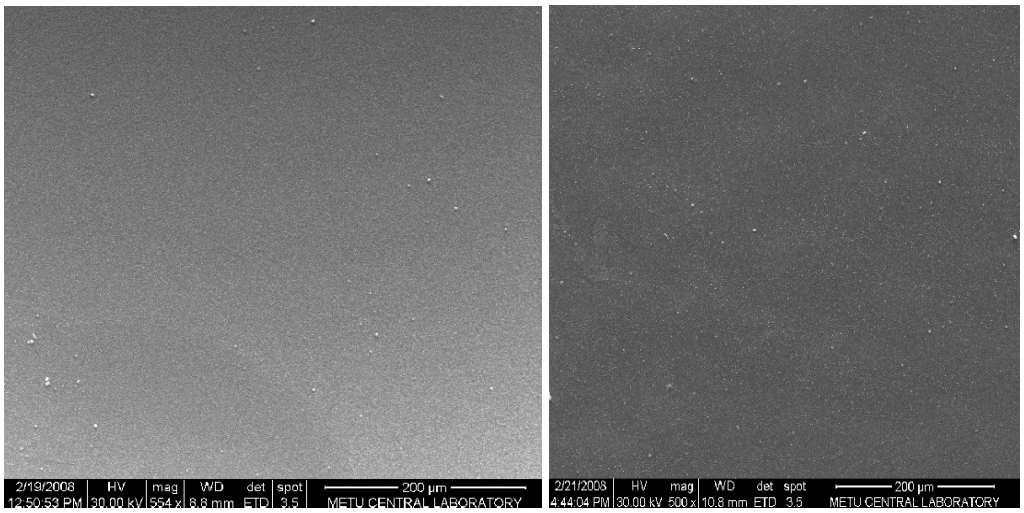

(c) (d)

Figure 4.13: SEM micrographs recorded for (a) as-grown, and $AgGaSe_2$ thin films annealed at (b) 450, (c) 550, and (d) 600 ^{o}C.

4.3.3 Structural Analysis

Diffractogram obtained from XRD measurement for powder used in the deposition of $AgGaSe_2$ thin films is displayed Fig.4.14. It reveals that prepared source powder is in the single crystalline form containing mono-phase $AgGaSe_2$ [84] having tetragonal structure with the lattice parameters a = 5.993, b = 5.993, and c = 10.884 Å. The high intensity of reflection from the (112) plane indicates that $AgGaSe_2$ has chalcopyrite structure with the preferred orientation along this direction. As can be seen from Fig.4.15, the as-deposited film is in amorphous structure, while after annealing at

300 ^{o} C it is observed that the amorphous phase turns into polycrystalline structure including small crystallinities of Ag phase [85] with the reflections along (111) and (220) directions. There is no any modification in terms of improvement in the crystallinity on annealing sample at 350 ^{o} C, however, the increase in intensity and decrease in full-width at half-maximum (FWHM) of the Ag (111) reflection peak at the annealing temperature of 450 ^{o} C indicates the improvement in crystallinity. In addition, two new phases are developed at this temperature corresponding to GaSe [86] with (004), (101), and (110) and Ga_2Se_3 [87] with (220) plane reflections. Further annealing at 500 ^{o} C results in decreases in the intensity of Ag (111) and the arising of $AgGaSe_2$ phase with (112) reflection. On increasing annealing temperature to 550 ^{o}C, co-existence of three phases, Ga_2Se_3, GaSe, and $AgGaSe_2$, was detected. In addition, as XRD peaks of Ag disappear perfectly, there is a sharp increase in that of $AgGaSe_2$ phase with (112) orientation. Moreover, the other reflection peaks of $AgGaSe_2$ phase indexed with (220), (204), (312), (400), (316) and (424) appears at this temperature. The plausible reason behind the vanishing of Ag is the promotion of solid state reaction taking place between Ag and binary selenides, GaSe and Ga_2Se_3 that ends up with the formation of $AgGaSe_2$ at high annealing temperature (550 ^{o}C).

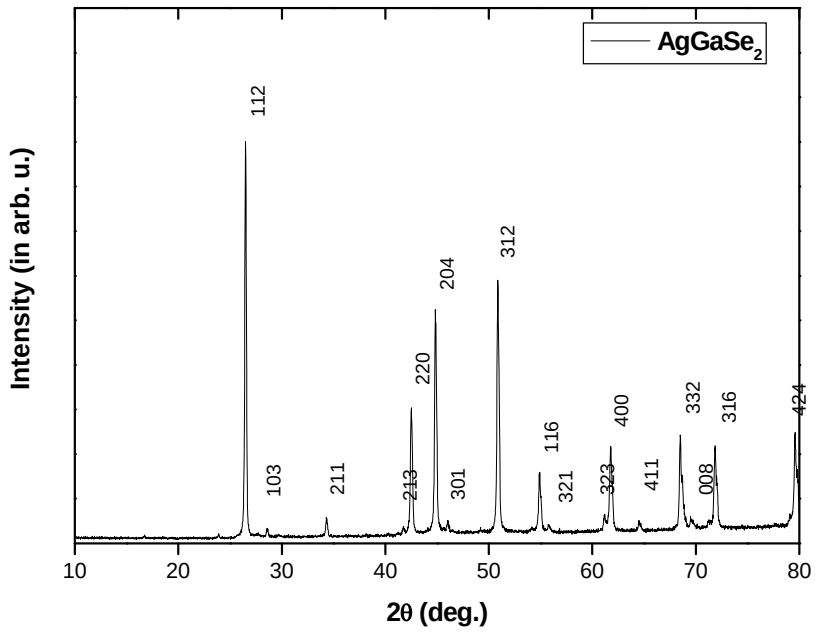

Figure 4.14: XRD patterns for powder $AgGaSe_2$ single crystal.

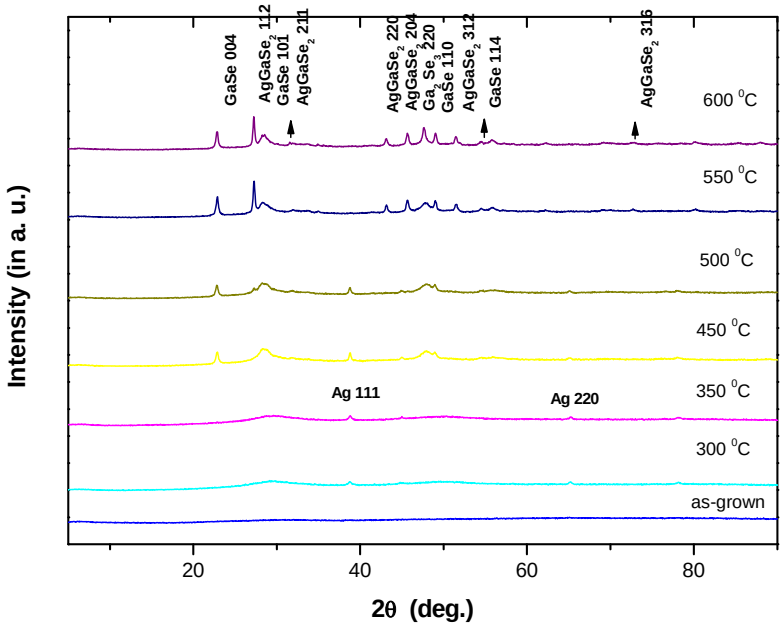

Figure 4.15: X-ray diffraction patterns of as-grown, and $AgGaSe_2$ thin films annealed at 300, 350, 450, 500, 550, and 600 ^{o} C.

During the deposition cycle the impinged Ag atoms were immobile due to the absence of sufficient thermal energy so as to join the nucleation centres formed at early stage of crystallization. However, on increasing annealing temperature Ag atoms gain sufficient thermal energy in order to be mobile and find a considerable chance to join in the formation of $AgGaSe_2$ together with binary selenides. After annealing at 600 ^{o}C, it was observed that there is a remarkable improvement in the crystallinity of Ga_2Se_3 and small decrease in intensity of (004) reflection peak belonging to GaSe, while there is no any noticeable modification in all reflection peaks of $AgGaSe_2$. Based on XRD results, the process taking place in the structure with annealing can be explained like that there is excess Ag on the surface of films at low annealing temperature, however, increasing annealing temperature give rise to the segregation of Ga and Se segregation to the surface, which results in systematic decrease in Ag and increase in Ga and Se atomic percentages on the surface as observed from the EDXA results. The Ga- and Se- rich surface at high annealing temperature promotes the reaction probability between Ga and Se for the formation of GaSe and Ga_2Se_3 binary phases. The appearance of $AgGaSe_2$ at so high temperature can also be explained by the model of "survival of the fastest" proposed

by van der Drift [88]. This model states that it is possible for various nuclei belonging to the different phases formed at the initial stage of the crystallization and each one competes to grow but it will be possible for some of them only having the fastest growth rate to survive. The grow rate of GaSe and Ga_2Se_3, in our case, is the dominant at low annealing temperature, but at high annealing temperatures $AgGaSe_2$ wins this competition. In summary, based on XRD results it is possible to claim that the formation of single phase $AgGaSe_2$ requires high annealing temperatures, which couldn't be tested over 600 ^oC because of melting point of the glass substrate.

4.3.4 Surface Morphology

The SEM micrographs recorded for as-grown and annealed $AgGaSe_2$ thin films are shown in Fig.4.16. It reveals that post-annealing has a strong influence on morphology of the deposited films, which results in the variations in the grain sizes such as between (128-192 nm), (151-397 nm), (82-403 nm), and (169-526 nm) for the as-grown, sample annealed at 450, 550 and 600 ^{o} C, respectively. The deviation from stoichiometry, as consequence of the segregation, has also an important effect on the morphology of the deposited films. The variations observed in grain sizes on annealing at different temperatures could also be attributed to the structural modifications witnessed in XRD analysis. The increase observed in range of grain sizes after increasing annealing temperature is possibly due to the coalescence of pre-formed nucleated centres corresponding to binary selenides driven by thermal energy. The modifications due to creation or decomposition of nuclei may result in change the type of nucleation from homogenous to heterogeneous observed in SEM images illustrated in Fig.4.16.

The observed systematic increase in some type of grains on increasing annealing is probably related to continuously grown GaSe and Ga_2Se_3 binary selenides formed at the early stage of crystallization. The large agglomerations (or spots) seen at high annealing temperature might be due to the coalescence of the grains belonging to binary selenides and silver to form $AgGaSe_2$ phase seen at high annealing temperatures.

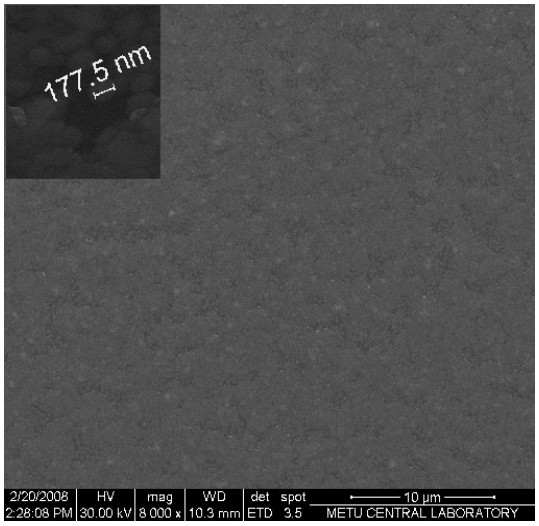

(a)

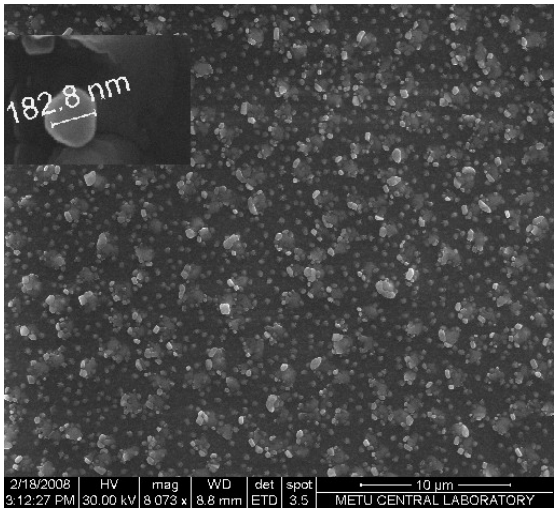

(b)

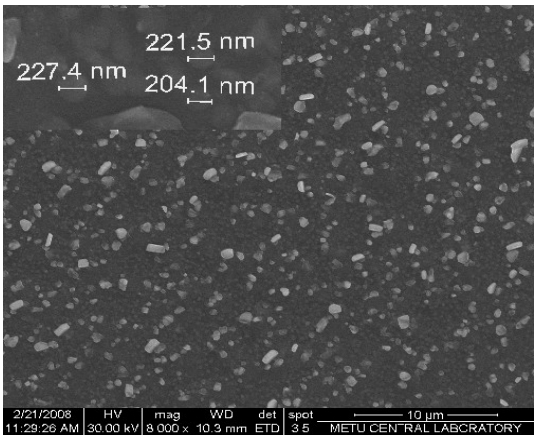

(c)

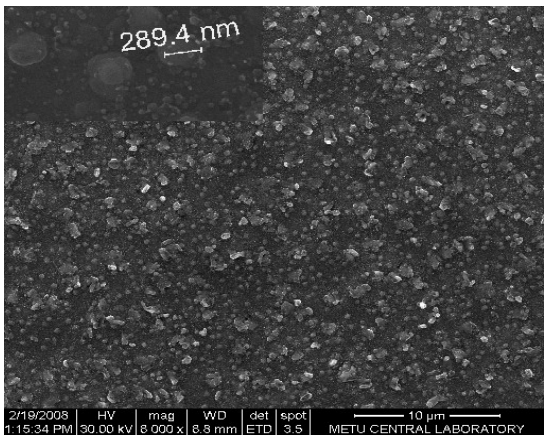

(d)

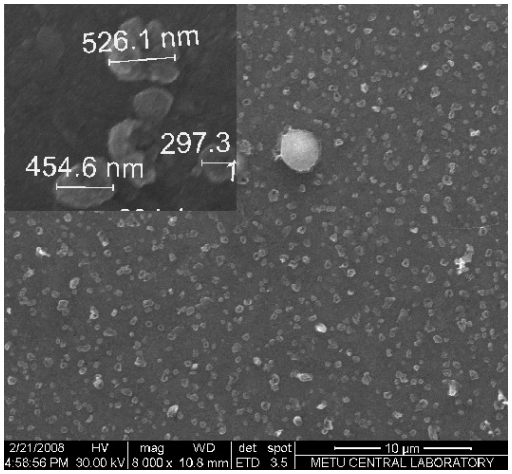

(e)

Figure 4.16: SEM images of (a) as-grown, and $AgGaSe_2$ thin films annealed at (b) 300, (c) 450, (d) 550, and (e) 600 ^{o}C.

On the other hand, the arising of small droplets on the surface with increasing annealing is possibly due to the segregation of constituent elements of Ga and Se to the surface that also observed from the EDXA and XPS results, which point out that there is a systematic increase in the percentage of Ga and Se concentration on the surface with increasing annealing temperature. Also, this segregation results in formation of binary selenides constructed in a Ga - and Se - rich environment.

4.3.5 Chemical Composition Analysis

The composition and chemical states of elements at surface or near - surface region of deposited $AgGaSe_2$ thin films have been determined by performing XPS measurement conducted by using Mg K_α line, 1235.6 eV, at power 195 W with the constant mode pass energy of 48 eV. The C 1s photoelectron peak at 284.6 eV was selected as the reference for the calibration of binding energies. Fig.4.17 shows the XPS spectrum of as-grown $AgGaSe_2$ thin films. The existence of carbon (C) and Oxygen (O) in the spectra is possibly because of effect as carrying the samples to the measurement system. In order to reduce the amount of it, the samples were sputtered for 2 minutes by Argon (Ar) ions with energy of 2000 eV. As can be seen from Fig.4.17, the concentrations of C and O decrease substantially following to this process.

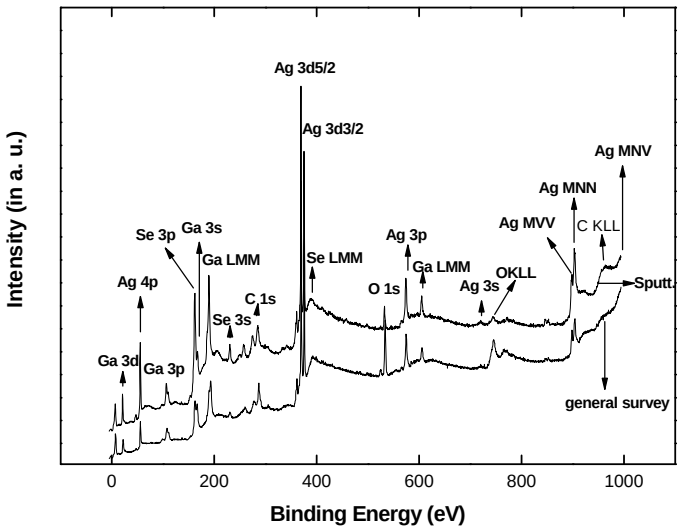

Figure 4.17: XPS survey spectra of the as-grown $AgGaSe_2$ thin films before and after sputtering with Ar^+ at 2 keV for 2 min.

The XPS spectra show that Ag, Ga, Se, C, and O elements are appeared in all samples. To identify chemical states of elements, the dominant peaks of Ag (3d), Ga (3p), and Se (3p) photoelectron peaks were analysed by applying fitting procedure. It can be summarized as; the background elimination by applying Tougard model, the decomposition of specified photoelectron peak by selecting Gaussian and Lorentzian fitting functions, checking the preservation of right intensity ratio for spin-orbit splitting doublets for photoelectrons emerged from p, d, and f orbitals, calibration of binding energies, and comparison of calculated binding energies with reported ones supplied by NIST database regarding either chemical shift and binding energy or doublet separation for spin-orbit splittings. The intensity ratio for the doublet lines should preserve the correct value, which is 1:2, 2:3, and 3:4 for p, d, and f lines, respectively [53]. The evaluation of Ag 3d photoelectron peak of as-grown and annealed $AgGaSe_2$ thin films is illustrated in Fig.4.18. The Ag 3d spectrum was indicated by doublet terms Ag 3d5/2 and Ag 3d3/2 well separated due to the existing spin-orbit coupling. The analysis was conducted on Ag 3d5/2 for the identification of Ag chemical states. As indicated in Fig.4.18, the Ag 3d5/2 deconvoluted into four components up to 450 ^{o}C and then reduced to three with increasing annealing temperature to 550 ^{o}C. The observed and reported binding energies of components of Ag 3d5/2 levels in specific chemical structures are presented in Table 4.4 for each component of as-grown and annealed samples in the temperature range of 300-550 ^{o}C. Since the area of each component peak is a measure of the existence of phase, on the top (or near) surface region, it is clearly seen that Ag_2Se is the dominant phase as compared to the other identified states of AgO and Ag in the as-grown films. As can be seen from the spectrum of annealed samples, the Ag and Ag_2Se are decreasing with increasing annealing temperature and disappears at 450 and 550 ^{o}C, respectively. On the other hand, the $AgGaSe_2$ appears at 450 ^{o}C and grows at 550 ^{o}C. The identified binary phases of AgO and Ag_2Se were not observed in XRD studies, which is probably stemming from the presence of these states either at the surface or at grain boundaries. A similar behaviour was reported by R. Caballero *et al* [89]. The observed increase in oxide state of Ag might be due to the air exposure after repeating several annealing following to the sputtering process during XPS measurements.

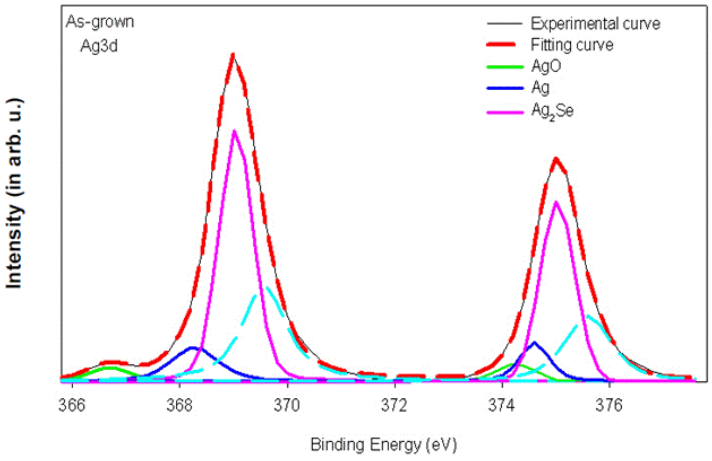

(a)

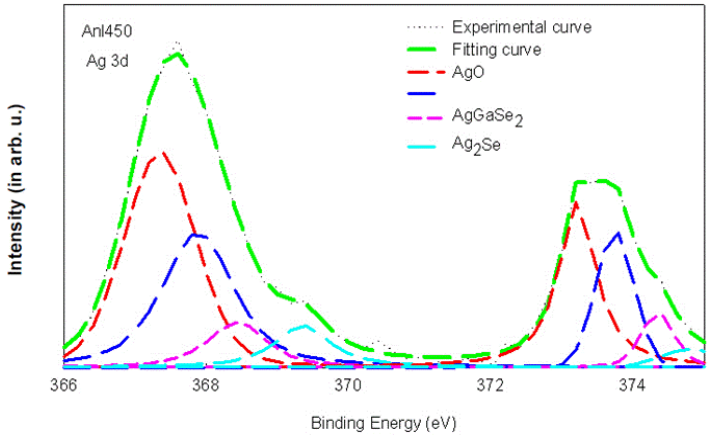

(b)

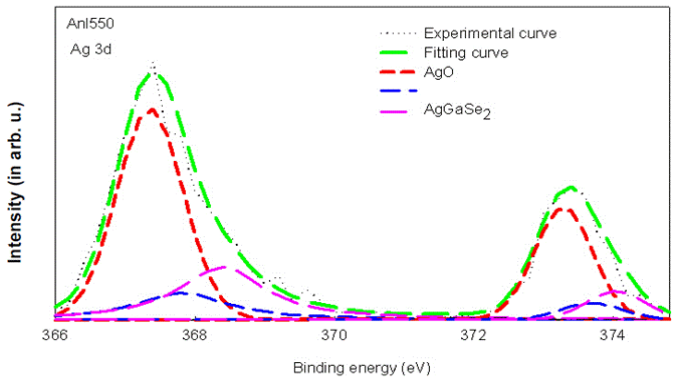

(c)

Figure 4.18: The Ag 3d spectra for (a) as-grown, and $AgGaSe_2$ thin films annealed at (b) 450, and (c) 550 ^{o}C.

The observed change in Ag and Ag_2Se are in good agreement with the results obtained from XRD and EDXA analysis. That's, in the early stage of crystallization there is an Ag-rich surface that gives a chance to Ag atoms to form the bonds as Ag-Ag and Ag-Se on the surface (or near the surface) region. On increasing annealing temperature the Ag-Ag and Ag-Se bonds are possibly broken and released Ag and Se atoms are used either in the formation of $AgGaSe_2$ or AgO observed at high temperatures.

The deconvolution of Ga 3p spectra for as-grown and annealed $AgGaSe_2$ thin films are shown in Fig.4.19. The fitting results are summarized in Table 4.5. The Ga 3p spectra was fitted for four component peaks belonging to Ga_2O_3, $AgGaSe_2$, Ga, and an unidentified phase for as-grown films. The dominant peak was Ga_2O_3 with binding energy presented in Table 4.5.

Table 4.4: The fitting parameters of Ag 3d photoelectron line with respect to $3d_{5/2}$

Temp. (^{0} C)	Chemical formula	Observed B.E. (eV)	Reported B.E. (eV) [Ref.]	
As-grown	AgO	367.20	367.30	[90]
	Ag	368.40	368.40	[91]
	Ag_2Se	369.00	369.00	[92]
300	AgO	367.00	367.30	[90]
	Ag	368.60	368.40	[91]
	Ag_2Se	369.20	369.00	[92]
450	AgO	367.30	367.30	[90]
	$AgGaSe_2$	368.45	368.40	[91]
	Ag_2Se	369.40	369.00	[92]
550	AgO	367.30	367.30	[90]
	$AgGaSe_2$	368.40	368.40	[91]

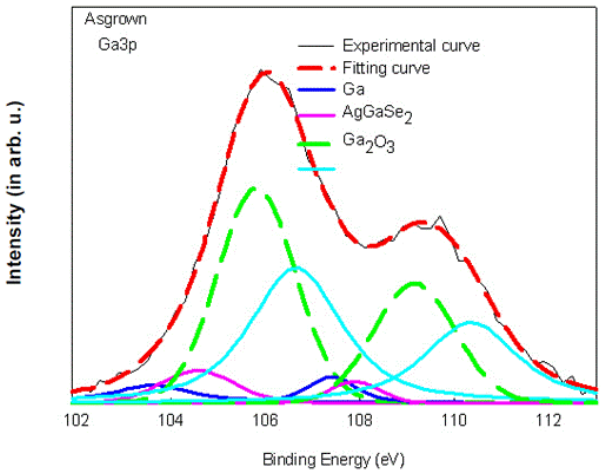

(a)

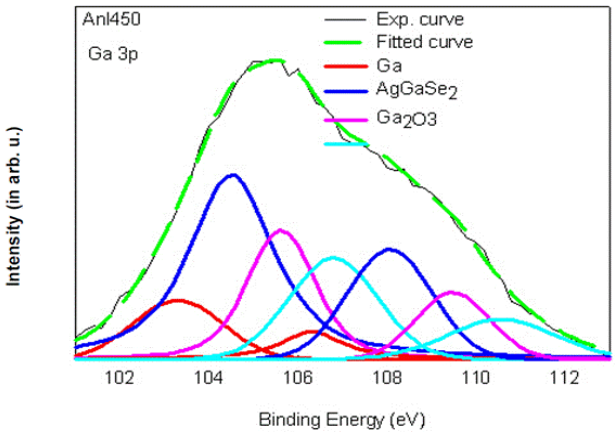

(b)

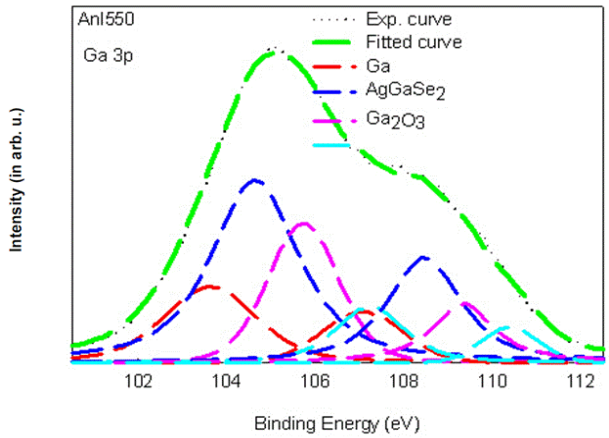

(c)

Figure 4.19: The Ga 3p spectra for (a) as-grown, and $AgGaSe_2$ thin films annealed at (b) 450, and (c) 550 ^{o}C.

And, the smaller two peaks are corresponding to $AgGaSe_2$ and elemental Ga.

Increase in annealing temperature has resulted in an increase in the intensity of Ga peak. This is in good agreement with EDXA and XPS results. The area under $AgGaSe_2$ peak initially increases from 6.9 to 7.7 % by annealing at 300 ^oC, and then a sharp increase to 45 % from 300 to 450 ^oC, and a slight increase to 45.4 % from 450 to 550 ^oC and again a slight change to 46.6 % from 550 to 600 ^oC. These variations imply the formation $AgGaSe_2$ phase with increasing annealing temperature. The Ga_2O_3 is the main component of convolution of Ga 3p in the as-grown films. It suggests that the most of the Ga on the surface (or near-surface) region is used in the construction of Ga-O bonds. The observed decrease in Ga_2O_3 on increasing annealing may be attributed to the decomposing of Ga_2O_3 at high temperature, which subsequently supplies Ga to be used in the formation of new nucleation centres belonging to binary selenides and $AgGaSe_2$ by constructing Ga-Se and Ag-Ga-Se bonds. Annealing above 450 ^oC results in the formation of Ag-Ga-Se and Ga-O bonds via the solid-solution reaction taking place between constituent elements of Ag, Ga, and Se and oxygen contaminated to the surface of films.

Fig.4.20 shows the XPS spectra of Se 3p core level for as-grown and $AgGaSe_2$ thin films annealed in the temperature range of 300-600 ^{o} C. Three states are identified from the deconvolution of Se 3p, which are corresponding to elemental Se, Ga_2Se_3, and SeO_2 with fitting parameters summarized in Table 4.6. The Se and SeO_2 chemical states were not observed in XRD analysis, which is a clear confirmation of that these phases are related with the surface states. The area under the peak of Se is increasing from 36 to 48.1 % by annealing at 300 ^oC, and then disappears perfectly at 450 ^oC, an re-appears with percentage of 12.7 at 550 ^oC, and finally shows a slight increase from 12.7 to 17.6 % on increasing annealing temperature from 550 to 600 ^oC. For the evaluation of Ga_2Se_3, we couldn't observe any systematic change following to post-annealing process. That's, it shows a sharp increase from 24.4 to 45 % from the as-grown to 450 ^{o} C, then a slight decrease from 45 to 39.6 % on increasing annealing temperature from 450 to 550 ^oC, and then considerable decrease from 39.6 to 17 % with the increasing annealing temperature from 550 to 600 ^oC. In the evolution SeO_2, it was found that there is an increase in amount this state with increasing annealing temperature. On the other hand, a decrease observed in Se with the annealing temperature up to 450 ^oC, which is

probably related with the initial crystallizations at low temperatures and subsequently the formation some surface states like binary selenides, GaSe and Ga_2Se_3, as observed in XRD patterns and the oxide form (SeO_2) deduced from XPS measurement. The increase in percentage of selenium from 450 to 600 ^oC might be the consequence of decomposition of binary phases with increasing annealing temperature for the synthesis of $AgGaSe_2$.

Table 4.5: The fitting parameters of Ga 3p photoelectron line with respect to $3p_{3/2}$

Temp. (^oC)	Chemical formula	Observed B.E. (eV)	Reported B. E. (eV)	[Ref.]
As-grown	Ga	103.60	103.50	[93]
	Ga_2O_3	105.80	105.70	[93]
	$AgGaSe_2$	104.60	104.70	[91]
	-	110.36	-	-
300	Ga	103.70	103.50	[93]
	Ga_2O_3	105.90	105.70	[93]
	$AgGaSe_2$	104.70	104.70	[91]
	-	107.10	-	-
450	Ga	103.30	103.50	[93]
	Ga_2O_3	105.62	105.70	[93]
	$AgGaSe_2$	104.51	104.70	[91]
	-	106.80	-	-
550	Ga	103.60	103.50	[93]
	Ga_2O_3	105.70	105.70	[93]
	$AgGaSe_2$	104.64	104.70	[91]
	-	107.20	-	-
600	Ga	103.30	103.50	[93]
	Ga_2O_3	105.40	105.70	[93]
	$AgGaSe_2$	104.40	104.70	[91]

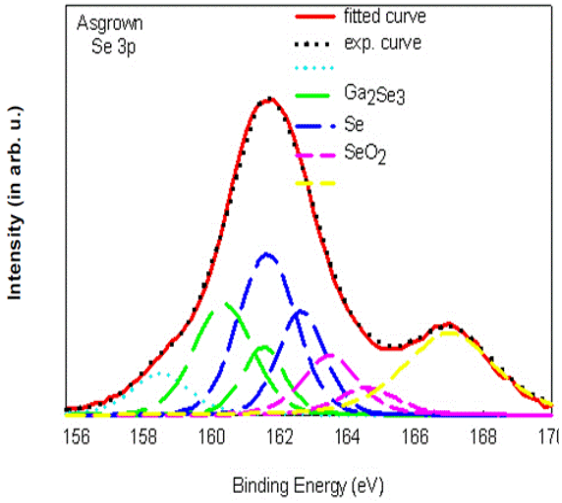

(a)

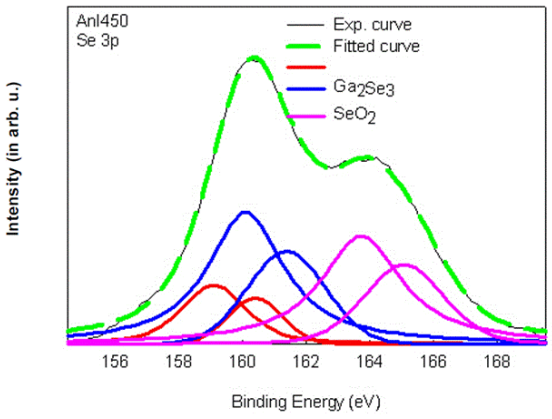

(b)

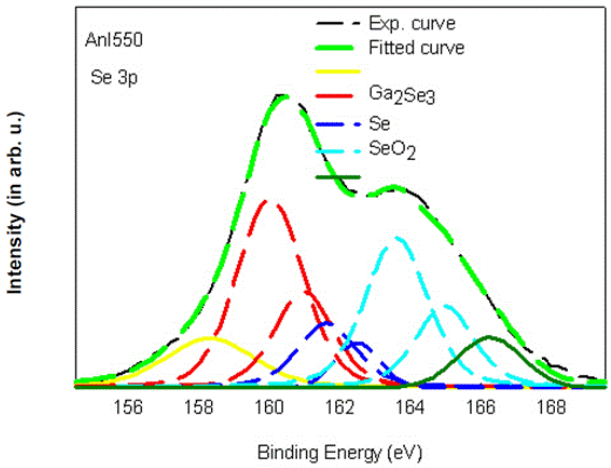

(c)

Figure 4.20: The Se 3p spectra for (a) as-grown, (b) annealed at 450, and (c) 550 ^{o}C $AgGaSe_2$ thin films.

Table 4.6: The fitting parameters of Se 3p photoelectron line with respect to $3p_{3/2}$

Anl. Temp. (^{o}C)	Chemical formula	Obs. B.E. (eV)	Reported B. E. (eV)	[Ref.]
As-grown	Ga_2Se_3	160.35	160.30	[94]
	Se	161.65	161.70	[95]
	SeO_2	163.55	163.60	[96]
	-	158.50	-	-
	-	167.00	-	-
300	Ga_2Se_3	160.30	160.30	[94]
	Se	161.80	161.70	[94]
	SeO_2	163.53	163.60	[96]
	-	158.40	-	-
	-	167.50	-	-
450	Ga_2Se_3	160.10	160.30	[94]
	SeO_2	163.70	163.60	[96]
	-	159.10	-	-
550	Ga_2Se_3	160.02	160.30	[93]
	Se	161.63	161.70	[95]
	SeO_2	163.60	163.60	[96]
	-	158.31	-	-
	-	166.25	-	-
600	Ga_2Se_3	160.10	160.30	[94]
	Se	161.60	161.70	[95]
	SeO_2	163.30	163.60	[96]
	-	158.70	-	-

4.4 Characterization of $AgGaSe_2$ Thin Films Deposited by Sputtering Technique

In this part of study, sputtering technique has been used for the deposition of $AgGaSe_2$ thin films onto soda-lime glass substrates by using sequential layer by layer deposition of GaSe and Ag thin films produced using Ag and GaSe targets by means of DC and RF magnetrons, respectively. The layer thickness optimization of Ag and GaSe was performed by conducting several deposition cycles with the same

parameters before the sequential deposition of GaSe/Ag/GaSe/Ag/GaSe/Ag/GaSe/Ag/GaSe thin film layers onto soda-lime glass substrates kept at constant temperature around 250 ^{o}C to form $AgGaSe_2$ thin film. The thickness of each layer of Ag and GaSe was around 15 nm and 130 nm, respectively. The thickness of the deposited $AgGaSe_2$ thin films was found to be varying from 705 to 720 nm depending on the position of samples on holder during the deposition process. To study the effect of annealing on the physical properties of deposited $AgGaSe_2$ thin films the rapid-annealing in the temperature range of 350-600 ^{o}C was applied under constant N_2 flow in a special designed horizontal furnace for 5 minute.

4.4.1 Structural and Compositional Analysis

Compositional analysis of the deposited $AgGaSe_2$ thin films was carried out by performing EDXA measurement at the acceleration voltage of 6 kV. The results obtained for as-grown and annealed films at 450 and 550 ^{o}C are given in Table 4.7. It shows that here is a Ga-rich and Ag-poor composition and the atomic percentage of Se is decreasing with increasing annealing temperature. The decrease in the amount of Se is a frequently encountered situation in selenium based compounds and attributed to the re-evaporation from the surface at high annealing temperatures [97-98].

Table 4.7: EDAX results obtained for as-grown and annealed $AgGaSe_2$ thin films at 450 and 550 ^{o}C at 6 kV

	Atomic Percent (at %) ±2%		
sample	Ag	Ga	Se
stoichometry	25.00	25.00	50.00
as-grown	17.99	32.07	49.93
450 ^{o}C	17.87	32.77	49.36
550 ^{o}C	22.98	35.39	41.63

For the identification the structure and phases in the deposited $AgGaSe_2$ thin

films, the XRD measurements were performed in the range of 20^o-90^o with scan rate of 2^o/min. The diffraction patterns seen in Fig.4.21 show that all films are polycrystalline.

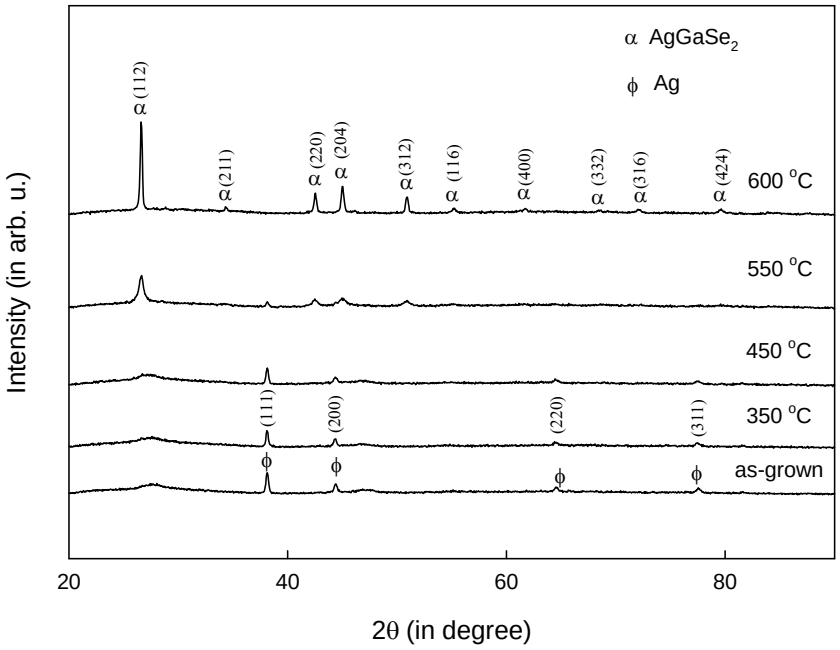

Figure 4.21: XRD patterns of as-grown and annealed $AgGaSe_2$ thin films between 350 and 600 ^oC.

Based on the analysis of the diffraction patterns, it was found that the Ag metallic phase exists in the as-grown $AgGaSe_2$ structure with the diffraction along (111), (220) and (311) directions as compared with JCPDS card [99]. It was deduced from the analysis that only Ag was phase available in the structure up to the annealing temperature of 450 ^oC. However, above 550 ^oC, the co-existence of $AgGaSe_2$ [100] and Ag was observed. Moreover, increasing annealing temperature up to 550 ^oC resulted in systematical decrease in the intensities of Ag peak and developing the $AgGaSe_2$ phase as to be the dominant phase in the structure. The annealing temperature of 550 ^oC seems to be critical value for the formation of $AgGaSe_2$ phase since below this critical value only the Ag phase developed probably stemming from the insufficient thermal energy for reaction taking place between sequentially deposited Ag and GaSe film layers. When the annealing temperature was elevated to 600 ^oC, the Ag phase disappeared completely and the structure was consisting of single phase $AgGaSe_2$. The possible reason of disappearing Ag phase at high

annealing temperature can be attributed to the growth of $AgGaSe_2$ mono-phase requiring high thermal kinetic energy for the constituent atoms. Similar observations have been reported previously by H. Matsuo et al [20] and [101]. The phase of $AgGaSe_2$ developed at 600 ^oC was found to be chalcopyrite with the preferred orientation along (112) direction and lattice parameters of a=b=5.993Å, c=10.884 Å and c/a=1.816. It is clear that the intensity of (112) reflection increases with increasing annealing temperature from 550 to 600 ^oC, thus, indicating a better crystallinity. That is, the full width at half maximum (FWHM) for the (112) is decreasing with increasing annealing temperature. Based on (112) reflection, the grain size of the films annealed at 550 and 600 ^oC were calculated using the Scherrer's formula (eqn. 2.2). It was found that the grain size increased from 49 to 72 nm with increasing annealing temperature from 550 to 600 ^oC.

The surface morphology of the deposited $AgGaSe_2$ films has been determined by SEM micrographs. Fig.4.22 shows the SEM pictures obtained for the as-grown and annealed samples between 450 and 600 ^oC. It can be clearly seen that the samples consist of grains with different shapes and diameters ranging from 0.5 μm to 2 μm and they are increasing with increasing annealing temperature. As seen from picture, the likely cause of gradual increase in grain size is closely related to the coalescence of previously formed small grains with increasing thermal energy supplied during annealing process and resulting in the better crystallinity. This is also in good agreement with the results obtained from the XRD study in terms of improvement in crystallinity. When the grain sizes obtained from both XRD and SEM measurements are compared, it is seen that there is a large difference, which is the reason of the grain sizes appeared in SEM images are the grains only at the surface of films, while grain size calculated from the XRD is the average value of the grain sizes distributed throughout the thickness of the film [20].

As it was previously mentioned that there are some structural parameters related to chalcopyrite compounds like anion displacement (μ) and distortion (x) parameters, which are determining the structural and optical properties of these compounds. By using the lattice parameters (a=5.993 Å and c=10.884 Å) the positional parameter (σ) (defining the position of C atoms with respect to A and B atoms in the chalcopyrite structure of ABC_2) and anion-cation bond length were calculated through the

equations of (1.1).

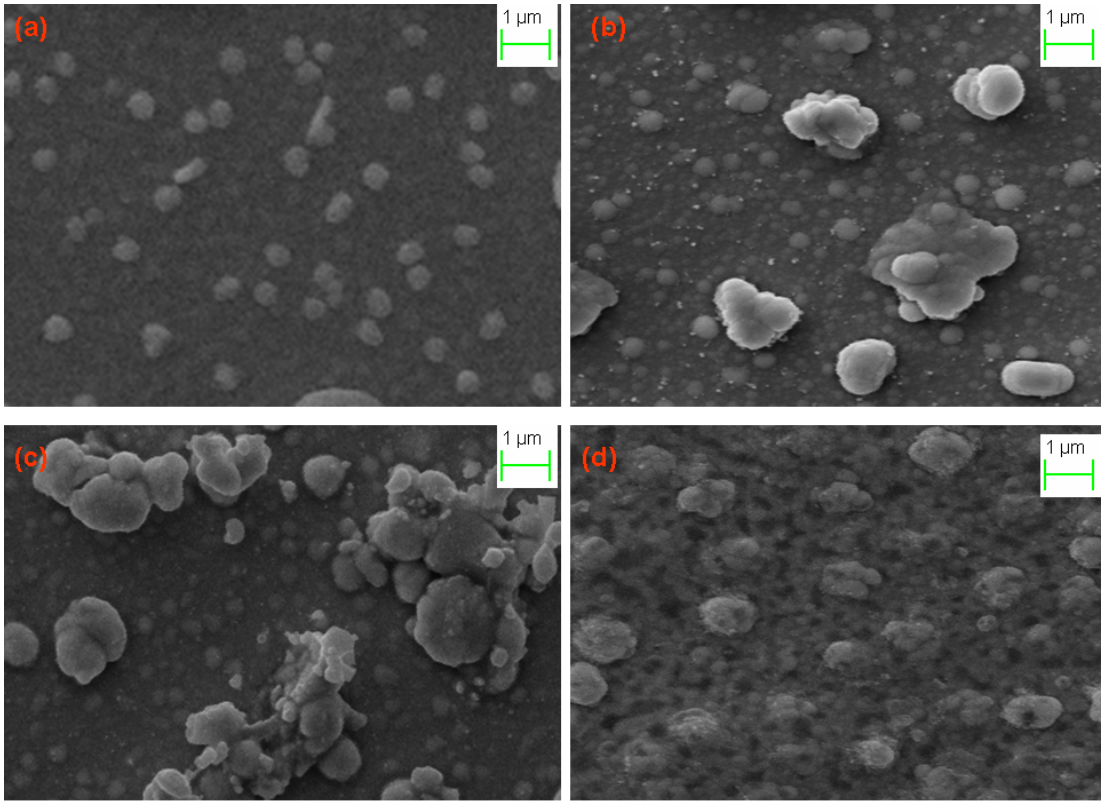

Figure 4.22: SEM pictures recorded for (a) as-grown and annealed $AgGaSe_2$ films at (b) 450 ^oC, (c) 550 ^oC, and (d) 600 ^oC.

In this equation, $R_{A\text{-}C}$, and $R_{B\text{-}C}$ are A-C (Ag-Se), and B-C (Ga-Se) bond lengths, respectively. For $AgGaSe_2$, we have found these values as 0.3, 2.7, and 2.35 Å, respectively. Then, by making use of these values, the anion displacement parameter was calculated by using equation (1.2) and found to be 0.299. This value for $AgGaSe_2$ was previously reported to be as 0.288 [102], which is almost the same value when compared in the experimental error limit. The displacement parameter values imply that the Se atoms are located away from the Ag atoms when compared with the ideal position of Se (μ=0.25) in the zinc blende structure. This results in the reduction in the hybridization between Se p and Ag d orbitals, which has an important effect on determining the band gap values of such type compounds. That also explains why the band gap of ABC_2 chalcopyrite compounds are lower approximately 0.5 eV from that of binary analogue of II-VI compounds [30].

The second anomalous parameter is the tetragonal distortion (x) and measures the deviation of ratio c/a from the accepted value of about 2. That is, the chalcopyrite unit cell is constructed by doubling the unit cell of zinc blende structure in vertical direction with lattice parameter ratio c/a, which approximately equals to two. However, the unit cell of chalcopyrite structure is tetragonaly distorted from this value which is represented by x=2-c/a [34]. We have found this value to be 0.184, which is in very well agreement with reported value for $AgGaSe_2$ [28].

4.4.2 Optical Analysis

Optical properties of $AgGaSe_2$ thin films were studied by carrying out transmittance and reflectance measurements in the wavelength range of 325-1100 nm at room temperature. Fig. 4.23 and fig. 4.24 show the variation of transmittance and reflectance with wavelength for as-grown and annealed films, respectively.

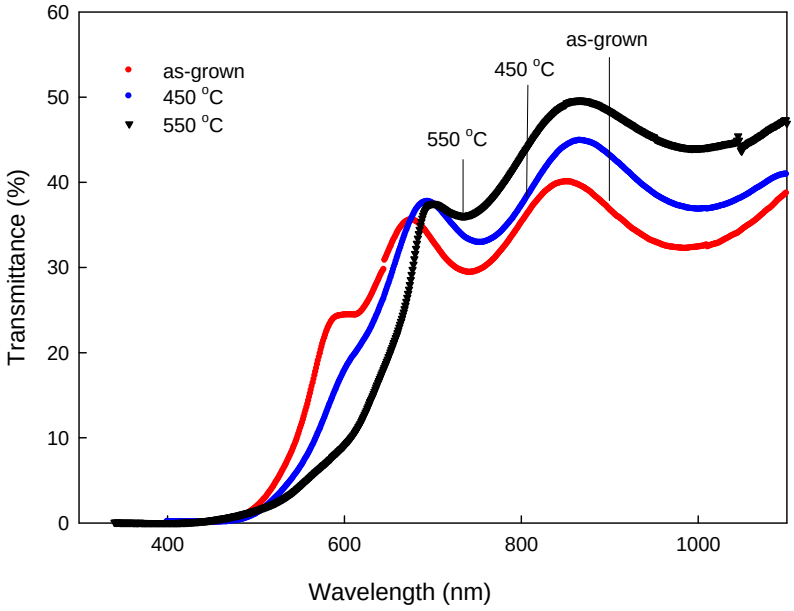

Figure 4.23: Transmittance spectra obtained for as-grown and annealed $AgGaSe_2$ films at 450 and 550 °C.

As seen from fig. 4.23, the average transmittance is over 40% for all films in infrared region and increases as the annealing temperature increases; however the reflectance is below 20% and decreases with increasing annealing temperature as accepted. The

observed variation in reflectance and transmittance may be attributed to the improvement in crystallinity, diminishing scattering centers, and better structural homogeneity following to the annealing process [103].

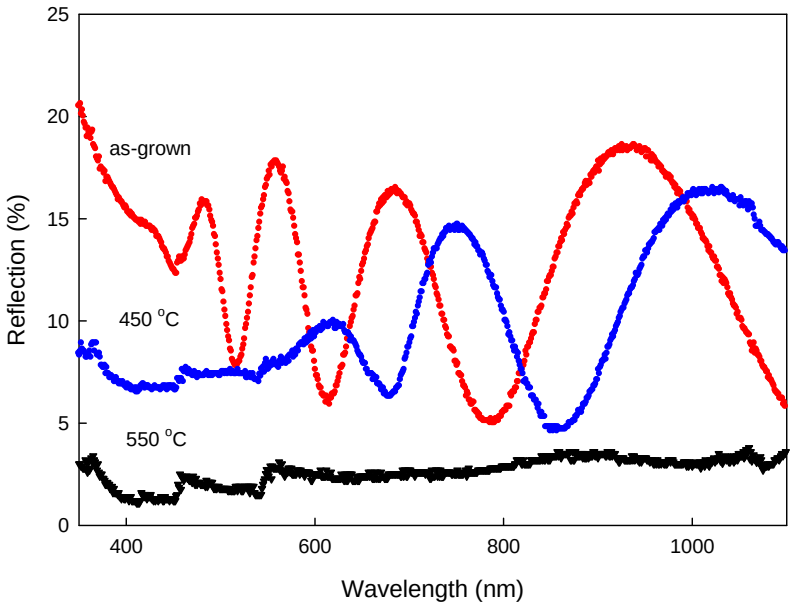

Figure 4.24: Reflectance spectra obtained for as-grown and annealed $AgGaSe_2$ films at 450 and 550 °C.

Using the transmittance and reflectance values, the absorption coefficient (α) was calculated through the eqn. (2.17).It was found that the absorption coefficient follows the relation given by eqn. (2.25). To determine the band gap energy values, the $(\alpha h\nu)^2$ versus photon energy ($h\nu$) was plotted as shown in Fig. 4.25 and Fig. 4.26 for the as-grown and the sample annealed at 550 °C, respectively. Optical band gap values for the three linear regions were calculated for as-grown and film annealed at 550 °C from the extrapolation of the linear part of curves on the energy axis, and listed in Table 4.8. The analysis of the evaluated energy values shows the general characteristic of I-III-VI_2 chalcopyrite compounds. The structure of such type of compounds is similar to the structure of II-VI materials. However, there is a difference between the chalcopyrite and zinc blende structures in terms of the existing uppermost valance band nature. The triple degeneracy in p-like Γ_{15} level in zinc blende structure is lifted and split into three levels due to the tetragonal symmetry of the crystal field and spin-orbit interaction in chalcopyrite structure as

shown in Fig. 4.27 [5, 23].

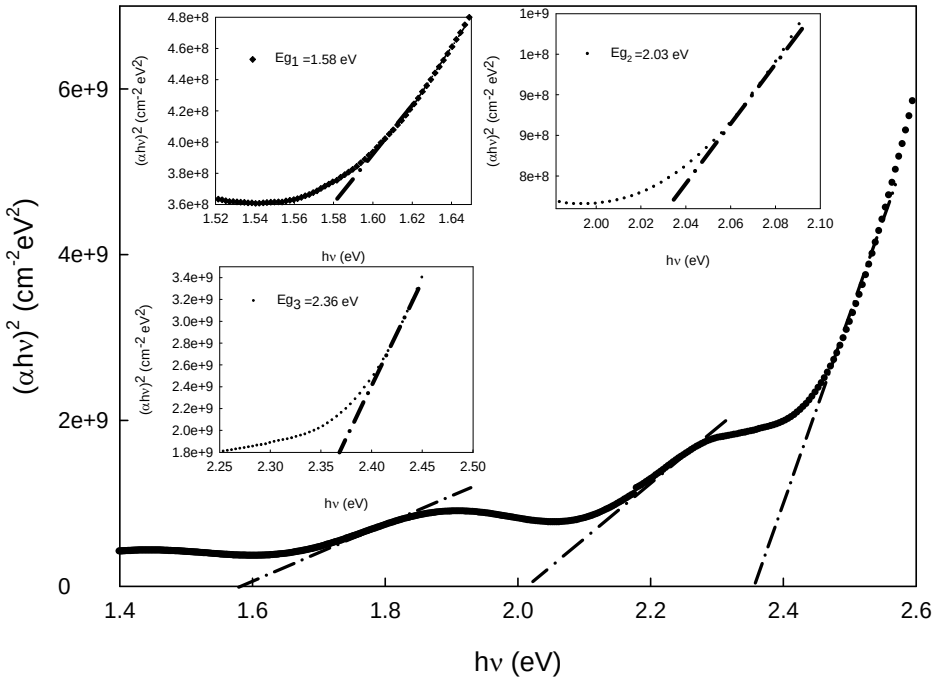

Figure 4.25: Variation of $(\alpha h\nu)^2$ versus $(h\nu)$ plot for as-grown $AgGaSe_2$ thin film.

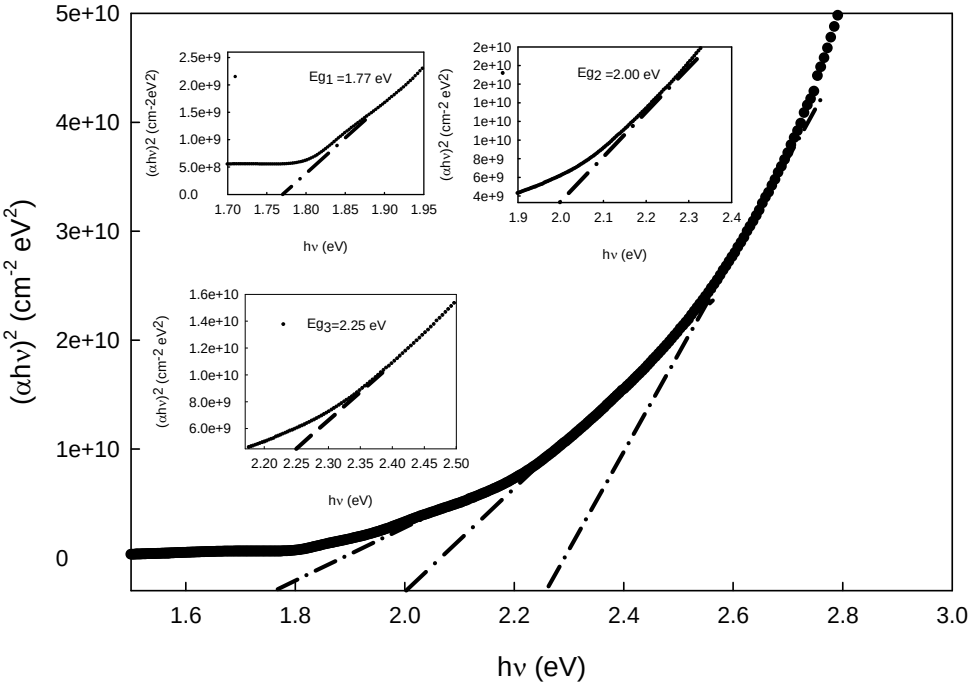

Figure 4.26: Variation of $(\alpha h\nu)^2$ versus $(h\nu)$ plot for $AgGaSe_2$ thin film annealed at 550 ^oC.

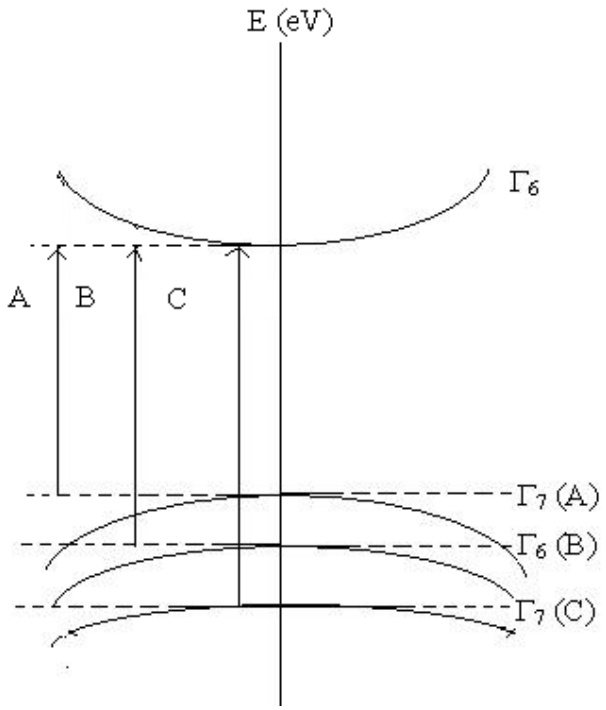

Figure 4.27**:** Band Structure of $AgGaSe_2$ for optical transitions.

Here, Γ_7(A), Γ_6(B) and Γ_7(C) transitions correspond to band to band transition, the crystal field, and the spin-orbit splitting levels to conduction band minimum, respectively. The band gap energies E_{g1}, E_{g2}, and E_{g3} found from the optical absorption for the as-grown and annealed sample at 550 ^{o}C represent A, B, and C transitions shown in Fig.4.27, respectively. Especially, these values obtained for the sample annealed at 550 ^{o}C are in a close agreement with previously reported data for $AgGaSe_2$ [23, 28, 30, 104]. Based on the quasi-cubic model, the spin-orbit (Δ_{SO}) and crystal-field (Δ_{CF}) parameters were also calculated by using the following relation [1];

$$E_{1,2} = -\frac{1}{2}\left[\Delta_{SO} + \Delta_{CF}\right] \pm \left[\left(\Delta_{SO} + \Delta_{CF}\right)^2 - \frac{8}{3}\Delta_{SO}\Delta_{CF}\right]^{1/2} \qquad (4.4)$$

Calculated values of Δ_{CF} and Δ_{SO} for the as-grown and annealed sample at 550 ^{o}C are given in Table 4.8. As compared with the reported values for $AgGaSe_2$ [23, 28, 30, 104], it was observed that there was a slight deviation from the reported values, which could be the result of the structural changes with annealing. To confirm the these transitions obtained from the optical absorption measurement, the

photoresponse measurements were carried out, since it is a strong tool for the determination of band gap energy and valance band splitting. These levels stemming from crystal-field and spin-orbit interaction were also observed from the photoresponse measurements carried out for as-grown and film annealed at 550 ^{o}C as shown in Fig. 4.28 and Fig. 4.29, respectively. Each spectrum consists of three peaks with almost the same energy values obtained from the absorption measurements.

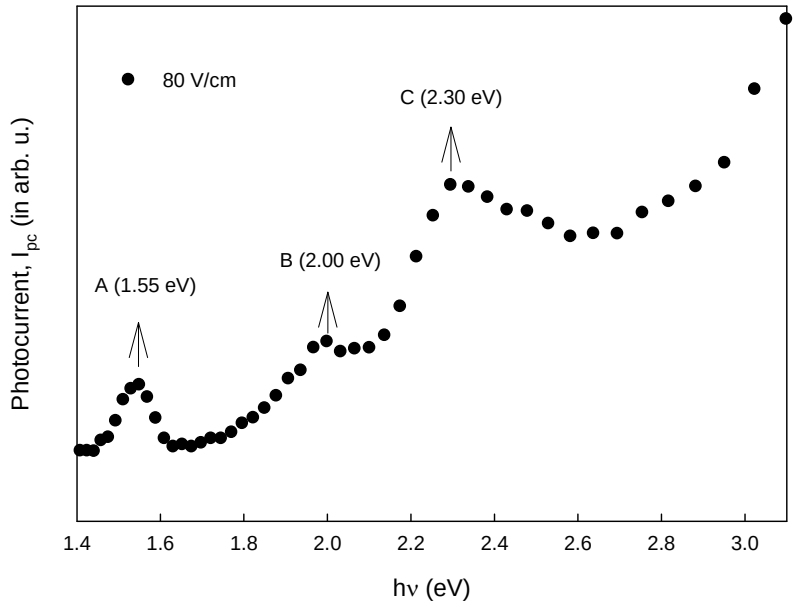

Figure 4.28: Photoresponse of as-grown $AgGaSe_2$ thin film at room temperature.

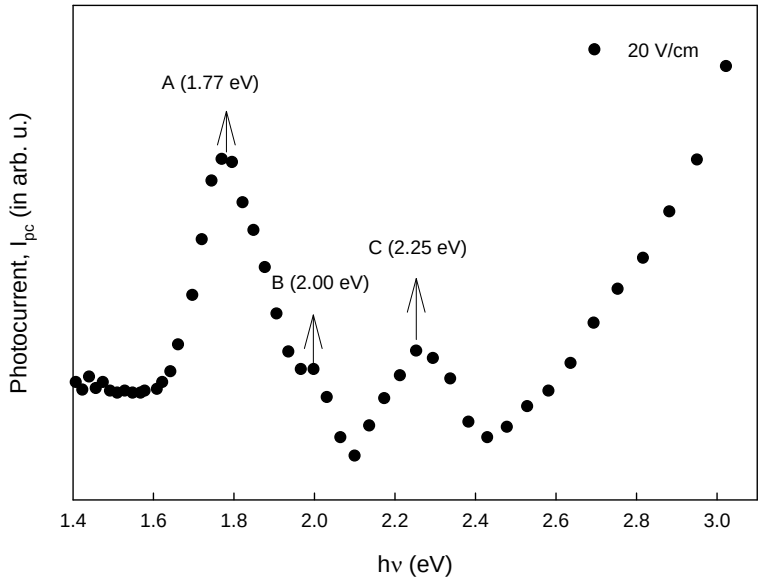

Figure 4.29: Photoresponse of $AgGaSe_2$ thin film annealed at 550 ^{o}C at room temperature.

Table 4.8: Calculated energy values of optical transitions, crystal-field and spin-orbit parameters for the as-grown and annealed $AgGaSe_2$ thin film at 550 ^oC

Sample	E_{g1} A (eV)	E_{g2} B (eV)	E_{g3} C(eV)	Δ_{SO} (eV)	Δ_{CF} (eV)
as-grown	1.58	2.03	2.36	0.42	-0.54
550 ^oC	1.77	2.00	2.25	0.30	-0.28

4.4.3 Electrical Characterization

The variation of conductivity as a function of temperature for as-grown and $AgGaSe_2$ thin films annealed at 450 and 550 ^oC is shown in Fig. 4.30.

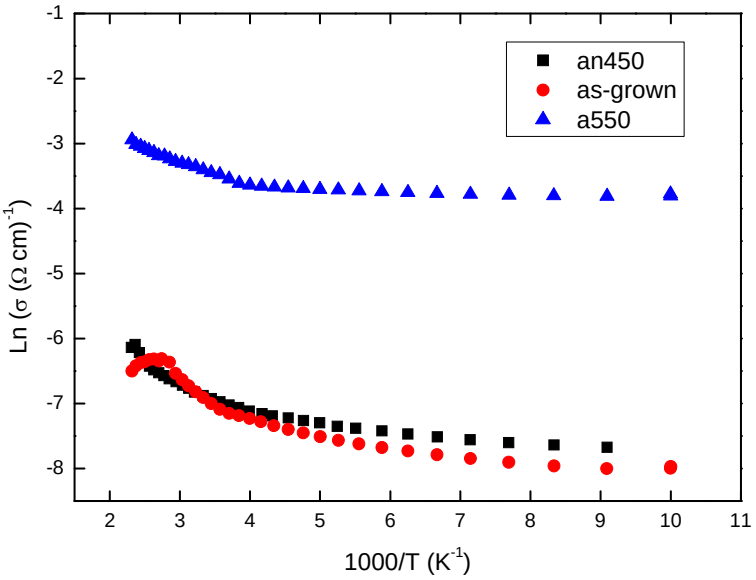

Figure 4.30: Temperature dependent electrical conductivity of as-grown and $AgGaSe_2$ thin films annealed at 450 ^oC and 550 ^oC

As can be seen from the figure, the conductivity values for all samples increase exponentially as the sample temperature increases, which can be taken as a clear indication of $AgGaSe_2$ thin film behaving as a semiconductor material. It is also seen that the conductivity shows pronounced increases when the samples is annealed

above 450 ^{o}C. The room temperature resistivity values were measured around 1000, 965, and 30 (Ω-cm) for as-grown, and the samples annealed at 450, and 550 ^{o}C, respectively. There is approximately two order decrease in resistivity after annealing at 550 ^{o}C. Previous works have shown that $AgGaSe_2$ is a semi-insulating material with resistivity value varying from $1x10^{8}$ to $3x10^{10}$ (Ω-cm) [12, 23-24]. The possible reason of obtaining $AgGaSe_2$ with a lower resistivity is the result of having different stoichiometry. This was also confirmed by a study conducted on $AgGaSe_2$ [105]. In that study, it was found that the conductivity was varying in between $1.4x10^{-6}$ and $4.9x10^{-3}$ $(\Omega\text{-cm})^{-1}$ with changing the atomic ratios of constituent elements. The temperature dependent conductivity reveals two distinct regions with different activation energies for as-grown and annealed samples as listed in Table 4.9.

Table 4.9: Calculated activation energies for as-grown and annealed $AgGaSe_2$ thin films at 450 and 550 ^{o}C

sample	E_1 (meV) (in (110-230) ± 20K)	E_2 (meV) (in (250-390) ± 20K)
as-grown	12	65
450 ^{o}C	9	45
550 ^{o}C	5	34

It implies that there are different conduction mechanisms dominating at different temperature region. Cation (Ag, Ga) and anion (Se) vacancies and interstitials (or cation-cation antisite disorder point defects) may cause formation of different defect levels in undoped chalcopyrite compounds. Calculated activation energies for some donor levels of $AgGaSe_2$ were reported to be varying from 20 to 210 meV [106]. They could be attributed to the native point defects, especially the Se-vacancies due to their low formation energies in n-type $AgGaSe_2$. The observed fluctuation in atomic percentage of constituent elements following to the post-annealing may promote the formation of these defects.

The measured conductivity found to be following the Arrhenius relation given in

eqn. (4.3). As can be seen from the table, the activation energies for two linear region of each sample decreases as annealing temperature increases. The lowering activation energy is closely related to the observed decrease in resistivity after post-annealing process since it results in generation of more free carriers compared with as-grown film at the same temperatures. Of course, the free carriers are not the only parameters determining the resistivity. Thus, the other parameters influencing the resistivity should also be determined. It is known that the conductivity is expressed in terms of mobility (μ) and free charge carrier concentration (n) related by $\sigma = nq\mu$ expression. Here, n is the free electron concentration since the $AgGaSe_2$ thin films were found to be conducting as n-type confirmed by both hot-probe and Hall effect measurements. It is known that the origin of n-type conduction in chalcopyrite compounds is the anion vacancies (V_{Se}) [24]. Similar conduction type for Ag-poor and Ga-rich $AgGaSe_2$ was reported by Matsuo et al. [20] .To understand the effect of mobility and free carrier concentration on determining conductivity, Hall measurements were performed for the as-grown and samples annealed at 450, and 550 ^{o}C in the temperature range of 100-370 K. The carrier concentration (n) of the film was evaluated through the $n=1/qR_H$ relation, where R_H and q are Hall coefficient and electron charge, respectively. The temperature dependent carrier concentrations for the as-grown and annealed sample at 450 and 550 ^{o}C are shown in Fig. 4.31. It has been observed that the carrier concentration stays almost constant in between ~100 and 330 K (with ± 20 K deviation) and increases with increasing temperature at high temperature above 330 K. The room temperature carrier concentration calculated to be $9.6x10^{14}$, $1.7x10^{15}$ and $6.6x10^{16}$ cm^{-3} for as-grown, the films annealed at 450 and 550 ^{o}C, respectively. That's the free carrier concentration increases as the annealing temperature increases, which is probably related to the lowering activation energies following to the annealing process promoting the generation of free carriers.

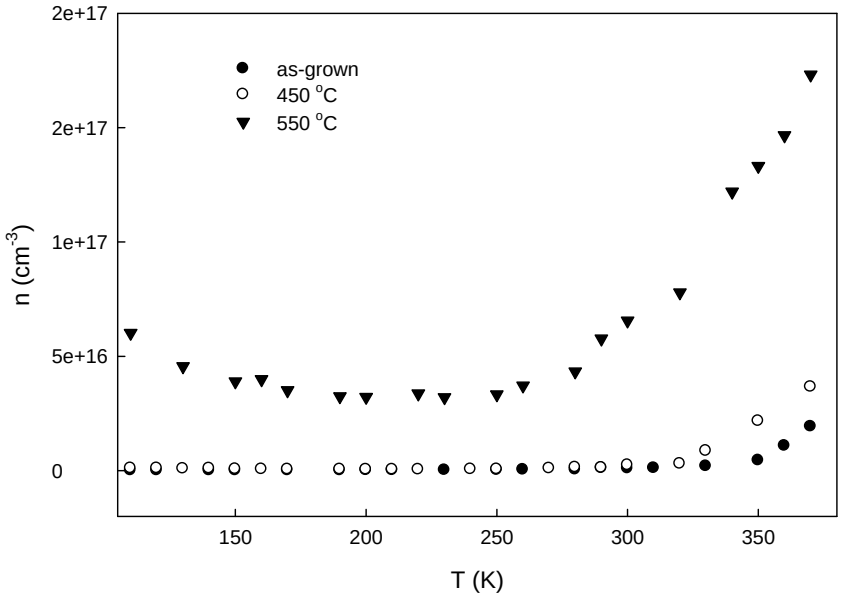

Figure 4.31: Variation of carrier concentration (n) as a function of temperature for as-grown and annealed $AgGaSe_2$ thin films at 450 and 550 °C.

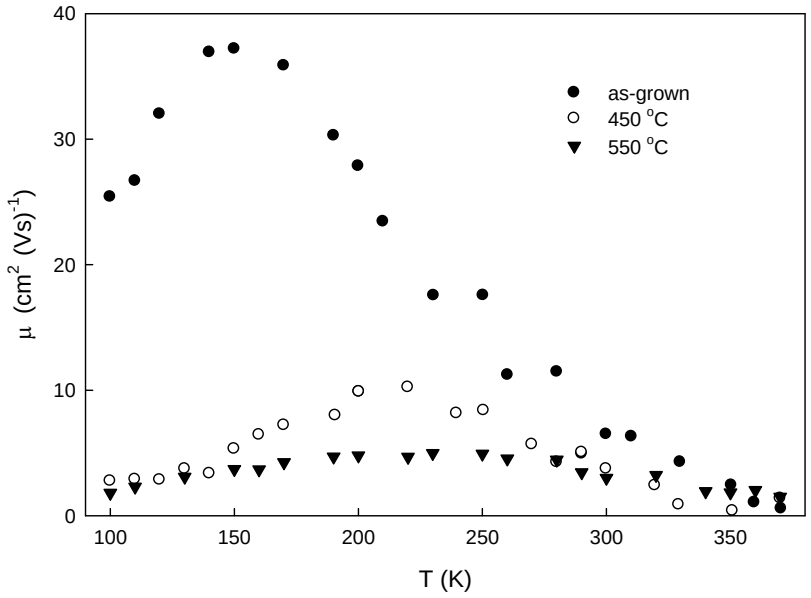

Figure 4.32: Variation of mobility (μ) as a function of temperature for as-grown and annealed $AgGaSe_2$ thin films at 450 and 550 °C.

The mobility of the $AgGaSe_2$ thin film was calculated using the $\mu=\sigma R_H$ relation. The temperature dependent mobilities of the as-grown and the samples annealed at 450 and 550 °C are shown in Fig.4.32. The room temperature mobility

values were found to be as 6.4, 3.7, and 3 cm^2 $(V.s)^{-1}$ for as-grown and the films annealed at 450 and 550 ^oC, respectively. They are in good agreement with the reported values of $AgGaSe_2$ deposited with the different Ag/Ga ratios [105]. As seen from the figure, the mobility decreases with the increasing annealing temperature. It was observed that the mobility increases up to a critical temperature value and then starts to decrease with the increasing sample temperature. To understand the observed behaviour of mobility at different temperature intervals and to determine the scattering mechanisms, the Log (μ) versus Log (T) was plotted for as-grown and annealed $AgGaSe_2$ thin films in Fig. 4.33. The slope of each linear region was calculated, which gives the exponent of $\mu \alpha T^{\pm\beta}$ relation that determines the dominant scattering mechanisms in the studied temperature region. The calculated exponent values in the specific temperature intervals for as-grown and annealed $AgGaSe_2$ thin films are given in Table 4.10.

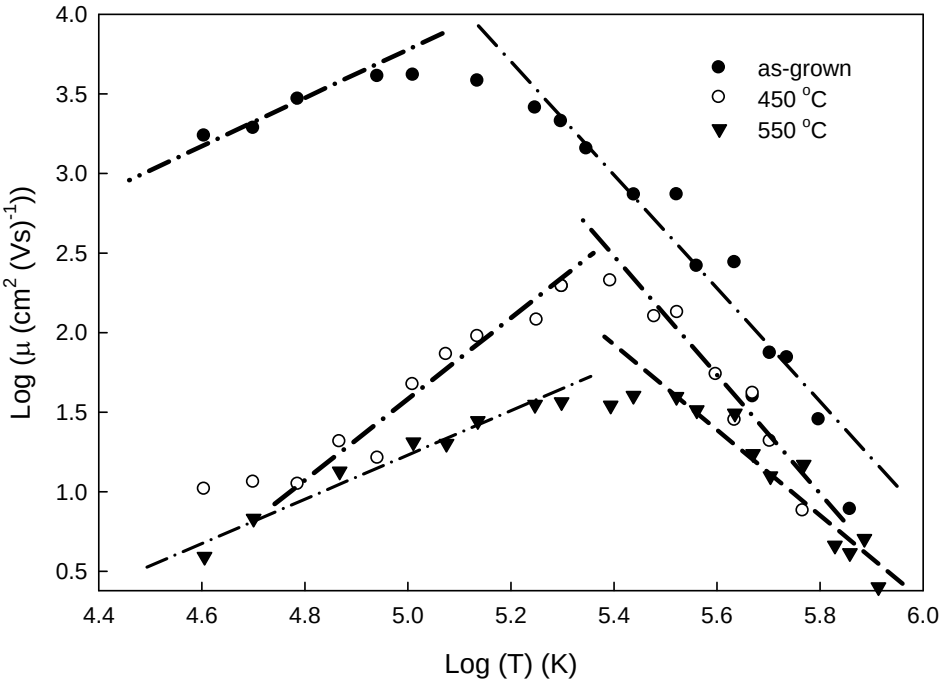

Figure 4.33: Log (μ) vs Log (T) relation for as-grown and annealed $AgGaSe_2$ thin films at 450 and 550 ^oC

Table 4.10: Calculated exponents in low and high temperature regions for as-grown and annealed $AgGaSe_2$ thin films at 450 and 550 ^oC

Sample	β	Low Temp. Reg. (K)	β	High Temp. Reg. (K)
as-grown	+1.0	(100-150)	-3.6	(170-370)
450 ^oC	+2.4	(120-200)	-3.7	(230-370)
550 ^oC	+1.4	(100-200)	-3.2	(230-370)

The variation of mobility according to the law of $\mu\alpha T^{+\beta}$ is a characteristic of scattering mechanisms of free carriers [81]. Thus, the observed steady increase in mobility with increasing temperature at low temperature interval for all samples could be attributed to the scatterings of the carriers with the ionized states. On the contrary, there is $\mu\alpha T^{-\beta}$ variation at high temperature region for all samples. The decrease in mobility with increasing temperature in this region can be explained by phonon scattering starting to dominate at high temperatures [81]. In addition, the value of $\beta=3/2$ for the power index is explained by the scattering of majority carriers (electrons) on the acoustic lattice phonons. In our case, the calculated power exponents ((-3.6), (-3.7), and (-3.2) for as-grown and the films annealed at 450 and 550 ^oC, respectively) for the mobility-temperature dependence are larger than 3/2 imposing that acoustic phonons would not be sufficient to explain the variation observed in mobility. The transition from domination by one type to the other depends on the material and its impurity nature and concentration. Deviation from "3/2" could be related with complex band structures as well as optical phonon scattering. In general, the temperature dependence of the mobility of a crystalline semiconductor can be expressed as $\mu \sim T^{\alpha+\gamma/2}$ where α and γ are constants whose magnitudes and signs are the indication of the dominant scattering mechanism [107].Similar results have been reported for the $CuInTe_2$ thin films [108] and this behaviour was explained by the contribution coming from the polar and non-polar optical interactions. Consequently, in our case the effect of interaction of electrons

with acoustic, polar and non-polar phonons could be responsible for having exponent values larger than 3/2.

4.5 Characterization of Ag-Ga-S Thin Films Deposited by Thermal Evaporation

In this part of study, our aim was to improve the electrical and optical properties of $AgGaS_2$ by studying the Ag-Ga-S system produced by a sequentially evaporation of $AgGaS_2$ and Ag films in a specific proportion by a double source thermal evaporation method. The Ag-Ga-S system contains several forms of compounds like $AgGaS_2$, $AgGa_5S_8$, $AgGa_3S_5$, and Ag_9GaS_6. To the best of our knowledge there is no any study on Ag-Ga-S system. So, herein, the effect of annealing on the structural, electrical, and optical properties of Ag-Ga-S thin films deposited by thermal evaporation were investigated.

Thin films of compound with Ag-Ga-S (AGS) system were prepared using double sources onto the soda-lime glass substrates kept constant around 200 ^oC during the deposition cycle. Prior to the sequential evaporation of Ag and $AgGaS_2$ films, the optimization of individual layers was carried out independently by conducting several depositions under the same conditions. The individual precursors of $AgGaS_2$ and Ag were deposited sequentially on substrates in order of $AgGaS_2$/Ag/$AgGaS_2$ layers with thickness of approximately 900/(50-60)/900 nm, respectively. The deposition of the layers in the given sequence was repeated until the reproducibility of films was managed. Then, to examine the effect of annealing on properties of films, the samples were annealed in the temperature range of 350-550 ^oC for a period of 5 minutes in nitrogen (N_2) flow.

4.5.1 X-ray Diffraction (XRD) and Compositional Analysis

XRD measurements have been performed to identify the structural properties of the source material (powder) and deposited Ag-Ga-S thin films. To determine the effect

of annealing on the film structure, measurements were carried out for the samples annealed in N_2 atmosphere at the temperatures ranging from 300 to 550 ^oC for 5 minute. Fig.4.34 shows the diffraction patterns for the single crystalline powder $AgGaS_2$ used as the evaporation source. It is clear from the pattern that the sintered powder has single crystalline structure and there is no diffraction peaks corresponding to any precipitation of secondary phases. Comparing with JCPD card [109], it is deduced that this phase is corresponding to $AgGaS_2$ with chalcopyrite structure well oriented in (112) direction. The lattice constants *a* and *c* are 5.754 and 10.301 Å, respectively. Fig.4.35 shows XRD patterns of as-grown and annealed films in the temperature range of 350-550 ^oC.

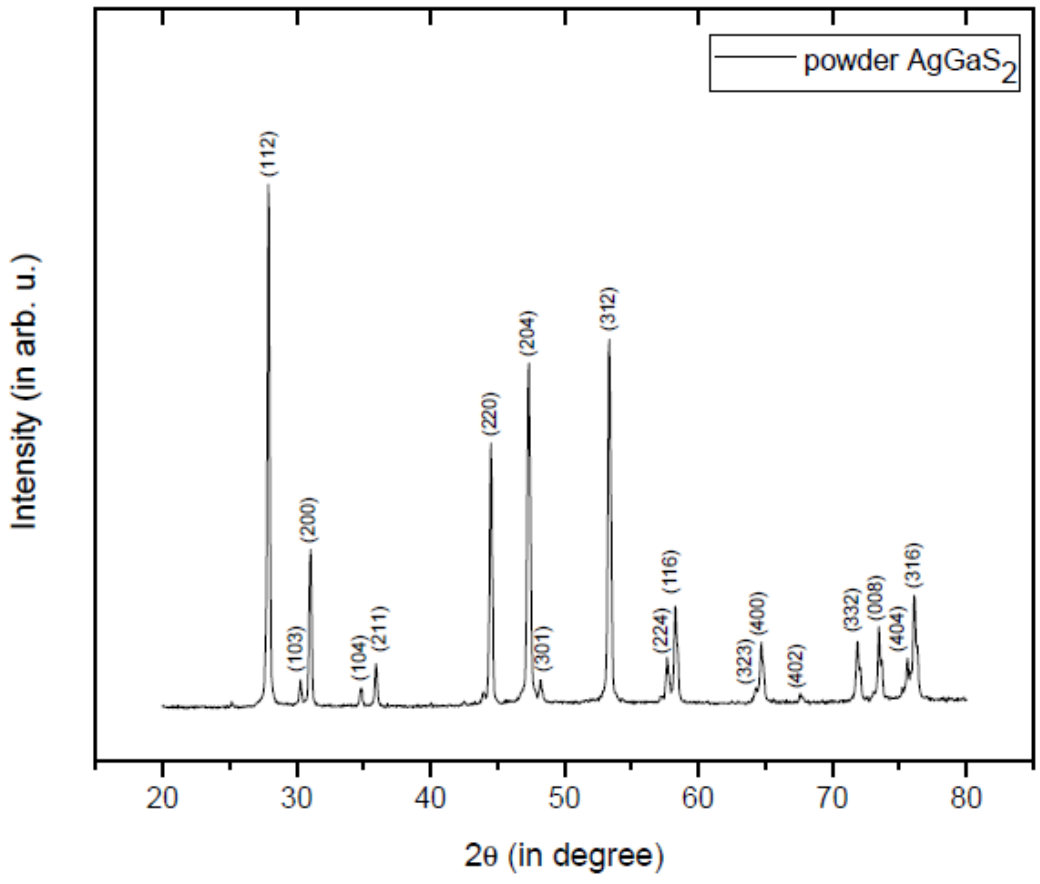

Figure 4.34: X-ray diffraction pattern for the powder used as the evaporation source.

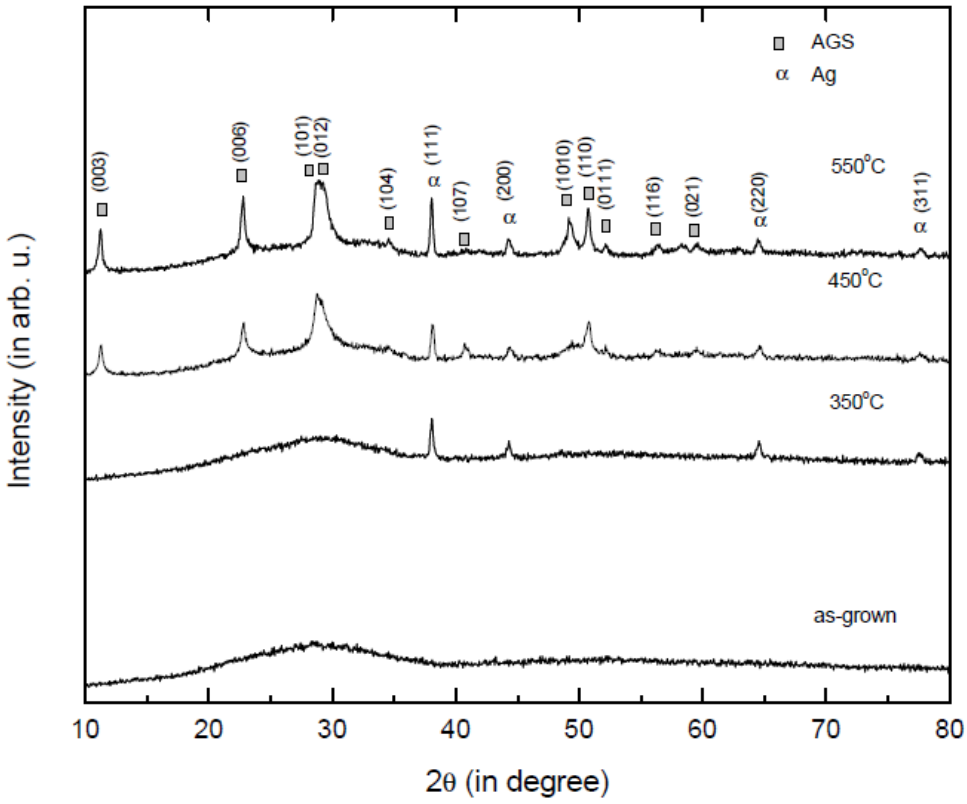

Figure 4.35: X-ray diffraction patterns of as-grown and AGS thin film annealed in the temperature range of 350-550 ^{o}C.

As seen from Fig. 4.31, the as-grown film is in amorphous structure. Annealing the samples at 350 ^{o}C, Ag crystallites were observed. Namely, the observed peak positions coincide with those of the (111), (200), (220) and (311) reflections of Ag having cubic structure [99]. Up to the annealing temperature of 400 ^{o}C, there is no remarkable variation in terms of improvement in the structure. However, above 400 ^{o}C annealing temperature the (Ag,Ga)S (AGS) develops with co-existence of Ag phase. Comparing with JCPD cards, it is revealed that AGS is a ternary compound with hexagonal structure (a=b=3.587, and c=23.200 Å) [110]. All appeared reflecting planes with corresponding Miller indices (h, k, l) for the AGS were illustrated in Fig. 4.35. From the pattern, it is seen that the predominant (101) peak of hexagonal system exhibiting a preferred orientation along this plane. With further increase in annealing temperature (550 ^{o}C), it is seen that the intensity of reflection lines of both AGS and Ag phases are increasing, which is the indication of the better crystalline quality. As observed from SEM images (in Fig. 4.36) of as-grown and annealed film

at 550 ^{o}C, the increasing grain sizes with the annealing could also confirm the improvement in crystallinity. Hence, annealing the films give thermal energy to the adsorbed atoms to complete the nucleation process. High mobile ad-atoms have a large diffusion distance which promotes the probability of collision process and triggers the nucleation resulting in growing a film with larger grains [111]. The structure of the film annealed at 550 ^{o}C is dominated by AGS with the preferred orientation along (101) direction corresponding to Bragg's angle 2θ=28.97.

The compositional analysis has been performed by EDXA measurements. A typical spectrum for the powder $AgGaS_2$ is shown in Fig. 4.37. Results have revealed that the ratio of the constituent elements Ag:Ga:S in the powder and as-grown film is nearly 1:1:2 (23.72:27.81:48.47 %) and 1:5:8 (7:35.86:57.14 %), respectively. This implies that the stoichiometry of unknown (Ag,Ga)S in JCPDS database is likely to be $AgGa_5S_8$. There is no any study reported for $AgGa_5S_8$ structure so far. It is clear from the XRD pattern of film annealed at 550 ^{o}C that the elemental Ag diffraction peaks exist in the structure and their intensities are increasing. The SEM pictures (Fig. 4.38) obtained for the as-grown and films annealed at 550 ^{o}C also confirm the evolution of silver phase. These micrographs were recorded with the same parameters (the same spot size, working distance (WD) and acceleration voltage). It is seen that the agglomerations are distributed irregularly and their densities over the surface are increasing with post-annealing. The EDXA measurements for the regions embody high density of these geometric shapes have revealed that the atomic percent of constituent elements Ag, Ga, and S is 79.50, 13.19, and 07.30, respectively. High atomic percent of Ag implies that these features with different geometries and sizes are corresponding Ag crystallites probably improved by the crystallization of mobile Ag atoms diffused out from the grain boundaries to the surface by the subsequent post annealing at high temperatures. In addition, it is likely to be due to the diffusing of Ag atoms from the deposited Ag-layer to the surface through the voids formed during the segregation of high volatile S triggered at high annealing temperatures. The most probable reason of not developing single phase in the structure is insufficient thermal energy driven by annealing to complete the reaction between the sequentially deposited $AgGaS_2$/Ag/$AgGaS_2$ film layers.

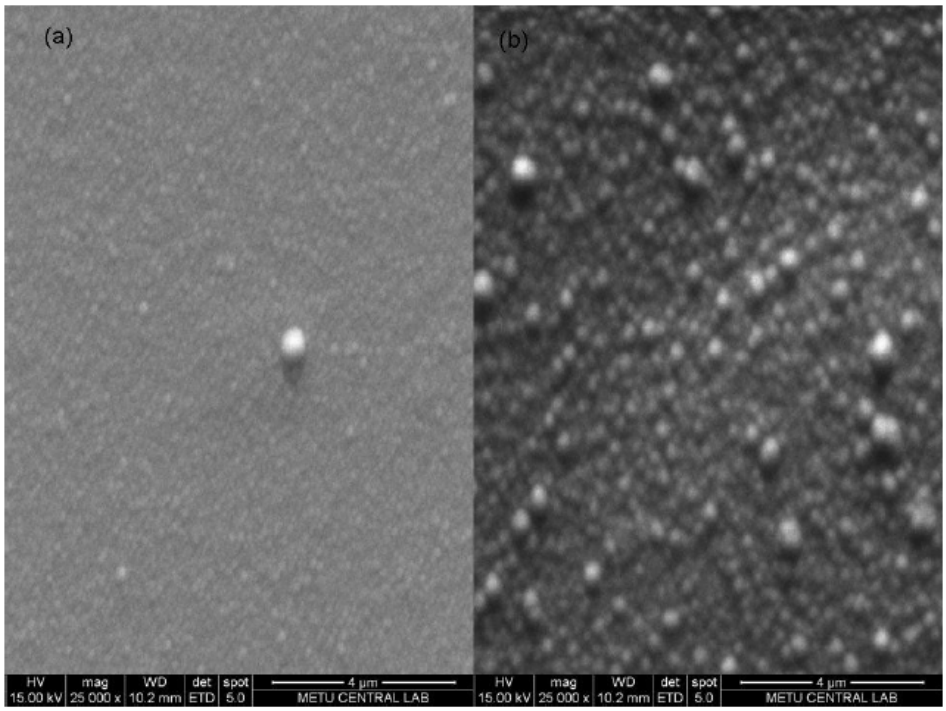

Figure 4.36: SEM micrographs for (a) as-grown and (b) AGS films annealed at 550 ^{o}C.

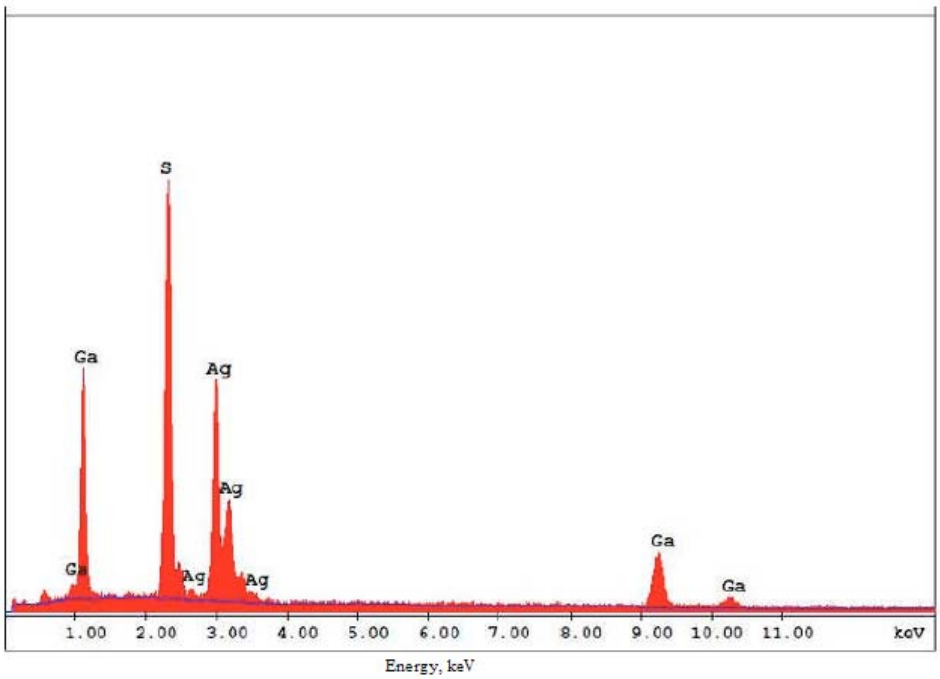

Figure 4.37: EDXA spectrum for the source-powder $AgGaS_2$ conducted at 20 kV.

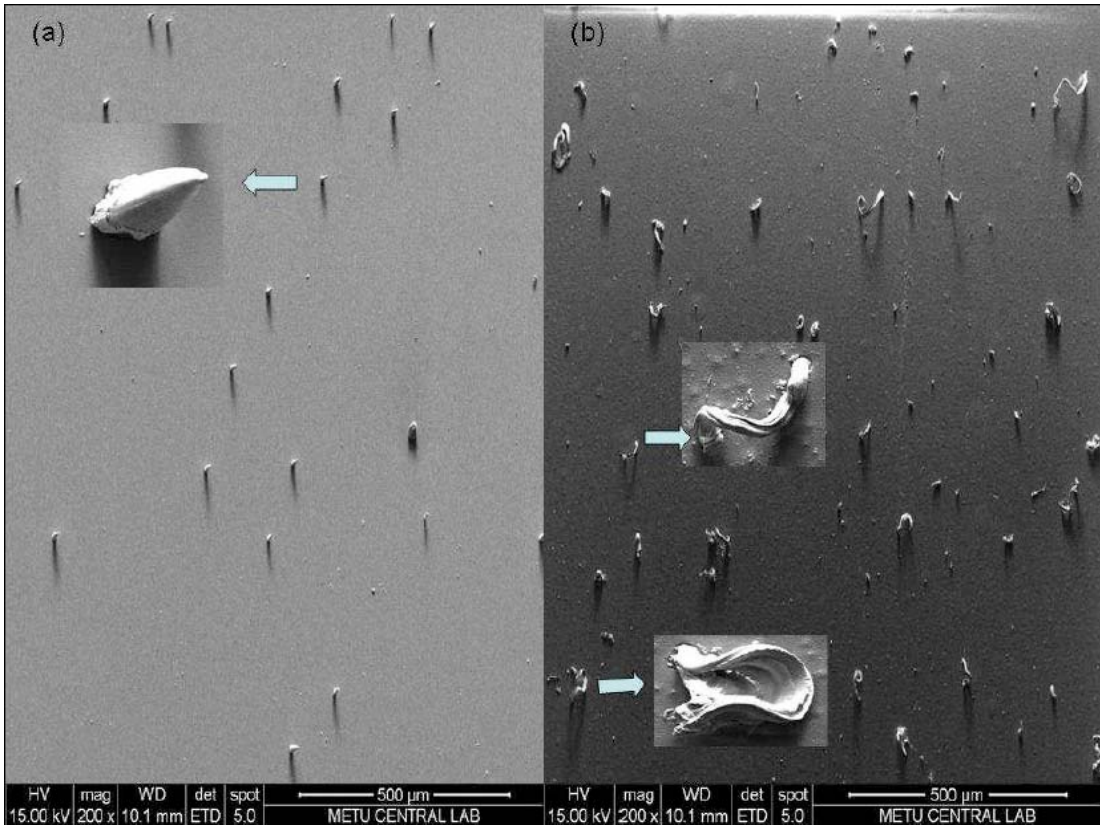

Figure 4.38: SEM pictures indicating the evolution of Ag agglomerations obtained for (a) as-grown and (b) AGS thin films annealed at 550 ^{o}C.

Because of that, to increase the probability of interaction of Ag-crystallites to complete the formation of AGS nucleations, the mobility of silver atoms should be increased by raising annealing temperature. But, for the films deposited on soda-lime glass substrates it is not feasible to increase the annealing temperature over 550 ^{o}C due to the melting point of glass substrate.

4.5.2 Optical Analysis

Fig. 4.39 shows the transmittance spectrum measured in the range of 325 to 900 nm for the as-grown and films annealed at 350 and 550 ^{o}C. As clearly seen from the figure, there is a variation in transmission and absorption edge with increasing annealing temperature.

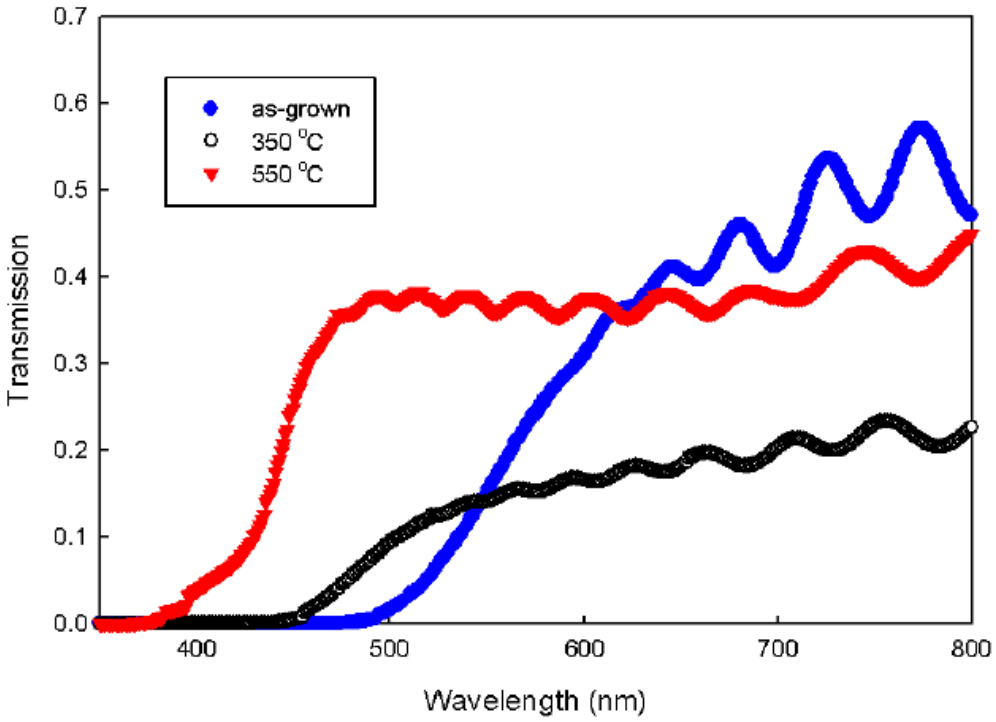

Figure 4.39: Transmittance spectrum for the as-grown, and films annealed at 350 and 550 °C

It seems that the average transmittance increases from 20 % to 38% as annealing temperature increased from 350 to 550 °C. The enhancement in transparency with the increase of annealing temperature could be attributed to the modifications in the structure and surface morphology of the films following to the annealing. It is well-known that a smoother surface causes less surface scattering of light. The observed Ag agglomerations on the surface of the films and precipitation or nucleation of silver atoms firstly in the amorphous and then polycrystalline structure may be treated as the scattering centers responsible for the dispersion of incoming photons and result in the variation of absolute value of the transparency with the annealing as seen in the figure. The silver related formations on the surface may act as the surface optical centers since they make a more roughened surface, whereas unreacted constituent elements related formations and precipitations, act as bulk scatterings. Thereby, the observed fluctuation in transmittance could be related with the formation (or elimination) of the surface and bulk scatterings at different annealing temperatures. As it was deduced from the XRD analysis, the crystallinity of the samples was improving with increasing annealing temperature. This can be the

indication of decreasing bulk scatterings. On the other hand, from the SEM pictures, it was understood that the density of surface scatterings increases with increasing of annealing temperature. Thus, the higher transmittance observed at high annealing temperature could be attributed to the decreasing of scattering centers such as the improvement of structural homogeneity and better crystallinity.

The absorption coefficient (α) of the films was obtained by means of transmittance (T) measurement through the following relation given in eqn. (2.18). The reflection measurements were also carried out for the AGS films and it was found that there are low reflection values (lower than 10 %). Thus, it was not taken into account during the calculation of absorption coefficient. Fig. 4.40 shows the plot of absorption coefficient as a function of photon energy ($h\nu$) for the as-grown, and the films annealed at 350 and 550 ^{o}C. For all samples it is found that the absorption coefficient above the fundamental band edge is around 10^4 cm^{-1}, which is a characteristic value for the I-III-VI semiconductors. Dependence of absorption coefficient on photon energy follows an allowed direct interband transition given by eqn. (2.25). The optical band gap energies were calculated from the plot of $(\alpha h\nu)^2$ vs $(h\nu)$ by extrapolating the linear region of the plot to energy axis of $(\alpha h\nu)^2=0$. The direct band gaps increase with increasing annealing temperature and the absorption edges shift to smaller wavelength (blue-shift). The band gap energy values are found as 2.30, 2.48, and 2.75 eV for the as-grown, and films annealed at 350 and 550 ^{o}C, respectively. It is well-known that the presence of unsaturated bonds and deviation from the stoichiometry results in the formation of localized states in the forbidden band gap. Since the as-grown samples are amorphous in nature and becoming crystalline by subsequent heat treatment, the increase in band gap likely to be stemming from the reduction of defects and decrease of structural disorder. The band gap value 2.75 eV obtained for the sample annealed at 550 ^{o}C agrees well with the reported value of 2.76 eV [112].

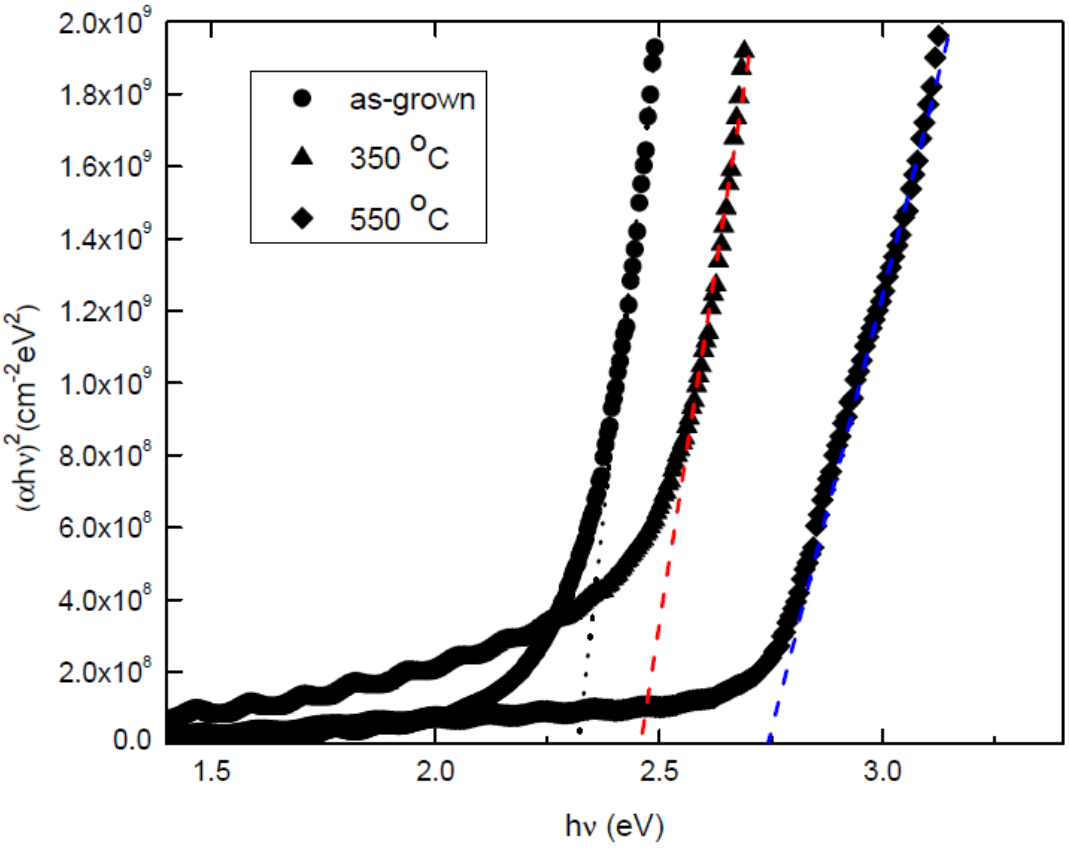

Figure 4.40: Plot of $(\alpha h\nu)^2$ against $(h\nu)$ for as-grown and AGS thin films annealed at 350 °C and 550 °C.

The optical constants (refractive index (n) and extinction coefficient (k)) of the AGS films were determined by the envelope method [113]. For the weak absorption regions, the refractive index can be determined by means of the following expression,

$$n=[N+(N^2-n_o^2n_s^2)^{1/2}]^{1/2} \quad (4.5)$$

where n_s is the refractive index of substrate (soda-lime glass), n_o is the refractive index of air which is equal to 1 and N is defined by

$$N = \frac{\left(n_o^{\,2} + n_s^{\,2}\right)}{2} + 2n_o n_s \frac{(T_M - T_m)}{T_M T_m} \quad (4.6)$$

where T_M and T_m stand for the maxima and subsequent minima of the transmission

spectra connected by the fitted envelopes illustrated as in Fig. 4.41. Fig. 4.42 and 4.43 shows the spectral distribution of *n* and *k* for the as-grown, and the films annealed at 350 and 550 ^{o}C, respectively. Constants are determined in the wavelength range of 480-680 nm and 350-860 nm for the *n* and *k*, respectively. From the spectral distribution of refractive index, it is deduced that there is a sharp decrease in the refractive index with increasing wavelength up to a specific wavelength, and then start to increase with increasing wavelength over this wavelength for the as-grown and film annealed at 350 ^{o}C. The decrease in refractive index with increasing wavelength implies that material shows usual dispersion behaviour. For the film annealed at 550 ^{o}C, the refractive index is almost wavelength independent in the studied wavelength range. As a result of the spectral distribution of refractive index, it can be concluded that the annealing process has a pronounced effect on the optical properties of these thin films. This variation is closely related to the modification taking place in the structure and optical absorption following to the annealing at different temperatures. The obtained refractive index values for the as-grown and annealed films are given in Table 4.11. The reported refractive index value for the $AgGaS_2$ in the 500-700 nm range is between 2.5 and 2.6 [114], which is larger than obtained nearly for all values for as-grown and annealed films at 550 ^{o}C, and very close to that obtained for the film annealed at 350 ^{o}C for the whole scanning wavelength range. Different structure and stoichiometry of $AgGaS_2$ (tetragonal) and $AgGa_5S_8$ (hexagonal) makes this difference plausible. The extinction coefficient values are estimated from the absorption coefficient through $k=\alpha\lambda/4\pi$ relation. Fig. 4.43 shows the spectral variation of *k* for the as-grown, and films annealed at 350 ^{o}C and 550 ^{o}C. It is clear that there is a trend of decreasing in the extinction coefficient with increasing annealing temperature, which shows that films are becoming highly transparent at long wavelengths. For the annealed samples, the *k* values are smaller than that of as-grown film for the 350-550 nm wavelength range. However, these values stay above the value of as-grown film over this range. It is well-known that extinction coefficient is a measure of absorption coefficient of a material.

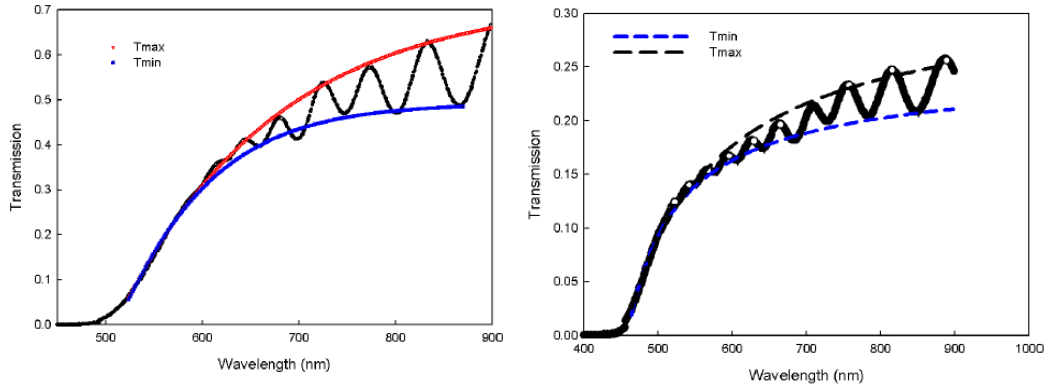

(a) (b)

Figure 4.41: The envelope fittings of T_{max} and T_{min} for the (a) as-grown and (b) AGS thin film annealed at 350 ^{o}C.

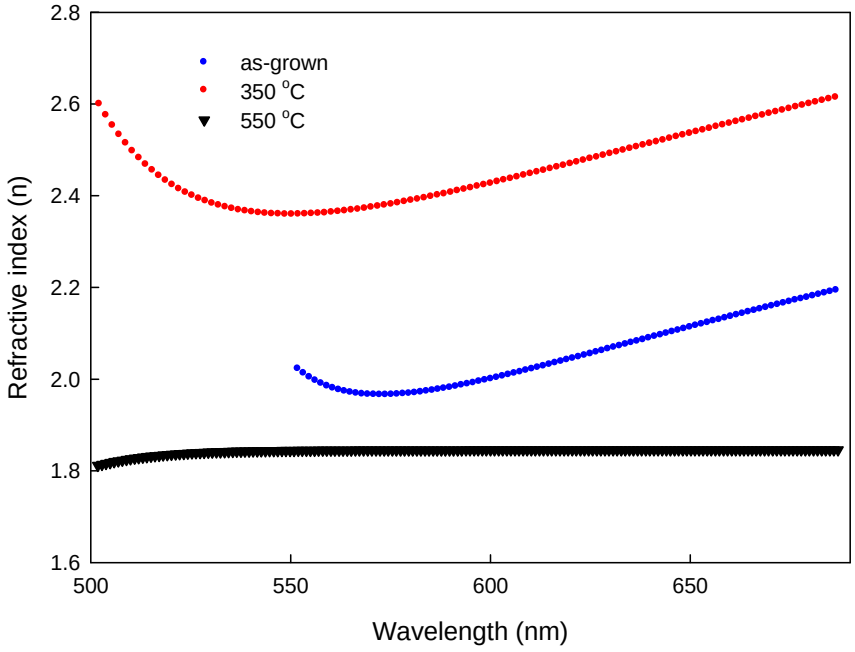

Figure 4.42: Spectral distribution of refractive index for the AGS thin films.

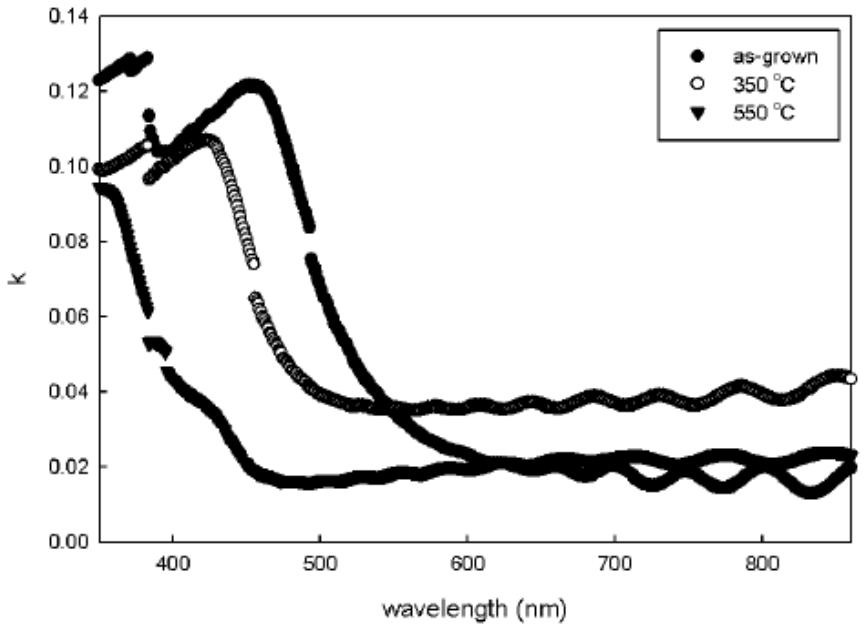

Figure 4.43: Spectral distribution of extinction coefficient (*k*) for the AGS thin films.

Table 4.11: Calculated refractive index values for as-grown and AGS samples annealed in the temperature range of 35-550 ^{o}C

Sample	wavelength range (nm)	n
As-grown	530-680	2.0-2.2
350 ^{o}C	490-680	2.4-2.6
550 ^{o}C	500-680	~1.8

As can be seen from the Fig. 4.39, the transmittance enhances (absorption decreases) with increasing annealing temperature. This suggests that the increase in the transparency is likely to be originating from the decrease observed in *k* with increasing annealing temperature in the same wavelength range. The optical constants are closely related to the density of defects in a structure. Thereby, the elimination or formation of such type defects with annealing may have pronounced effects on the optical properties.

4.5.3 Photo-Electrical Analysis

The temperature dependence of dark and illuminated conductivity under the illumination intensity of 17, 34, 55, 81, 113mW/cm^2 is shown in Fig. 4.44. The photoconductivity (PC) was evaluated by subtracting the illuminated conductivity from the dark conductivity. The variation of photoconductivity as a function of inverse temperature for the illumination intensity of 55, 81, and 113 mW/cm^2 is indicated as an inset in Fig. 4.44. It is seen that the conductivity under illumination for all intensity is larger than dark conductivity and there is an exponential increase in the conductivity with increasing ambient temperature and illumination intensity. The variation of conductivity under light could be divided into two regions: low and high temperature regions. In the low temperature region (150-260 K), the conductivity values for all illumination intensities are almost temperature insensitive. However, in the high temperature region, there is a sharp exponential increase with increasing temperature. As observed from the variation of the photoconductivity as a function of temperature in Fig. 4.44, there are three different temperature regions. In the first region (150-300 K), the PC slightly decreases with increasing temperature and increasing with increasing illumination intensity. In the second region (310-370 K), the PC exponentially increases with increasing temperature for each illumination intensity of 55, 81, 113 mW/cm^2 with activation energies of 264, 340, and 350 meV, respectively. Existence of these regions with different activation energies indicates the presence of different trap levels. The increase in activation energy with increasing illumination intensity implies that the Fermi level in the as-grown film is changed due to the increasing density of the defect centers [115]. Finally, in the third region, over 380 K the photoconductivity decreases with increasing temperature for all intensities. This phenomenon is known as the thermal quenching of photoconductivity [69]. Such a behaviour is generally attributed to the co-existence of the sensitizing and recombination centers in the structure [115]. To investigate the nature of recombination centers, the relation of photocurrent (I_{pc}) versus illumination intensity (Φ) was studied for the 150, 250 and 300 K temperatures. The plot of $\ln(I_{pc})$ vs. $\ln(\Phi)$ for these temperatures is shown in Fig. 4.45. The relation between photocurrent and the illumination intensity follows the $I_{pc} \alpha \Phi^n$ expression, where the

power exponent (n) is indicating the behaviour of the recombination mechanism [68].

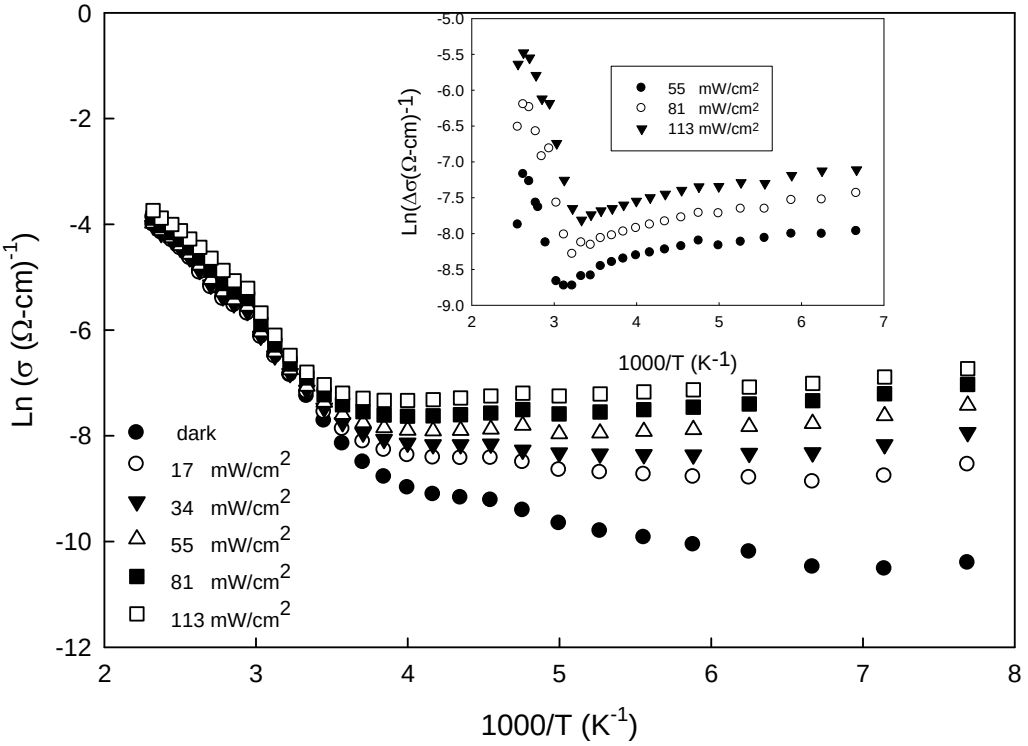

Figure 4.44: The temperature dependence of dark and illuminated conductivity under the illumination intensity of 17, 34, 55, 81, 113mW/cm^2. The inset of figure shows the temperature dependence photoconductivity.

From the slope of the curve, it was found that the (n) values varied between 1 and 2, which is the indication of supralinear photoconductivity related with the two centre model (for the case of n>1). According to this model the life time of free carriers is increasing with increasing illumination intensity. Thereby, it is becoming more photosensitive with increasing illumination intensity [69].

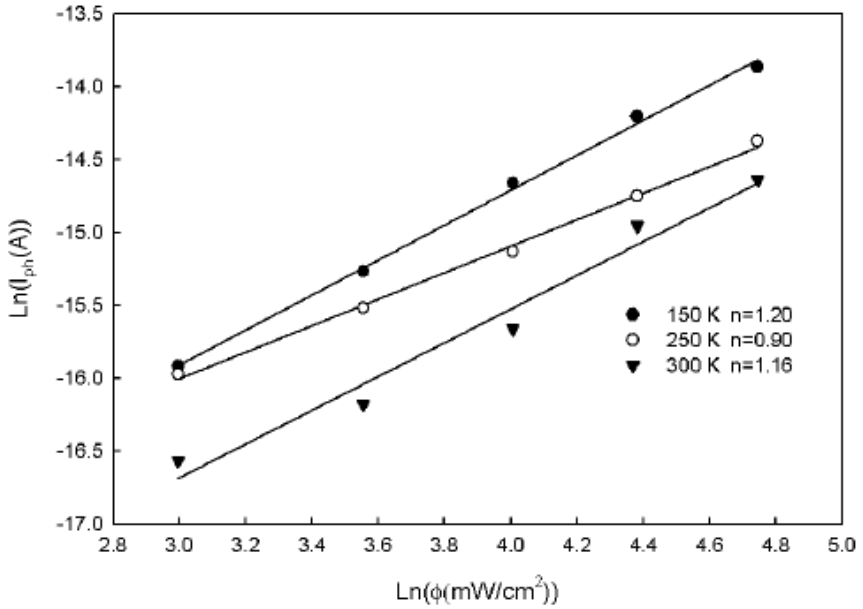

Figure 4.45: The photocurrent-intensity relation for the as-grown AGS thin film.

The dark conductivity and photoconductivity for the annealed films were quite different, namely, there is no any response under the illumination. A similar behaviour was reported for $AgGaS_2$ thin films [13]. The changes observed in photoconductivity probably occur due to the structural modification introduced by the deposition of the conducting silver layer. By illuminating the films, free charge carriers are generated depending on illumination intensity. The life-time of generated free carriers has pronounced effect on the conductivity, which could be affected partially by defects and the space charge regions present on the surface or grain boundaries. Thus, the observed remarkable photosensivity in the as-grown film probably could be the result of the layer by layer depositing of the film structure. Then, the photo-and thermally-generated carriers are gathered with the applied field in this conducting layer and transported to the probes without encountering so much defects (life-time killing) and space charge regions responsible for building barrier potentials.

4.6 Characterization of $AgGaS_2$ Thin Films Deposited by Thermal Evaporation

In this part of thesis, the aim is to study the effect of post-annealing on the structural, electrical, and optical properties of $AgGaS_2$ thin films. The substrate temperature was kept constant at around 300 ^oC during deposition cycle. The thickness of films was measured in-situ by thickness monitor and following to deposition by profilometer, which was found to be around 700 nm consisted of $AgGaS_2$/Ag/ $AgGaS_2$ layers with thickness of 300/100/300 nm, respectively. The $AgGaS_2$ thin films were prepared on to both soda-lime and quartz substrates by two-source thermal evaporation method. However, the mono-phase $AgGaS_2$ has been obtained only for the film deposited on to the quartz substrates. Thus, we have focused on investigation the structural, electrical and optical properties of $AgGaS_2$ thin films deposited on to soda lime glass substrate.

4.6.1 Structural and Compositional Analysis

To investigate the composition of the powder (used as evaporation source) and deposited thin films EDXA measurements were performed. The atomic percentages of constituent elements (Ag, Ga, and S) were found to be significantly depending on post-annealing process. Results obtained for powder, as-grown and $AgGaS_2$ thin films annealed at 450-700 ^oC were presented in Table 4.12. As can be understood from results, there is a nearly stoichiometric composition for the source powder within the experimental error (2%), but it is not the case for the deposited films. Namely, it reveals that as-grown films contain excess gallium and deficient in silver and sulphur. As the annealing temperature increases, the atomic percentage of Ag increases and that of Ga and S decreases significantly, which probably originates from either the large difference between the vapour pressures of constituent elements during deposition or re-evaporation of weakly-bound elements from the substrate surface with post-annealing as previously observed in Ag-Ga-S thin films.

Table 4.12: EDXA results obtained for powder and $AgGaS_2$ thin films

Sample	Atomic percentage (%)±2 Ag	Ga	S
Powder	23.72	27.81	48.47
As-grown	19.00	27.00	54.00
450 ^oC	20.57	26.00	53.43
650 ^oC	23.08	24.42	52.50
700 ^oC	25.02	23.00	51.98

Fig.4.46 shows the XRD diffractograms obtained for powder, as-grown, and $AgGaS_2$ thin films annealed at 450-700 ^oC. It reveals that as-grown film is amorphous in nature and includes small Ag crystallinities [99] with identified (111) plane reflection. Annealing film at 450 ^oC results in improvement in crystallinity of silver phase and triggering of the nucleation for the development of GaS [116] and $AgGaS_2$ [117] with the reflection along (004) and (400), respectively.

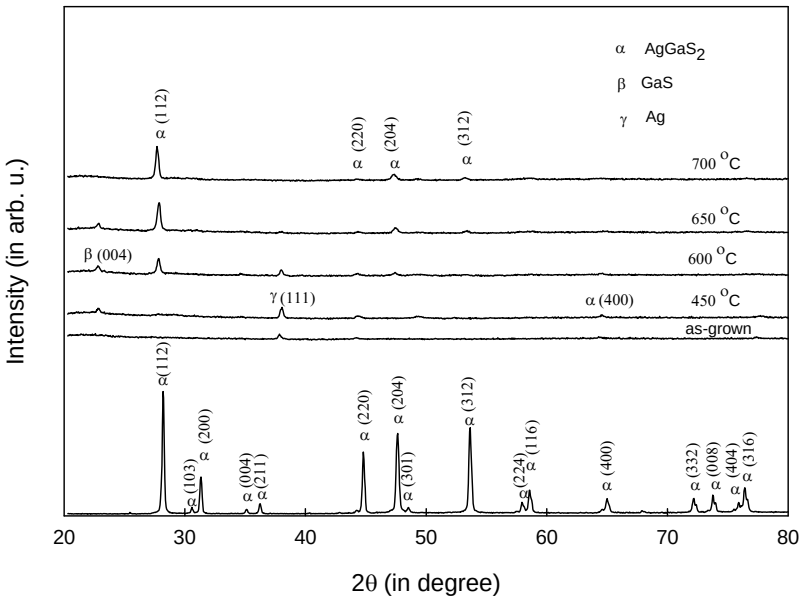

Figure 4.46: X-ray diffraction patterns of source powder, as-grown and $AgGaS_2$ thin film annealed in the temperature range of 450-700 ^oC.

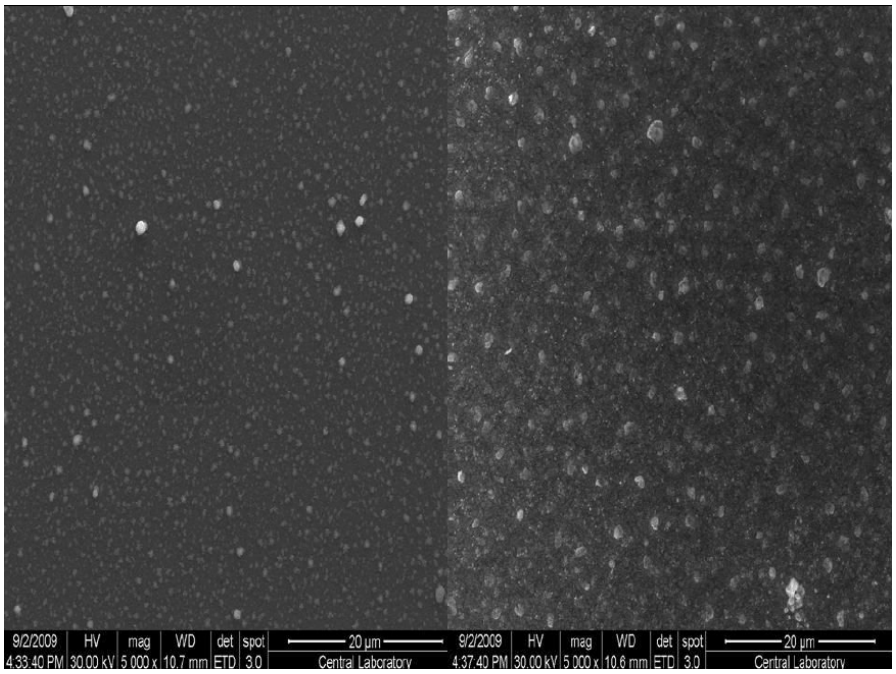

(a_1) (b_1)

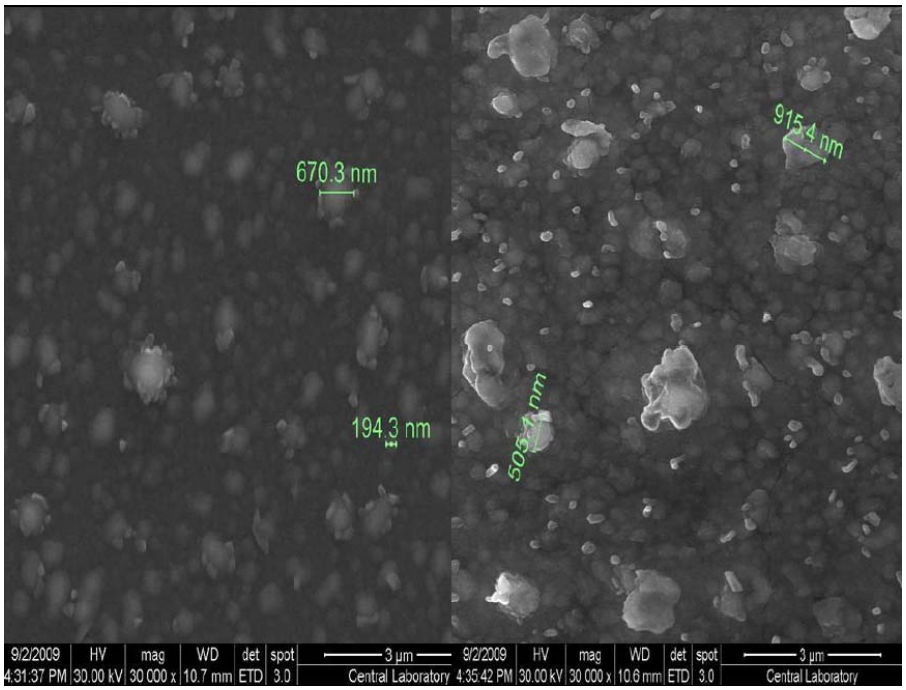

(a_2) (b_2)

Figure 4.47: SEM micrographs for (a_1, a_2) as-grown and (b_1, b_2) $AgGaS_2$ films annealed at 700 ^oC.

As can be seen from Fig.4.46, there is an increase in crystallinity of $AgGaS_2$ with increasing annealing temperature. After annealing the film at 700 ^oC, the Ag and GaS

secondary phases disappears clearly and film shows mono-phase $AgGaS_2$ with chalcopyrite structure and preferred (112) plane orientation. The disappearance of Ag and GaS secondary phases at high annealing temperature can be attributed to the coalescence of nucleated grains in the early stage of crystallization to form $AgGaS_2$ driven by thermal energy supplied by post-annealing as observed in electron-beam evaporated $AgGaSe_2$ thin films introduced previously.

To study the surface morphology of the deposited films and understand the effect of post-annealing on it, the SEM measurements were carried out for as-grown and $AgGaS_2$ thin film annealed at 700 ^oC. The recorded micrographs are shown in Fig.4.47. As can be easily understood from the pictures, the surface of films is nearly homogenous consisted of drop-like (spots) features distributed uniformly over the surface. After annealing at 700 ^oC, the density and size of droplets seem to be increasing; this could be attributed to the improvement in crystallinity as a consequence of post-annealing that consisted with the outcome drawn from the XRD study.

4.6.2 Optical Analysis

Fig. 4.48 and Fig. 4.49 show the spectral distribution of transmission and reflection obtained at room temperature in the wavelength range of 400-1100 nm, respectively. The average transmission is 18 % and 50 % for as-grown and sample annealed at 700 ^oC, respectively. Namely, transparency increases with increasing annealing temperature, which is usually attributed to the improvement in crystallinity. On the other hand, it can also be seen from Fig.4.49 that the reflection decreases with increasing annealing temperature, which changes about from 40 % to 5 % on annealing from room temperature to 700 ^oC. Such a decrease in reflection could be attributed to the existence of decreasing scattering of light from the surface and bulk of sample due to the increasing uniformity on the surface and the improvement in the crystallinity as observed from both the SEM and XRD studies. Optical absorption coefficient was determined through the eqn. (2.16). The results show that the relation between absorption coefficient (α) and photon energy ($h\nu$) follows the relation given

in eqn. (2.25).

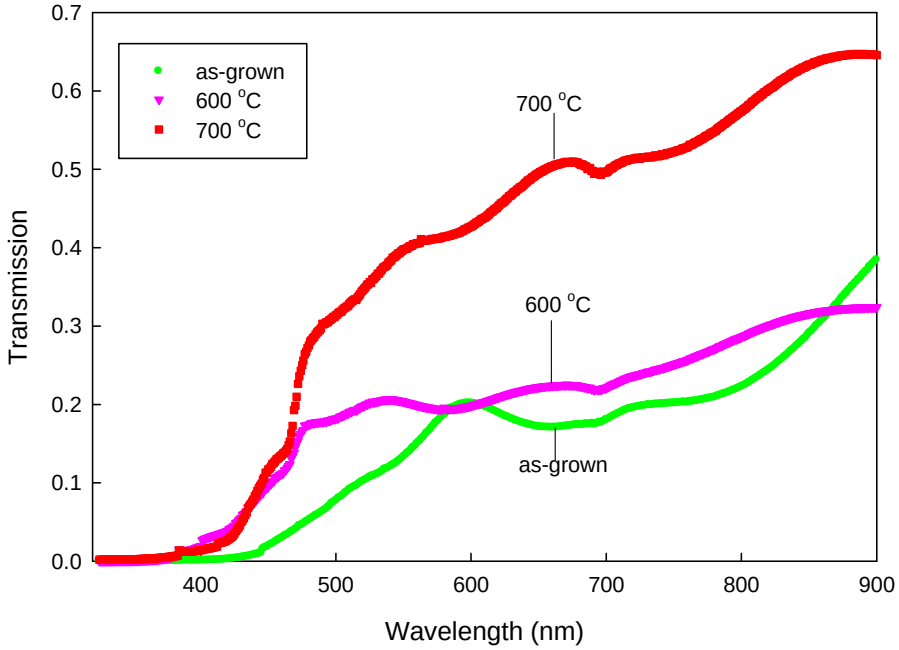

Figure 4.48: Transmittance spectrum for the as-grown, and films annealed at 600 and 700 °C.

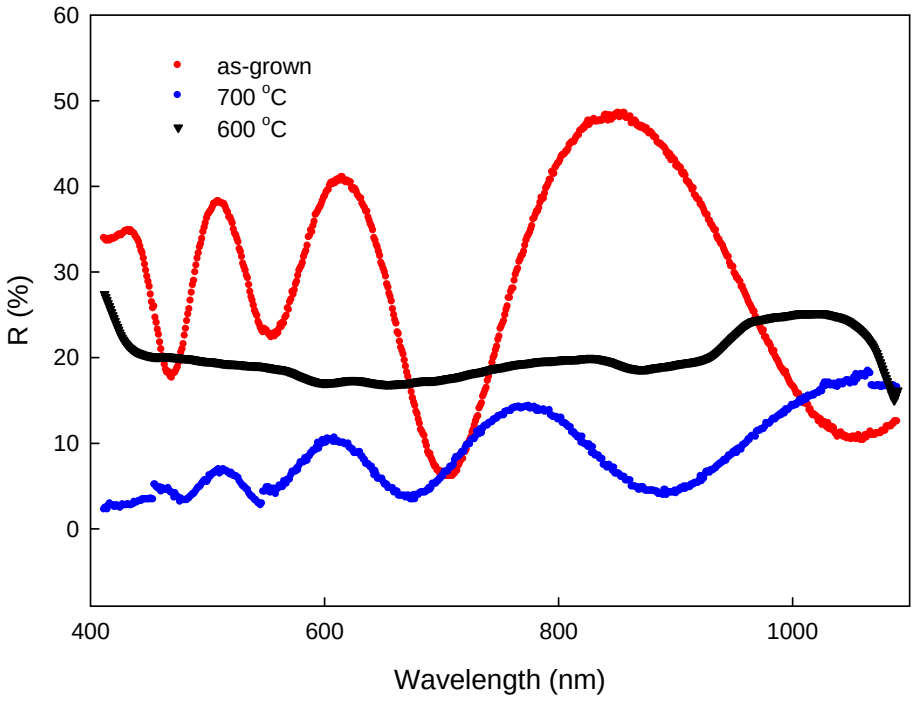

Figure 4.49: Reflectance spectrum for the as-grown, and films annealed at 600 and 700 °C.

From the extrapolating the straight line revealed from the $(\alpha h\nu)^2$ vs $(h\nu)$ (Fig.4.50), band gap values were calculated and found to be 2.65, 2.74, and 2.79 eV for as-grown and sample annealed at 600 and 700 ^{o}C, respectively. It reveals that there is a systematic increase in band gap energy values along with increase in annealing temperature that could be due to the elimination of defect states, disorder and early crystallized secondary phases (Ag and GaS) in structure following to annealing process.

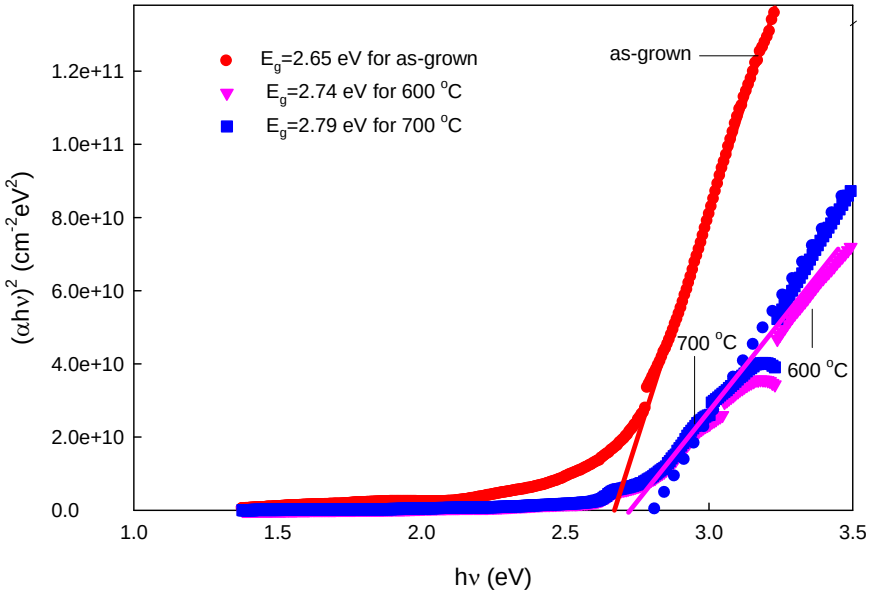

Figure 4.50: Plot of $(\alpha h\nu)^2$ against $(h\nu)$ for as-grown and $AgGaS_2$ thin films film annealed at 350 ^{o}C and 550 ^{o}C.

4.6.3 Electrical Analysis

Temperature dependent conductivity measurement was carried out in the temperature range of 100-430 K for the as-grown and sample annealed at 600 and 700 ^{o}C. The plot of conductivity (Ln(σ)) versus inverse absolute temperature is shown in Fig.4.51. This dependence reveals that conductivity increases exponentially with the inverse temperature. Hence, the resistivity increases with the increasing annealing temperature. The room temperature values were calculated to be as $2x10^3$, $5x10^3$, and

$9x10^6$ Ω-cm for as-grown, sample annealed at 600 and 700 °C, respectively. The variation of conductivity as a function of temperature shows different linear region for all samples except annealed sample at 600 °C, which is confirmation of existing a typical conduction mechanism activated in a temperature region with specific activation energy. These regions correspond to the various defect levels in forbidden band gap with the average activation energies (in Table 4.13).

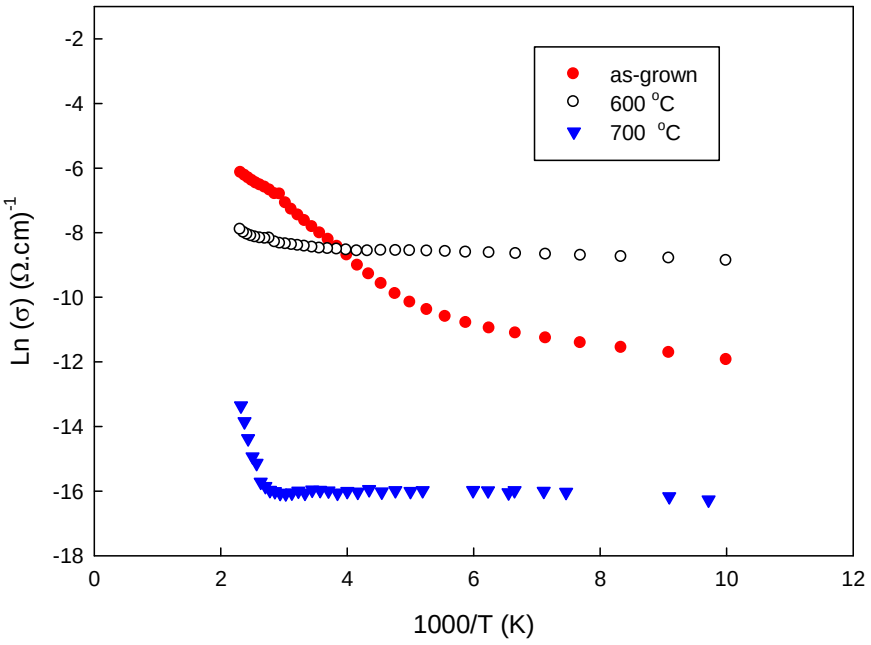

Figure 4.51: Temperature dependent electrical conductivity of as-grown and $AgGaS_2$ thin films annealed at 600 °C and 700 °C.

Table 4.13: Calculated activation energies.

Sample	Low Temp. (K)	Ea_1 (meV)	High Temp. (K)	Ea_2 (meV)
As-grown	100-190	28	200-430	133
600 °C	100-220	-	270-430	32
700 °C	100-360	-	370-430	631

The plausible reason behind these levels is the availability of potential point defects such as vacancies and interstitials in the structure. There are two levels for as-grown, while it is almost single level for the annealed samples. The change from the two levels to one level could be due to the elimination of some defect-related states in a structure following to the annealing resulted in improvement in crystallinity. In addition, it is clear that annealing sample at 700 ^{o}C give rise to formation of states in forbidden band gap with relatively high activation energy (631 eV) along with the formation of mono-phase $AgGaS_2$ in the structure. So, the large increase in resistivity may be related with the formation of these levels, which reduces their contributions to the conduction by thermally excited free charge carriers. Another likely reason for this increase on annealing at 700 ^{o}C may be the Ag crystallites that still exist in the structure up to 600 ^{o}C, which may facility the flow of free charge carriers. The same behaviour has been reported for $AgInS_2$ [118]. A similar situation was also reported previously for $AgGaSe_2$ [20]. Namely, in that study it was observed that up to annealing temperature of 400 ^{o}C, the resistivity decreases with increasing annealing temperature, while it increases above 500 ^{o}C, which can be attributed to the high resistive nature of $AgGaSe_2$ in mono-phase. Since $AgGaS_2$ and $AgGaSe_2$ are close together in terms of resistivity (semi-insulating materials), the same reason may be plausible in our case after the development of mono-phase $AgGaS_2$ in the structure.

To understand the nature of conductivity more clearly the physical parameters that determine the conductivity should also be known such as mobility (μ) and free carrier concentration (n) since, $\sigma = n\mu q$. The free carriers are electrons, which are confirmed by means of hot-probe and Hall measurements and found to be behaving as *n*-type conduction. The n-type conduction in chalcopyrite compounds those have large band gap such as $AgGas_2$ and $CuGaS_2$ is generally attributed to the VI-element vacancies, which have quite low formation energies [119]. Thus, the deviation observed in stoichiometry of $AgGaS_2$ may results in formation of S vacancies, playing important role in *n*-type conduction. To determine the electrical parameters, the Hall measurement was carried out for as-grown and sample annealed at 600 and 700 ^{o}C at temperature of 100-350K. Fig. 4.52 and Fig. 4.53 show the variation of mobility and free carrier concentration (electrons) as a function of temperature for as-grown and annealed samples, respectively. As can be seen from Fig.4.48 and results Table 4.14,

the mobility increases on increasing annealing temperature.

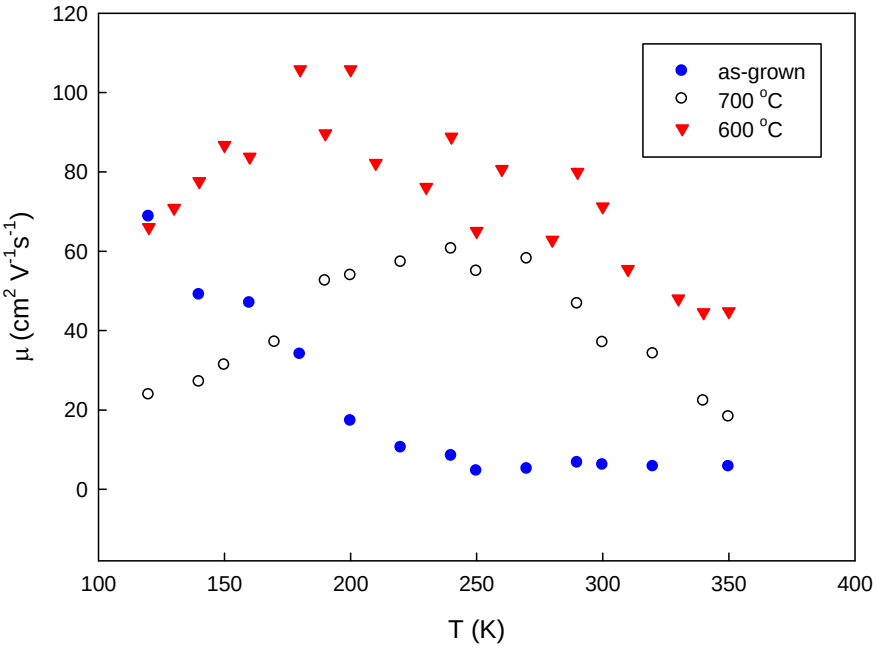

Figure 4.52: Variation of mobility (μ) as a function of temperature for as-grown and annealed $AgGaS_2$ thin films at 600 and 700 °C.

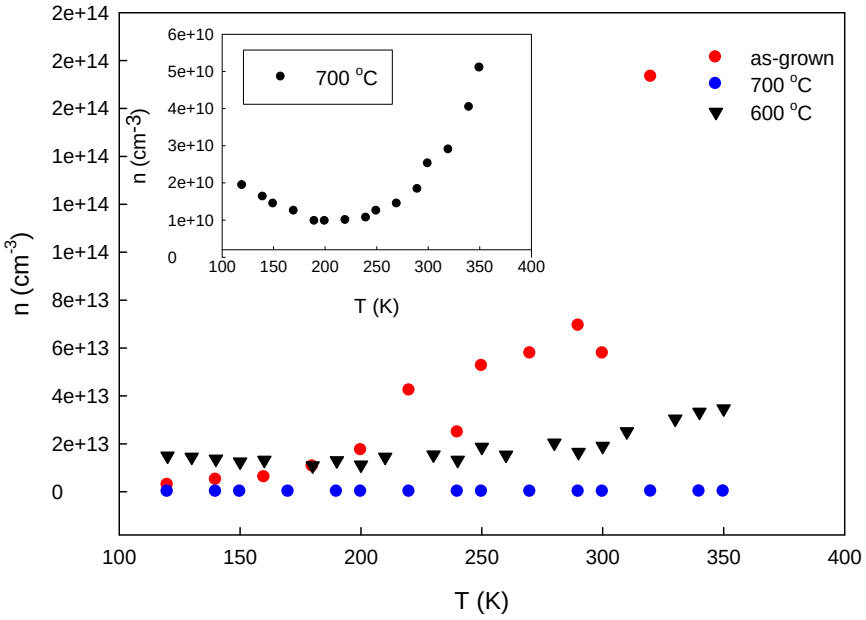

Figure 4.53: Variation of carrier concentration (n) as a function of temperature for as-grown and annealed $AgGaS_2$ thin films at 600 and 700 °C .

Table 4.14: Calculated room temperature (RT) mobility values.

Sample	μ (RT) ($cm^2V^{-1}s^{-1}$)	exponent (β)
As-grown	6.7	(-3.0) (100-250K)
600 ^oC	64	(+1.2) (100-180 K) and (-2.0) (230-350 K)
700 ^oC	37	(+1.6) (120-220 K) and (-3.0) (250-350K)

The room temperature (RT) values of mobility were found to be 6.7, 64, and 37 $cm^2V^{-1}s^{-1}$ for as-grown and film annealed at 600 and 700 ^oC, respectively. The increase in mobility with annealing may be attributed to the increase observed in grain size, which results in the increase in the mean free paths of free carriers [120]. However, the decrease in mobility on annealing from 600 to 700 ^oC is probably originated from the elimination of Ag crystallites, which facilities the passage of free carriers compared with other phases.

To understand scattering mechanisms the Log (μ) versus Log (T) plot was determined for as-grown and film annealed at 700 ^oC, since the slope of revealed linear regions gives the exponent of $\mu\alpha T^{\pm\beta}$ that determines the existing scattering mechanism in the studied temperature interval. This dependence reveals one and two regions for as-grown and annealed film, respectively. Namely, for the as-grown the mobility systematically decreases as the temperature increases by obeying $\mu\alpha T^{-n}$, whihe the mobility fits to $\mu\alpha T^{+\beta}$ and $\mu\alpha T^{-\beta}$ for the annealed film for low and high temperature regions, respectively with the calculated exponent (β) values given in Table 4.14. Based on the calculated exponent values, it is possible to suggest that for the as-grown sample the scattering due to the phonons is the dominant mechanism in almost all studied temperature range, while it is not the case for the annealed film, namely, the impurity ionization and phonon scattering mechanisms are dominant in the structure in low and high temperature regions, respectively.

Table 4.15: Calculated carrier concentration for as-grown and annealed $AgGaS_2$ thin films

Sample	n at (RT) (cm^{-3})	Change in n (120-350 K)
As-grown	$5.7x10^{13}$	$1x10^{13}$- $2x10^{14}$ cm^{-3}
600 ^oC	$1.9x10^{13}$	$1x10^{13}$- $4x10^{13}$ cm^{-3}
700 ^oC	$2.5x10^{10}$	$1x10^{10}$- $6x10^{10}$ cm^{-3}

The carrier concentration of $AgGaS_2$ thin film decreases as the annealing temperature increases as shown in Fig.4.53. The room temperature values were found to be $5.7x10^{13}$, $1.9x10^{13}$, and $2.5x10^{10}$ cm^{-3} for as-grown and sample annealed at 600 and 700 ^oC, respectively. The variation of carrier concentration in studied temperature intervals are summarized in Table 4.15. The improvement in crystallinity with annealing has resulted in elimination of some point defects (vacancies, interstitials, etc.) introducing donor levels with calculated relatively low activation energies that contributes the conductivity by thermal excitation based generated free carriers. Thus, the elimination of these levels may result in such a drastic decrease in free carrier concentration. The other side effect of improvement of crystallinity is the increase in grain size that resulted in increase in mobility. In summary, the Hall measurement has shown that the mobility increases and carrier concentration decreases with post-annealing. And, since the decrease of carrier concentration is more than the increase of mobility we have observed such a drastic decrease in conductivity following to annealing process.

4.6.4 Photo-Electrical Analysis

Temperature dependent photoconductivity measurements were carried out in the temperature range of 100-430 K for as-grown and film annealed at 600 and 700 ^oC.

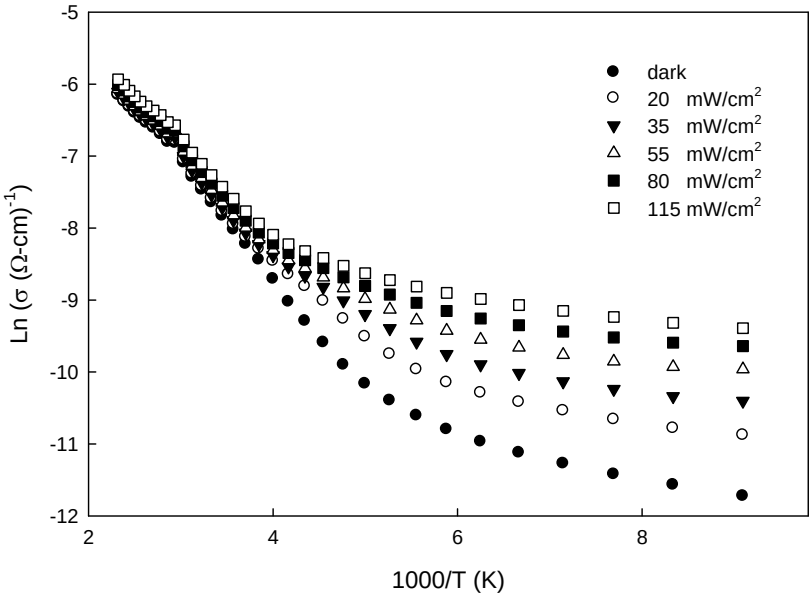

Figure 4.54: The temperature dependence of dark and illuminated conductivity under the illumination intensity of 17, 34, 55, 81, 113mW/cm^2 for as-grown $AgGaS_2$ thin film.

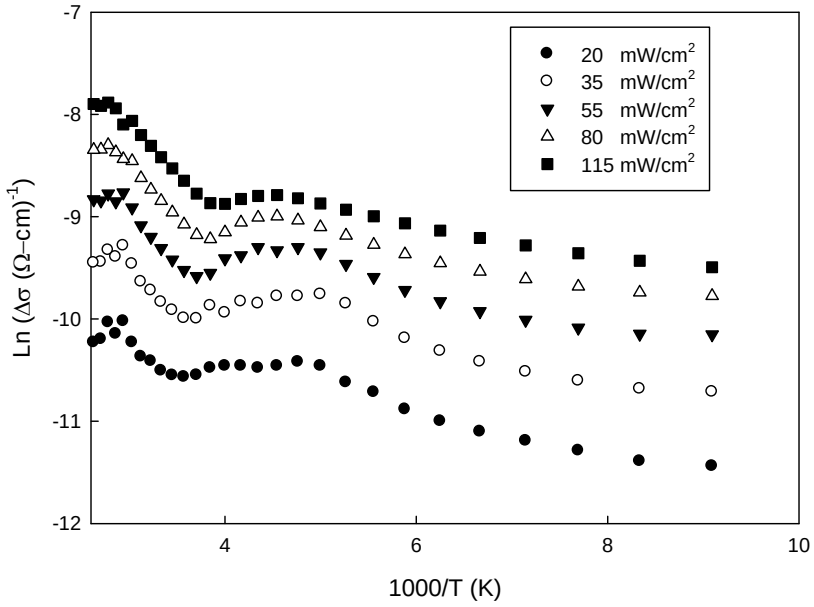

Figure 4.55: The temperature dependence of photoconductivity under the illumination intensity of 17, 34, 55, 81, 113mW/cm^2 for as-grown $AgGaS_2$ thin film.

Table 4.16: Calculated activation energies under different illumination intensities.

Intensity (mW/cm^2)	Ea_1 (meV) (120-200K)	Ea_2 (meV) (270-350K)
20	20	72
35	19	93
55	17	87
80	16	81
115	13	80

However, only as-grown film has shown sensitivity to light. The variation of conductivity under illumination as a function of temperature for the as-grown film is shown in Fig. 4.54. As can be seen from the figure, there is an increase in conductivity with increasing temperature and illumination intensity. The conductivity under light exhibits different behaviour at different temperature intervals.

That is, at low temperature there is a weak variation of conductivity with increasing temperature, however, there is a considerable increase in conductivity as the temperature increases at high temperature region. Photoconductivity (PC) ($\Delta\sigma$) was calculated by subtraction of dark conductivity from the conductivity measured under illumination of light. Fig. 4.55 shows the temperature dependence of PC under different illumination intensities (ranging from 20 to 115 mW/cm^2). As can be seen, the PC increases as the temperature and illumination intensity increases. It also reveals two distinct regions, low and high temperature regions. In low temperature region, the variation of PC with temperature is quite low. However, in high temperature region it is seen that there is a more pronounced variation of PC with temperature. From the slope of linear regions revealed at low and high temperature regions, the activation energies were calculated. In polycrystalline films, these activation energies are the representation of variation in the barrier height of grain boundaries under specific illumination level [108]. The linear regions with calculated activation energies (E_a) (barrier height changes) under different illumination intensities are presented in Table 4.16. The calculated activation energies under

illumination are less than those obtained from the dark conductivity. It is a reasonable result since the illumination results in the generation of free electron and holes that contributes increase in conductivity by either increase in carrier concentration or decrease in the barrier height created in the grain boundaries. Namely, the defects results in building barrier potentials since they are behaving as traps and charged by capturing free carriers. Thus, if the created minority carriers are captured by such type traps, it brings about neutralizing these space charge regions and subsequently reducing the barrier potential [108]. In our case, the observed decrease in activation energies following to the increasing illumination intensity could be attributed to modification of barrier height on illumination. Temperature dependence of PC also reveals that above the critical temperature (T=360 K) the PC decreases as the temperature increases for all intensities. The similar behaviour was observed for Ag-Ga-S thin films determined previously in this thesis. As it is explained before, this behaviour is called the thermal quenching and commonly attributed to the co-existence of sensitizing and recombination centers. To investigate the nature of these centers, the relation between the photocurrent (I_{PC}) and illumination intensity (Φ) was determined. Fig. 4.56 shows the variation of photocurrent as function of illumination intensity plotted for 100, 150, 200, 250, 300 and 400 K.

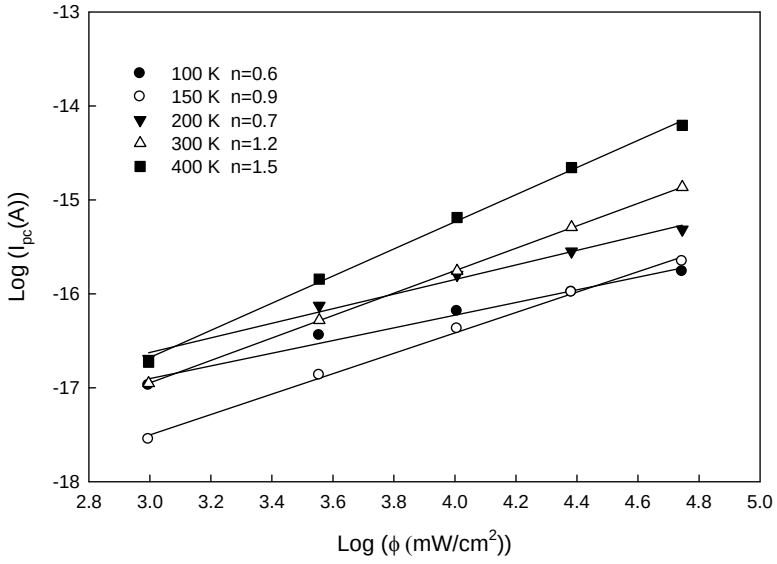

Figure 4.56: The photocurrent-intensity relation for the as-grown $AgGaS_2$ thin film.

The relation between them is given by $I\alpha\Phi^{\beta}$. Here, β is the exponent calculated from the slope of $Log(I_{PC}) - Log(\Phi)$ and represents the type of recombination mechanism. As can be seen from the figure, the n value is varying from 0.6 to 0.9 ($\beta<1$) and from 1.2 to 1.5 ($\beta>1$) at low and high temperatures, respectively. As explained in theoretical consideration part, $\beta<1$ case stands for the sublinear photoconduction explained by one center model (claims the existence of only one type imperfection), which means that life-time of free carriers decreases as the illumination intensity increases. And, $\beta>1$ case represents the supralinear character explained by two-center model, which implies that the life-time increases and material becomes more photosensitive on increasing illumination intensity.

CHAPTER 5

CONCLUSIONS

In this study, an attempt was made to investigate structural, electrical and optical properties of $AgGa(Se_{2-x}S_x)$ thin films for x changing between 0 and 2.

$AgGa(Se_{0.5}S_{0.5})_2$ thin films deposited onto soda-lime glass substrates by using thermal evaporation method. Compositional analysis has revealed that as-grown films were silver- and selenium- deficient, gallium- and sulphur- rich. As the samples were annealed a systematic decrease in Ag was observed. In addition, following to this process, variation in color of the films (from yellow to dark gray) was observed, which was attributed to the structural modification in the structure. Structural analysis has shown that there is an increase in crystallinity on annealing treatment deduced from XRD diffractograms. It has also revealed that there is co-existance of $AgGaS_2$ and α-Ga_2Se_3 phases up to 550 ^oC and S phase over 600 ^oC, which is probably stemmed from the decomposition of Ga_2Se_3 phase at this temperature because of the segregation of sulphur atoms. The absorption coefficient and band gap energy of samples were calculated from the transmittance measurements. Results revealed that there is a shifting of the absorption edge slightly to the different energies with annealing, which is correlated with the structural transformation from amorphous to polycrystalline phase, modifications of the phases depending on the annealing process and the segregations of constituent elements. The segregation mechanism was also studied by performing XPS measurements. Based on this measurement, it was found that there is a drastic variation in amount of S and Ag on the surface on annealing. The substantial change in S obtained from XPS study after annealing is consisted with the behaviour analysed from XRD study and allow us to suggest that the out-diffusion of weakly bounded sulphur in the structure to surface and subsequently volatilization is triggered with annealing. However, the opposite behaviour is observed for the silver, that is, post-annealing results in diffusion of Ag

from the upper to lower layers in the material The observed modification in the structure has an important effect on determining many properties of the films. The results of electrical characterization has shown that the room temperature resistivity values of the samples varied from 0.7 x 10^8 to 0.9 x 10^7 (Ω-cm) depending on the changing annealing temperature from room temperature to 600 ^oC, which is plausible to assign these modifications.

The effects of annealing temperature on the structural and morphological properties of the $AgGaSe_2$ thin films deposited onto the soda-lime glass substrates by using electron-beam technique have been studied. Based on EDXA analysis, it was found that the as-grown films were not stoichometric, namely, a Ag rich but Ga and Se deficient composition, which was also verified by structural analysis. XRD study has shown that annealing samples at 300 ^oC showed the reflection coming from Ag elements, which subsequently disappeared depending on the increasing annealing temperature. From the recorded SEM micrographs, it was clearly observed that the large agglomerations (spots) of Ag on the surface of the films disappear as the annealing temperature increases. The elimination of these large spots on annealing could be attributed to either the diffusing Ag atoms from surface to bulk or staying at the layer near to the surface consisting of mainly segregated Ga and Se with increasing annealing temperature. The grain sizes on the surface of the films were measured to be in the 82-526 nm from SEM pictures. SEM micrographs have revealed also that post-annealing has a pronounced effect on the modification of the film structure and morphology. The investigation of composition and chemical bonding on the surface and near to the surface of the $AgGaSe_2$ thin films have been studied by performing XPS measurements. The results showed that Ag, Ga, and Se constituent and C and O contaminanents were included in all samples. The identification of chemical states using the dominant peaks of Ag (3d), Ga (3p) and Se (3p) photoelectron peaks have shown the evolution of different phases of binary and ternary structures took place on the increasing annealing temperature. This evolution was attributed to the segregation of Ga and Se atoms to the surface of the films and Ag atoms to the bulk of the films as observed from EDXA results. Namely, it was deduced that Ag content in the structure decreases, while the Ga and Se content increases on the surface depending on the increasing annealing temperature.

$AgGaSe_2$ thin films were also deposited by using sputtering technique onto soda-lime glass substrates. $AgGaSe_2$ thin films were prepared from layer by layer deposition of Ag and GaSe targets by means of DC and RF magnetron sputtering process, respectively. Through the systematic compositional analyses we have observed that there was a Ga-rich composition. In addition, a remarkable variation in amount of constituent elements especially in Se following to rapid-annealing process was observed, which was attributed to the re-evaporation high volatile Se from the surface at high annealing temperatures. Based on XRD analysis, it was found that the Ag metallic phase exists in the as-grown $AgGaSe_2$ structure and that was available in the structure up to the annealing temperature of 450 ^oC. However, increasing annealing to 550 ^oC resulted in the single phase of polycrystalline $AgGaSe_2$ to be as the dominant phase in the structure with the preferred orientation along (112) direction. The grain size of the films was found to be increasing from 49 nm to 72 nm with increasing annealing temperature from 550 to 600 ^oC. In addition, some structural parameters like displacement and tetragonal distortions were calculated as 0.299 and 0.184, respectively. Transmittance and reflectance measurement were carried out in the wavelength range of 325-1100 nm at room temperature and it was found that there was a remarkable variation in transmission and reflection as annealing temperature increases. The variation in reflectance and transmittance was attributed to the structural modifications on post-annealing process. The crystal-field and spin-orbit splitting levels were detected by observing transitions of band to band, the crystal-field, and spin-orbit level with characteristic energy values 1.77 , 2.00, and 2.25 eV, respectively for film annealed at 550 ^oC. Almost the same values were observed from the photospectral response measurements. Temperature dependent conductivity and Hall effect measurements were performed in the temperature range of 100-430 K. The electrical resistivity of the films was in the range of 30-1000 Ω-cm. The room temperature carrier concentration increased from $9.6x10^{14}$ to $6.6x10^{16}$ cm^{-3} as the annealing temperature was elevated to 550 ^oC. Through the Log (μ) versus Log (T) plot the nature of the scattering mechanisms have been determined. It was found that in low temperature region the ion scatterings are determining scatterings, while it is phonons for high temperature regions.

$AgGaS_2$ thin films were successfully deposited on to the soda-lime glass substrates from the single crystal powder $AgGaS_2$ and excess interlayer of silver to prevent silver (Ag) deficiency in the structure by using double source thermal evaporation system. An attempt to growth of $AgGaS_2$ from the evaporation stoichiometric sintered single crystalline powder has failed due to the deficiency in silver and excess of Ga and S in composition of deposited thin films. In order to overcome the deficiency of Ag in the structure, double sources including Ag shots and $AgGaS_2$ sintered powder were used. To form $AgGaS_2$ thin films the deposition of Ag and $AgGaS_2$ thin layers were carried out in the $AgGaS_2$/Ag/ $AgGaS_2$ sequence with thickness of 900/50-55/900 nm. XRD analysis showed that layer by layer deposition has resulted in growth of Ag-Ga-S (AGS) system with stoichiometry of $AgGa_5S_8$. Based on the XRD analysis, it was revealed that AGS grows with co-existence of Ag phase at the annealing temperature of 400 ^oC. The structure of the film annealed at 550 ^oC had AGS structure with the preferred orientation along (101) direction. Optical band gap values calculated by using transmission and reflection were found to be varying between 2.30 and 2.75 eV on increasing annealing temperature from 350 to 550 ^oC. The evaluated values of refractive indexes by using envelope method could be found in the range of 1.8-2.6 in the studied wavelength region. Photoconductivity measurements were performed under different illumination intensity ranging between 17 and 113 mW/cm^2 in the 100-430 K temperature range. Results showed that the segregation of constituent elements produced different recombination and sensitizing centers at different energy levels, which was assigned to the structural modification introduced during the deposition or post-annealing process.

In final part of thesis, our aim was to obtain mono-phase AGS thin films with $AgGaS_2$ stoichiometry by using double source thermal evaporation system and then study the effect of post-annealing on the structural, electrical, and optical properties of deposited thin films. The thickness of films was found to be around 700 nm consisted of $AgGaS_2$/Ag/ $AgGaS_2$ layers with thickness of 300/100/300 nm, respectively. The $AgGaS_2$ thin films were prepared on to both soda-lime and quartz substrates by two-source thermal evaporation method. However, the mono-phase $AgGaS_2$ has been obtained only for the film deposited on to the quartz substrates.

EDXA measurements have shown that the atomic percentages of constituent elements (Ag, Ga, and S) were significantly depending on post-annealing process. From the obtained XRD diffractograms it was found that that as-grown film is amorphous in nature and includes small Ag crystallinities. On annealing film at 450 ^{o}C it was observed that the transformation to polycrystalline structure is taking place with co-existance of Ag, GaS, and $AgGaS_2$ phases.On increasing annealing temperature 700 ^{o}C it was observed that Ag and GaS secondary phases disappears clearly and film shows mono-phase $AgGaS_2$ with chalcopyrite structure and preferred (112) plane orientation. This process was attribured to the coalescence of nucleated grains belonging to Ag and GaS in the early stage of crystallization to form $AgGaS_2$ driven by thermal energy supplied by post-annealing. SEM measurements were carried out for as-grown and $AgGaS_2$ thin film annealed at 700 ^{o}C to see the effect of post-annealing on morphology of deposited films. From the recorded pictures it was clearly understood that surface of films is nearly homogenous consisted of drop-like (spots) features distributed uniformly over the surface. And, the density and size of droplets seem to be increasing on annealing sample at 700 ^{o}C, which was attributed to the improvement in crystallinity with annealing. Spectral distribution of transmission and reflection obtained at room temperature in the wavelength range of 400-1100 nm. From these measurements it was deduced that transparency increases and reflection decreases with increasing annealing temperature, which is usually attributed to the improvement in crystallinity and existence of less scattering of light from the surface and bulk of sample due to a more uniform surface, respectively. Band gap values were calculated and found to be 2.65, 2.74, and 2.79 eV for as-grown and sample annealed at 600 and 700 ^{o}C, respectively. That is, there is a systematic increase in band gap energy values along with increase in annealing temperature. Temperature dependent conductivity measurement was carried out in the temperature range of 100-430 K for the as-grown and sample annealed at 600 and 700 ^{o}C. It was found that the resistivity increases as the annealing temperature increases and room temperature values were calculated to be $2x10^3$, $5x10^3$, and $9x10^6$ Ω-cm for as-grown, sample annealed at 600 and 700 ^{o}C, respectively. The increase in resistivity was attributed to existing of levels found to be have high activation energy with respect to as-grown film. Another plausible

reason behind the increase in resistivity was thought to be stemming from the elimination of Ag crystallites at high annealing temperature, which may facility the flow of free charge carriers. Mobility (μ) and free carrier concentration (n) parameters were determined by means of performing Hall measurement. It was deduced that deposited films behave as n-type conduction verifed by both Hall measurement and hot-probe method. The room temperature (RT) values of mobility were found to be 6.7, 64, and 37 $cm^2V^{-1}s^{-1}$ for as-grown and film annealed at 600 and 700 ^oC, respectively. Namely, there is an increase in mobility with annealing, which was attributed to the increase observed in grain size. From the Log (μ) versus Log (T) plot, the scattering mechanisms were investigated for as-grown and film annealed at 700 ^oC. It was found that for the as-grown sample the scattering due to the phonons is the dominant mechanism in almost all studied temperature range, while it is not the case for the annealed film, namely, the impurity ionization and phonon scattering mechanisms are dominant in the structure in low and high temperature regions, respectively. The room temperature carrier concentration values were found to be $5.7x10^{13}$, $1.9x10^{13}$, and $2.5x10^{10}$ cm^{-3} for as-grown and sample annealed at 600 and 700 ^oC, respectively. That is, there is a drastic decrease in carrier concentration on post-annealing, which was attributed to the improvement in crystallinity on annealing has resulted in elimination of some point defects (vacancies, interstitials, etc.) introducing donor levels with calculated relatively low activation energies that contributes the conductivity by thermal excitation based generated free carriers. Thus, the elimination of these levels may result in such a drastic decrease in free carrier concentration. In summary, since the decrease of carrier concentration is more than the increase of mobility we have observed such a drastic decrease in conductivity following to annealing process. Temperature dependent photoconductivity measurements were carried out in the temperature range of 100-430 K for as-grown and film annealed at 600 and 700 ^oC. However, only as-grown film has shown sensitivity to light. It was observed that the photoconductivity (PC) increases as the temperature and illumination intensity increases. The linear regions with calculated activation energies (E_a) (barrier height changes) under different illumination intensities are calculated and found to be less than those obtained from the dark conductivity. The observed decrease in activation energies following to the

increasing illumination intensity was attributed to modification of barrier height on illumination. In addition, it was found that above the critical temperature (T=360 K) the PC decreases as the temperature increases for all intensities, which is called the thermal quenching and commonly attributed to the co-existence of sensitizing and recombination centers. The nature of these centers has been investigated through the relation between the photocurrent (I_{PC}) and illumination intensity (Φ). This relation is expressed by $I_{PC} \alpha \Phi^n$ term. The determined n values are formal way of assigning the type of photoconduction charecteristic of material. Based on this analysis, it was deduced that n value was varying from 0.6 to 0.9 ($n<1$) and from 1.2 to 1.5 ($n>1$) at low and high temperatures, respectively. The found these values state the existance of sublinear and supralinear photoconduction at low and high temperature regions, respectively.

Finally, the obtained some important compositional, structural, electrical and optical results for $AgGaSe_{2-x}S_x$ thin films for $0 \leq x \leq 2$ are summarized in following table.

Material	**Deposition Technique**	**Chemical Composition**				
		Atomic Percentage (%)				
$AgGaSeS$	*Thermal Evaporation*	*Sample*	*Ag*	*Ga*	*Se*	*S*
		As-grown	5.58	27.76	13.84	52.82
		450 °C	3.86	41.09	21.04	34.01
		600 °C	3.63	36.73	21.24	38.40
$AgGaSe_2$	*Electron Beam*	*Sample*	*Ag*	*Ga*	*Se*	
		As-grow	13.76	33.71	52.53	
		450 °C	12.18	34.51	53.31	
		550 °C	10.51	35.07	54.42	
		600 °C	9.34	35.09	55.56	
$AgGaSe_2$	*Sputtering*	*Sample*	*Ag*	*Ga*	*Se*	
		As-grown	17.99	32.07	49.93	
		450 °C	17.87	32.77	49.36	
		550 °C	22.98	35.39	41.63	
$AgGa_5S_8$	*Thermal Evaporation*	*Sample*	*Ag*	*Ga*	*S*	
		As-grown	7.00	35.86	57.14	
$AgGaS_2$	*Thermal Evaporation*	*Sample*	*Ag*	*Ga*	*S*	
		As-grown	19.00	27.00	54.00	
		450 °C	20.57	26.00	53.43	
		650 °C	23.08	24.42	52.50	
		700 °C	25.02	23.00	51.98	

Material	Identified States	Resistivity (Room Temp.)	Type of Conduction	Mobility (Room Temp.)
AgGaSeS	*Sample* *States* As-grown Amorphous 550 °C $AgGaS_2$, Ga_2Se_3 600 °C $AgGaS_2$, Ga_2Se_3, S	*Sample* *ρ (Ω.cm)* As-grown $7x10^7$ 300 °C $5x10^7$ 450 °C $2x10^7$ 500 °C $3x10^7$ 550 °C $9x10^6$	n	
$AgGaSe_2$	*Sample* *States* As-grown Amorphous 350 °C Ag 550 °C GaSe, Ag, Ga_2Se_3 600 °C GaSe, $AgGaSe_2$, Ga_2Se_3	*Sample* *ρ (Ω.cm)* As-grown $1.4x10^5$ 550 °C $3.0x10^5$	n	
$AgGaSe_2$	*Sample* *States* As-grown Ag 450 °C Ag 550 °C $AgGaS_2$, Ag 600 °C $AgGaS_2$	Sample ρ (Ω.cm) As-grown 1000 450 °C 965 550 °C 30	n	Sample μ (cm^2/V.s) As-grown 6.4 450 °C 3.7 550 °C 3.0
$AgGa_5S_8$	*Sample* *States* As-grown Amorphous 350 °C Ag 550 °C Ag, $AgGa_5S_8$	*Sample* *ρ (Ω.cm)* As-grown 1410 550 °C $4.5x10^7$	n	
$AgGaS_2$	*Sample* *States* As-grown Ag 450 °C GaS, Ag 650 °C GaS, $AgGaS_2$ 700 °C $AgGaS_2$	Sample ρ (Ω.cm) As-grown $2x10^3$ 600 °C $5x10^3$ 700 °C $9x10^6$	n	Sample μ (cm^2/V.s) As-grown 6.7 600 °C 64 700 °C 37

Material	Free Carrier Cons. (n) (Room Temp.)	Optic Constants	Band Gap (eV)
$AgGaSeS$			Sample E_g As-grown 2.68 450 °C 2.85 500 °C 2.82 550 °C 2.83 600 °C 2.81
$AgGaSe_2$			Sample E_g As-grown 2.25 300 °C 2.32 400 °C 2.32 500 °C 1.74 600 °C 1.78
$AgGaSe_2$	Sample $n\ (cm^{-3})$ As-grown $9.6x10^{14}$ 450 °C $1.7x10^{15}$ 550 °C $6.6x10^{16}$		Sample Eg_1 Eg_2 Eg_3 As-grown 1.58 2.03 2.36 550 °C 1.77 2.00 2.25
$AgGa_5S_8$		*Sample* *n* *k* *Range (nm)* As-grown 2.0-2.2 0.04-0.02 530-680 350 °C 2.4-2.6 ~0.04 490-680 550 °C ~1.8 ~0.02 500-680	Sample E_g As-grown 2.30 350 °C 2.48 550 °C 2.75
$AgGaS_2$	Sample $n\ (cm^{-3})$ As-grown $5.7x10^{13}$ 600 °C $1.9x10^{13}$ 700 °C $2.5x10^{10}$		Sample E_g As-grown 2.65 600 °C 2.74 700 °C 2.79

REFERENCES

[1] G. D. Boyd, H. M. Kasper, J. H. McFee, F. D. Storz *IEEE J. Quant. Electron.* 8, p. 900, (1972).

[2] N. Yamamoto, H. Takehara, H. Horinaka, T. Miyauchi *Jpn. J. Appl. Phys.* 25 p. 1397, (1986).

[3] P. G. Schunemann, S. D. Setzler, T. M. Pollak *J. Crystal Growth* 211, p. 257 (2000).

[4] B. M. Basol, A. Halani, C. Leidhalm, G. Norsworthy, V. K. Kapur, A. Swatzlander, R. Matson *Prog. Photovolt. Res. Appl.* 8, p. 227, (2000).

[5] J. L. Shay and J. H. Wernick, *Ternary Chalcopyrite Semiconductors: Growth, Electronic Properties and Applications*. Pergamon Press, Oxford, 1975.

[6] P. C. Ricci, A. Anedda, R. Corpino, C. M. Carbonaro, M. Marceddu, I. M. Tiginyanu, V. V. Ursaki *Journal of Physics and Chemistry of Solids* 66, p. 1950, (2005). .

[7] H. C. Hsu, H. H. chen, S. Y. Kuo, C. S. Chang,W. F. Hsieh *Thin Solid Films* 419, p. 237, (2002).

[8] F. K. Hopkious *Laser Focus World* 31, p. 87 (1995).

[9] F. Rotermund, V. Petrov, F. Noock *Opt. Commun.* 185, p.177, (2000).

[10] A. Chahed et al *Physica B* 367, p. 142 (2005).

[11] B.-J. Zhao et al *Crystal Res. Technol.* 33, p. 943, (1998).

[12] B. Tell, H. M. Kasper *Physical review B* 4, p. 12 (1971).

[13] H. V. Campe *Thin Solid Films* 111, p. 17 (1984).

[14] P. G. Schunemann, S. D. Setzler, T. M. Pollak *Journal of Crystal Growth* 211, 257, (2000).

[15] G. C. Bhar, S. Das, D. V. Satyanarayan, P. K. Datta, U. Nundy, Y. N. Andreev *Opt. Lett.* 15, p. 2057, (1995).

[16] E. Takaoka, K. Kato *Opt. Lett.* 24, p.902, (1999).

[17] P. Ribinson, J. I. B. Wilson *Inst. Phys. Conf. Ser.* 35, p. 229, (1977).

[18] G. F. Knoll, *Radiation Detection and Measurement 3rd edit.,* New-York; Willey, 1999.

[19] Y. Satyanarayana Murty, O. M. Hussain, B. S. Naidu, P. J. Reddy *Mater. Lett.* 10, p. 504, (1987).

[20] H. Matsuo, K. Yoshino, T. Ikari *Thin Solid Films* 515, p. 505, (2006).

[21] B. Tell, H. M. Kasper *Phys. Rev. B* 4, p. 4455, (1971).

[22] K. –M. Nigge, F. P. Baumgartner, E. Bucher *Solar Energy Materials and Solar Cells* 43, p. 335, (1996).

[23] U. N. Roy, Y. Cui, R. Hawrami, A. Burger, L. Orona, J. T. Goldstein *Sol. Stat. Commun.* 139, p. 527, (2006).

[24] K. –M. Nigge, F. P. Baumgartner, E. Bucher *Solar Energy Materials and Solar Cells* 43**,** p. 335, (1996).

[25] A. Rockett, R. W. Birkmire *J. Appl. Phys.* 70, p. R81, (1981).

[26] H. W. Schock *Appl. Surf. Sci.* 92, p. 606, (1996).

[27] I. V. Bodnar, I. A.Victorov, T. L. Kushner., Y. V. Rud *Thin Solid Films* 487, p.199**,** (2005).

[28] H. S. Soliman *J. Phys. D: Appl. Phys.* 28, p. 764, (1995).

[29] M. Belhadj, A. Tadjer, B. Abbar, Z. Bousahla, B. Bouhafs, H. Aourag *Phys. Stat. Sol. (b)* 241, p. 2516, (2004).

[30] L. Artus, Y. Bertrand, C. Ance *J. Phys. C: Solid State Phys.* 19, p. 5937, (1986).

[31] L. C. Tang, M. H. Lee, C. H. Yang, J. Y. Huang, C. S. Chang *J. Phys. : Condens. Matter.* 15, p. 6043, (2003).

[32] D. Xue, K. Betzler, H. Hesse, D. Lammers *Phys. Stat. Solidi b* 216, p. R7, (1999).

[33] E. Niwa, K. Masumato *J. Crystal Growth* 192, p. 354, (1998).

[34] B. Chen, S. Zhu, B. Zhao, J. Zhang, Y. Huang, M. Li, J. Li, B. Tan, R. Wang, Z. He *J. Crystal Growth* 292, p. 490, (2006).

[35] S. Shirakata, T. Terasako, E. Niwa, K. Masumato *J. Physics and Chemistry of Solids* 64, p. 1801, (2003).

[36] M. Marceddu, A. Anedda, C. M. Carbonaro, D. Chiriu, R. Corpino, P. C. Ricci *Applied Surface Science* 253, p. 300, (2006).

[37] H. Matsuo, T. Tokuda, K. Yoshino, A. Kinoshita, T. Ikari, K. Kakimoto, S. Seto *Physics Status Solidi C* 6, p. 1070, (2009).

[38] S.-F. Zhue, B. –J. Zhao, J. Liu, Z. –H. Li, W.-T. Li *Material chemistry and*

Physics 50, p. 94, (1997).

[39] W. Z. Shen, S. C. Zhen, Y. Chang, W. G. Tang, G. C. Chen, L. Yang *Infrared Physics & Technology* 38, p. 113, (1997) .

[40] E. Calderon, B. Fernandez, L. Duran, P. Grima, M. Morocoima, E. Quintero *Physica B* 404, p. 4095, (2009).

[41] M. R. A. Bhuiyan, S. M. F. Hasan *J. Phys. D:Appl. Phys.* 39, p. 4935, (2006).

[42] A. Wagendristel and Y. Wang, *An Introduction to Physics and Technology of Thin Films*. World Scientific Publishing, Singapore-New Jersey-London-Hong Kong, 1994.

[43] M. Volmer, A. Weber *Z. Phys. Chem.* 119, p.277, (1920).

[44] F. C. Frank, J. H. Van der Merwe *Proc. R. Soc. London, Ser. A.* 198, p.205, (1949).

[45] J. N. stranski, L. Krastanov *Ber. Akad. Wiss. Wien* 146, p.797, (1938).

[46] Jong-Hee Park, *Chemical Vapor Deposition*. ASM International, The Material International Society, 2001.

[47] A. Z. Moshfegh, H. V. Kanel, S. C. Kashyap, M. Wuttig, *Physics and Technology of Thin Films IWTF 2003*. World Scientific Publishing, 2004.

[48] Shabbir A. Bashar, *Study of Indium Tin Oxide for Novel Optoelectronic Devices*, Ph.D Thesis, University of London, 1998.

[49] R.Darling *Lecture notes on Physical Vapor Deposion*, http://www.engr.washington.edu/~cam/PROCESSES/physicalvapdeppdf.html

[50] L. I. Maissel, M. H. Francombe, *An Introduction to Thin Films*. Gordon and Breach Science Publishers, New York-London-Paris, 1973.

[51] D. M. Mattox, *Handbook of Physical Vapor Deposition (PVD) Processing*. Noyes Publications, 1998.

[52] J. Zhou, *Indium Tin Oxide Deposition, Patterning, and Schottky Contact Fabrication*, Ms Thesis, Rochester Institute of Technolgy, Rochester, Newyork, 2005.

[53] John F. Watts, J. Wolstenholme, *An Introduction to Surface Analysis by XPS and AES.* John Willey and Sons Ltd, 2003.

[54] B. G. Yacobi, *Semiconductor Materials: An Introduction to Basic Principles*. Kluwer Academic/Plenum Publishers, London 2002.

[55] http://www.sckcen.be/microstructure/Infrastructure/XPS/.

[56] http://www.azom.com/details.asp?articleid=1556

[57] S. L. Flegler, J. W. Heckmen, K. L. Klomparens, *Scanning and Transmission Electron Microscopy, An introduction*, Oxford University Press. Oxford, 1993.

[58] B. D. Cullity, *Elements of X-ray Diffraction*. Addison-Wesley, Second Edition, 1978.

[59] C. Suryanarayana, M. Grant Norton, *X-ray Diffraction: a practical approach*. Plenum Press, New York, 1998.

[60] C. S. Barret, *Structure of Metals, Crystallographic Methods, Principles and Data*. Mc Graw-Hill, New York, 1956.

[61] C. R. Brundle, C. A. Evans, shaun Wilson, *Encylopedia of Materials Characterization: Surfaces, Interfaces, Thin Films*. Butterworth-Heinemman, Elsevier, 1992.

[62] D. K. Schroder, *Semiconductor Material and Device Characterization*. Jhon Willey and Sons, NY, 1990.

[63] M. Fox, *Optical Properties of Solids*. Oxford University Press, 2001.

[64] P. K. Basu, *Theory of Optical Process in Semiconductors*. Oxford Science Publications, Oxford University Press, 2005.

[65] J. I. Pankove, *Optical Process in Semiconductor*. Prentice-Hall, London, 1971.

[66] H. Karaağaç, Structural, *Electrical and Optical Characterization of Ge-implanted GaSe Single Crystal Grown By Bridgman Method*, Ms Thesis, Middle East Technical University, 2005.

[67] N. V. Joshi, *Photoconductivity, Art, Science, and Technology*. Marcel Dekker Inc., New York and Basel, 1990.

[68] R. H. Bube*, Photoelectronic Properties of semiconductors*. Cambridge University, 1992.

[69] R. H. Bube, *Photoconductivity of Solids*. John Willey and Sons, 1960.

[70] A. Luque, S. Hegedus, *Handbook of Photovoltac Scienc and Engineering.* John Willey and Sons, 2005.

[71] Murat Kaleli, *Investigation of Electrical and Optical Properties of Ag-In-Se Based Devices*, PhD. Thesis in Physics Department of Middle East Technical University, 2010.

[72] M. Venkatachalam, M. D. Kannan, S. Jayakumar, R. Balasundarapraphu, A. K. Nandakumar, N. Muthukumarasamy *Solar Energy Materials & Solar Cells* 92, p. 571, (2008).

[73] Tahir Çolakoğlu, *The Effect of Post-Annealing Process on The Physical Properties of Silver-Indium-Selenium Ternary Semiconductor Thin Films Deposited By Electron Beam Technique*, PhD Thesis in Physics Department of Middle East Technical University, 2009.

[74] Lake Shore User's Manual, *7500/9500 Series Hall Effect/Cryotronic Hall Effect Electronic Transport Measuring System*. Lake Shore Cryotronics Inc., USA.

[75] Cryostat, Janis Research Co., Wilmington, MA, USA.

[76] M. Kurasava, S. Kobayashi, F. Kaneko, K. Oishi, I. S. Ohta *J. Cryst. Growth 167*, p.151, **(**1996).

[77] M. A. Afifi, A. E. Bekheet, H. T. El-Shair, I. T. Zedan *Physica B: Conden. Matter 325***,** p. 308, (2003).

[78] T. Çolakoğlu, M. Parlak *Appl. Surf. Sci.* 254**,** p. 1569, (2008).

[79] NIST Database*: http://srdata.nist.gov/xps*

[80] N. F. Mott, E. A. Davis, *Electronic Process in Noncrystalline Materials*. Oxford: Clarendan Press, 1971.

[81] C. D. Blasi, D. Manno, G. Micocci, A. Tepore *J.Appl. Phys.* 65, p. 1164, (1989).

[82] B. Thomas, T. R. N. Kutty *Phys. Stat. Sol. A* 119, p. 127, (1990).

[83] C. Julien, N. Benramdabe, J. P. Guesdon *Semicond. Sci. Technol.* 6, p. 905, (1990).

[84] Joint Committee on Powder Diffraction Standarts (JCPDS) Card no. 31-0717

[85] Joint Committee on Powder Diffraction Standarts (JCPDS) Card no. 87-0717

[86] Joint Committee on Powder Diffraction Standarts (JCPDS) Card no. 37-0931

[87] Joint Committee on Powder Diffraction Standarts (JCPDS) Card no. 05-0727

[88] A. Van der Drift *Philips Res. Rep.* 22, p. 267 (1967).

[89] R. Caballero, C. Maffiotte, C. Guillen *Thin solid Films* 474, p. 70, (2005).

[90] V. K. Kaushik *J. Electron Spectr. Relat. Phemon.* 56, p. 273, (1991).

[91] R. Romand, M. Roubin, J. P. Deloume *J. Solid State Chem.* 25, p. 59, (1978).

[92] S. Zembutsu *Appl. Phys. Lett.* 39, p. 969, (1981).

[93] P. A. Bertrand *J. Vacuum Sci. Tech.* 18, p. 28 (1981).

[94] J. M. Thomas, I. Adams, R. H. Williams, M. Barber *J. Chem. Soc., Faraday Trans. II* 68, p. 755, (1972).

[95] S. Badrinarayanan, A. B. Mandale, V. G. Gunjikar, A. P. B. Sinna *J. Mater. Sci.* 21, p. 3333, (1986).

[96] W. E. Swartz, K. J. Wynne, D. M. Hercules *Anal. Chem.* 43, p. 1884, (1971).

[97] A.Roth, *Vacuum Technology 2nd Edn*. Amsterdam:North-Holland, 1980.

[98] C. M. Joseph, C. S. Menon *Semicond. Sci. Technol.* 11, p. 1668, (1996).

[99] Joint Committee on Powder Diffraction Standart (JCPDS) Card no: 04-0783

[100] Joint Committee on Powder Diffraction Standart (JCPDS) Card no: 31-1240

[101] H. Karaagac, M. Parlak *Applied Surface Science* 255, p. 5999, (2009).

[102] S. C. Abrahams, J. L. Bernstein *J. Chem. Phys.* 59, p. 5415, (1983).

[103] D. S. D. Amma, V. K. Vaidjan, P. K. Manoj *Mater. Chem. Phys.* 93, p. 194, (2005).

[104] Y. S. Murty, S. Uthana, B. Srinivasulu Naidu, P. J. Reddy *Sol. Stat. Commun.* 79, p. 277, (1991).

[105] M. R. A. Bhuiyan, D. K. Saha, S. M. F. Hasan *Indian Journal of Pure and Applied Physics* 47, p. 787, (2009).

[106] R. Marquez, C. Rincon *Mater. Lett.* 40, p. 66 (1999).

[107] L. L. Kazmerski, *Polycrystalline and Amorphous Thin Films and Device.* Academic Press, New-York, 1980.

[108] S. Roy, B. Bhattacharjee, S. N. Kundu, S. Chaudhuri, A. K. Pal *Material Chemistry and Physics* 77, p. 365, (2002) 365.

[109] Joint Committee on Powder Diffraction Standart (JCPDS) Card no: 270615.

[110] Joint Committee on Powder Diffraction Standart (JCPDS) Card no: 321008.

[111] N. M. Shah, J. R. Ray, K. J. Patel, V. A. Kheraj, M. S. Desai, C. J. Panchal , B. Rehani *Thin Solid Films* 517, p. 3639, (2008).

[112] C. C. Garry, B. David. *MRS Bulletin* 7, p. 28, (1998).

[113] H. Karaagac, M. Kaleli, M. Parlak *J. Phys. D:Appl. Phys.* 42, p. 165413, (2009).

[114] L. Artus, Y. Bertrand, L. Soler *J. Phys. C:Solid State Phys.* 20, p. 111, (1987).

[115] D. Redfield, R. H. Bube*, Photoinduced Defects in Semiconductors*. New-York: Cambridge University Press, 1996.

[116] Joint Committee on Powder Diffraction Standart (JCPDS) Card no: 491362

[117] Joint Committee on Powder Diffraction Standart (JCPDS) Card no: 750114

[118] Y. Akaki, S. Kurihara, M. Shirahama, K. Tsurugida, S. Seto, T. kakeno, Y. Yoshino *J. Of Physics and Chemistry of Solids* 66, p. 1858, (2005).

[119] H. Neumann *Cryst. Res. Technol.* 18, p. 483, (1983).

[120] S. M. Patel, V. G. Kapale *Material Letters* 4, p. 145, (1986).

VITA

PERSONAL INFORMATION

Surname, Name: Karaağaç, Hakan
Nationality: Turkish (TC)
Date and Place of Birth: 9 May 1983 , Diyarbakır
Marital Status: Single
Phone: +90 312 210 76 49
Fax: +90 312 210 50 99
email: karaagac@metu.edu.tr

EDUCATION

Degree	Institution	Year of Graduation
MS	METU Department of Physics	2005
BS	Çukurova Unv. Department of Physics	2003

WORK EXPERIENCE

Year	Place	Enrollment
2006-2010	METU Department of Physics	Research Assistant

FOREIGN LANGUAGES

Advanced English

PUBLICATIONS

A. Articles

1. **H. Karaagac**, M.Parlak, O.Karabulut, U.Serincan, R.Turan, B.G.Akınoğlu, *"Structural, Electrical, and Optical Properties of Ge-implanted GaSe Single Crystals Grown by Bridgman Technique"*, Cryst. Res. Technol., **41**, 1159, (2006).

2. **H. Karaagac**, M. Parlak, **"***Effects of Annealing on Structural, Electrical and Optical Properties of* $AgGa(Se_{0.5}S_{0.5})_2$ *Thin Films Deposited by Using Sintered Stoichometric Powder"*,Cryst. Res. Technol., **44**, 440, (2009).

3. **H. Karaagac** and M. Parlak, *"Effects of Annealing on Structural and Morphological Properties of Electron Beam Evaporated AgGaSe2 Thin Films"***,** Applied Surface Science, **255**, 5999, (2009).

4. **H. Karaagac**, M. Kaleli and M. Parlak, *"Characterization of $AgGa_{0.5}In_{0.5}Se_2$ Thin Films Deposited by Electron Beam Technique"*, Journal of Physics D: Applied Physics, **42**, 165413, **(**2009).

5. K.Yılmaz, **H.Karaagac,** *"Annealing Effects on Structural, Optical and Electrical Properties of E-Beam Evaporated $CuIn_{0.5}Ga_{0.5}Te_2$ Thin Films"*, Applied Surface Science, **256**, 6454, (2010).

6. **H.Karaağaç** and M. Parlak, *"Investigation of physical properties of quaternary $AgGa_{0.5}In_{0.5}Te_2$ Thin Films Deposited by Thermal Evaporation"*, Journal of Alloys and Compounds, **503**, 468, (2010).

7**. H. Karaagac**, M.Parlak, *"The investigation of structural, electrical, and optical properties of thermal evaporated AgGaS2 thin films",* (Submitted to Thin Solid Films: Acceptence date: September 10, 2010.)

8. **H. Karaagac**, M. Parlak, *"Deposition and Characterization of Layer by Layer Sputtered AgGaSe2 Thin Films",* (Submitted to Applied Surface Science. Submission date: Apr 14, 2010. Status: under review)

B. <u>Posters:</u>

1. **H. Karaağaç**, M. Kaleli, T. Çolakoğlu, M. Parlak, Ç.Erçelebi, *"Structural And Optical Properties of AgGa(SeS)2 Thin Films"*
E-MRS 2008 Spring Meeting, May 26-30, 2008, Strasbourg, France
Poster no:L-P1 38

2. T. Çolakoğlu, M. Parlak*, M. Kaleli, **H. Karaağaç**, Ç. Erçelebi,
"Structural and Optical Properties of Polycrystalline Ag-In-Se Thin Films Deposited"
E-MRS 2008 Spring Meeting, May 26-30, 2008, Strasbourg, France
Poster no:L-P3 31

3. M. Kaleli, T. Çolakoğlu, **H. Karaağaç**, M. Parlak, Ç.Erçelebi,
"Effect of Post Annealing on The Device Behaviors of p-Si/n-(Ag-In-Se) Junction"
E-MRS 2008 Spring Meeting, May 26-30, 2008, Strasbourg, France
Poster no:L-P3 32

4. T. Çolakoğlu, M. Parlak, M. Kaleli, **H. Karaagac**, C. Ercelebi,
"The Influence of Annealing Temperature on the Structural, Optical and Electrical Properties of Polycrystalline AgIn5Se8 Thin Films and Device Application"

NANOMAT 2008, International Workshop On Advanced Materials and Devices For Photovoltaic Applications, April 24-25, 2008,Ankara,Turkey
Poster no: P.32

5. **H. Karaağaç**, M. Parlak, T. Çolakoğlu, *"Characterization of Optical and morphological Properties of $AgGaSe_2$ Thin Films Deposited by Electron Beam Technique"*
15th High Condense Matter Meeting, Ankara,Turkey, December 7, 2008, Bilkent University
Poster no: P.9

6. **H. Karaağaç**, M. Parlak, I. Candan, M. Kaleli,
"Annealing Effects on The Structural and Optical Properties of $AgGa_{0.5}In_{0.5}Se_2$ Thin Films Deposited by Electron Beam Technique"
E-MRS 2009 Spring Meeting, June 8-12, 2009, Strasbourg, France
Poster no:B-P6 11

7. M. Kaleli, M. Parlak, **H. Karaağaç**, Ç.Erçelebi, I. Candan,
"The Device Behaviors of p-Si/n-(Ag-In-Se) Junction"
E-MRS 2009 Spring Meeting, June 8-12, 2009, Strasbourg, France
Poster no:B-P4 26

8. H. Karaagac, K. Yilmaz, M. Parlak*,"Characterization of qua-ternary CuIn0.5Ga0.5Te2 thin films deposited by electron-beam method"*
E-MRS 2010 Spring Meeting, June 7-11, 2010, Strasbourg, France
Poster no: M-P4 18

9. **H. Karaagac**, M. Parlak, Ç.Erçelebi, *"Characterization of Sputterering Deposited AgGaSe2 Thin Films"*
6th Nanoscience and Nanotechnology Conference: June 15-18, Çeşme, İzmir,Turkey

10. M. Kaleli, T. Çolakoğlu, **H. Karaağaç**, M. Parlak, Ç. Erçelebi,
"Device Characterization of n-Si/p-AgInSe2 Heterojunction Devices"
Solar TR-1, April, 29-30, METU, Ankara, Turkey

11. I. Candan, **H. Karaağaç**, M. Parlak, Ç. Erçelebi,
"Electrical and Optical Characterization of CuIn0.5Ga0.5Se2 Thin Films Deposited by E-beam Technique for Solar Cell Structure"
Solar TR-1, April, 29-30, METU, Ankara, Turkey

C. <u>Oral Presentations</u>

1. **H.Karaagac**, M.Parlak, O.Karabulut, R.Turan, B.Akınoğlu,
"Structural and Electrical Properties of Ge-implanted GaSe Single Crystal"
23th Turkish Society of Physics Meetting, Muğla,Turkey
Page No: 214

2. T. Çolakoğlu, M. Parlak, M. Kaleli, **H. Karaağaç,**
"The Effect of Heat Treatment on structural, Optical and Photoelectric Properties of $AgIn_5Se_8$ Thin Films"
15th High Condense Matter Physics Meeting, Ankara,Turkey, December 7, 2008, Bilkent University
Presentation No: S8

3. K. Yılmaz, **H. Karaağaç,**
"E-Demeti ile Büyütülmüş $CuIn_{0.5}Ga_{0.5}Te_2$ İnce Filmlerin Yapısal, Optik ve Elektriksel Özelliklerine Tavlamanın Etkisi"
16. Yoğun Madde Fiziği Ankara Toplantısı, 6 Kasım 2009, Gazi Üniversitesi
Bildiri No: S3

4. **H. Karaağaç**, M. Kaleli ve M. Parlak,
"Isısal Buharlaştırma Yöntemi ile Üretilen $AgGa_{0.5}In_{0.5}Te_2$ İnce Filmlerin Yapısal, Elektriksel ve Optiksel Özellikleri"
16. Yoğun Madde Fiziği Ankara Toplantısı, 6 Kasım 2009, Gazi Üniversitesi
Bildiri No: S7

5. M. Kaleli, **H. karaağaç** ve M. Parlak,
"Isısal Buharlaştırma Yöntemi ile Üretilen n-$AgIn_5Se_8$/p-Si Hetero-eklemlerin aygıt özellikleri"
16. Yoğun Madde Fiziği Ankara Toplantısı, 6 Kasım 2009, Gazi Üniversitesi
Bildiri No: S12